Mode Conversion Processes
in Magnetized Plasmas

A thesis submitted for the degree of
Doctor of Philosophy

by

Andrew Layden

School of Physics
University of Sydney
Australia

September 2013

Declaration of originality

To the best of my knowledge, this thesis contains no copy or paraphrase of work published by another person, except where duly acknowledged in the text. This thesis contains no material that has been presented previously for a degree at the University of Sydney or any other university.

<div align="right">Andrew Layden</div>

Included papers and attribution

Listed below are details of the papers (where published) on which Chapters 2 to 5 are based.

Chapter 2   **Changes in mode properties versus mode conversion for** I
waves in Earth's auroral ionosphere
A. Layden, I. H. Cairns, P. A. Robinson, and J. LaBelle,
Published in *Journal of Geophysical Research*, *116*, A12, 2011.

was primarily responsible for this work.

Chapter 3   **Electrostatic decay in a magnetized plasma**   I
A. Layden, I. H. Cairns, B. Li, and P. A. Robinson,
Published in *Physical Review Letters*, *110*, 18, 2013.

was primarily responsible for this work.

Acknowledgements

Firstly, I would like to thank my supervisor Professor Iver Cairns and associate supervisor Professor Peter Robinson. Their insight, guidance and encouragement have been indispensible and have made this thesis a pleasure to write. I thank my postgraduate colleagues and faculty in the Space and Plasma Group for stimulating discussions and assistance with various aspects of this research. Finally, I would like to thank my family, whose support during my candidature I could not have done without.

Abstract

Mode conversion processes in plasmas allow wave energy to be transferred between two or more different wave modes, and are often invoked in theories of space and astrophysical phenomena. For instance, electrostatic Langmuir waves which are trapped in the solar wind plasma can be converted to electromagnetic radiation and produce radio bursts, which can propagate through the plasma and thus be observed remotely.

In environments where mode conversion has been invoked there is often a significant ambient magnetic field. This modifies the dispersion relations of the wave modes and can result in additional wave modes. However, magnetization effects have been neglected in the analyses of certain mode conversion processes.

This thesis presents a number of investigations into mode conversion processes as they occur in magnetized plasmas, focusing on the magnetization of the Langmuir mode. The structure of the thesis is as follows. Chapter 1 introduces the relevant plasma theory and presents an overview of space physics phenomena for which mode conversion has been proposed. It summarizes the relevant observations and the associated theoretical interpretations. Chapter 2 investigates a certain mode conversion process that was stated to occur in the magnetized plasma of the Earth's auroral ionosphere. It is shown that mode conversion, in this case, is not necessary to account for observations. Instead, magnetization causes a change in mode characteristics that allows the waves to evolve in character as they propagate, without any mode conversion. Chapter 3 presents the first calculations of the kinematics for electrostatic decay of Langmuir waves in a weakly magnetized plasma, which are then implemented in quasilinear simulations of wave growth in the source regions of type III solar radio bursts. Magnetization is found to significantly affect the decay process. Applications to a variety of space and astrophysical phenomena are then proposed. Chapter 4 contains a detailed investigation into the kinematics of three-wave processes, where decay in two dimensions and in strongly magnetized plasmas are considered. Chapter 5 presents further quasi-linear simulations of magnetized electrostatic decay, where the dependences of the wave fields and energy densities on various plasma parameters are investigated. Chapter 6 summarizes the work presented in this thesis and discusses avenues for possible future research.

Contents

Chapter 1

Literature review

In this chapter we introduce the plasma theory that underlies the following chapters and present an overview of the literature on these topics. The structure of this chapter is as follows. Section 1.1 introduces waves in plasmas and their properties. Section 1.2 discusses plasma wave energetics; i.e., their growth and damping by particles. Section 1.3 discusses mode conversion processes, in which wave energy in one mode is converted to energy in other modes. Section 1.4 presents the observational contexts where these plasma waves and conversion processes occur, as well as open questions about their mechanisms that are the subject of the following chapters.

1.1 Plasma waves

Plasmas support a variety of wave modes, which are the natural modes of oscillation of wave fields and particles. These are described by Maxwell's equations, which in Fourier form are

$$\mathbf{k} \times \mathbf{E}(\omega, \mathbf{k}) = \omega \mathbf{B}(\omega, \mathbf{k}), \tag{1.1}$$

$$\mathbf{k} \times \mathbf{B}(\omega, \mathbf{k}) = -\omega \mathbf{E}(\omega, \mathbf{k})/c^2 - i\mu_0 \mathbf{J}(\omega, \mathbf{k}), \tag{1.2}$$

$$\mathbf{k} \cdot \mathbf{E}(\omega, \mathbf{k}) = -i\rho(\omega, \mathbf{k})/\epsilon_0, \tag{1.3}$$

$$\mathbf{k} \cdot \mathbf{B}(\omega, \mathbf{k}) = 0. \tag{1.4}$$

Here $\mathbf{E}$ and $\mathbf{B}$ are the electric and magnetic fields, ρ and $\mathbf{J}$ are the charge and current densities, ϵ_0 and μ_0 are the permittivity and permeability of free space, and ω and $\mathbf{k}$ are the (angular) frequency and wave vector of the fluctuating quantities. Equations (1.1)–(1.4) can be reduced to a single equation (the "wave equation"),

$$\frac{\omega^2}{c^2}\mathbf{E} + \mathbf{k} \times (\mathbf{k} \times \mathbf{E}) = -i\omega\mu_0\mathbf{J}, \tag{1.5}$$

regarding the magnetic field and charge density as subidiary quantities determined by $\mathbf{B} = \mathbf{k} \times \mathbf{E}/\omega$ and $\rho = \mathbf{k} \cdot \mathbf{J}/\omega$, respectively. A wave mode M is a solution to (1.5) characterized by its dispersion relation $\omega_M(\mathbf{k})$ and its polarization vector $\mathbf{e}_M(\mathbf{k}) := \mathbf{E}/E$. Longitudinally polarized waves have $\mathbf{k} \times \mathbf{e}_M = 0$ and so from (1.1) are electrostatic (i.e., $\mathbf{B} = 0$), whereas purely transverse waves have $\mathbf{k} \cdot \mathbf{e}_M = 0$ and are electromagnetic. Solutions of the wave equation are determined by the plasma's dielectric response tensor, which relates $\mathbf{E}$ linearly to the induced current $\mathbf{J}$ and depends on such properties as temperature, particle species and density, and the presence or absence of significant ambient magnetic fields.

In the Vlasov approach [*Vlasov*, 1968; *Melrose*, 1986a], the dielectric tensor is derived in terms of the particle velocity distribution $f(\mathbf{v})$, which is assumed to satisfy the collisionless Boltzmann equation with the electromagnetic fields calculated self-consistently. For an unmagnetized and fully ionized electron-ion Maxwellian plasma this gives three weakly damped modes: Langmuir, transverse, and ion sound modes.

A less general approach involves the fluid description of the plasma, in which the response is described in terms of the moments of $f(\mathbf{v})$ such as the mean density and flow velocity. Neglecting thermal motions yields the magnetoionic modes for an electron fluid, or the cold plasma modes if multiple particle species are present.

We discuss the properties of these modes below, as well as the case where both magnetization and thermal effects are retained.

1.1.1 Thermal unmagnetized modes

The Langmuir mode is an electrostatic mode in which ions are essentially static but the electrons and electric field oscillate with frequency ω_L and wavenumber k related via the dispersion relation (e.g. *Chen* [1974])

$$\omega_L(\mathbf{k}) = (\omega_p^2 + 3k^2 V_e^2)^{1/2}. \tag{1.6}$$

Here $\omega_p = \sqrt{e^2 n_e / m_e \epsilon_0}$ is the (electron) plasma frequency, e is the charge of the electron, n_e is the electron number density, m_e is the mass of the electron, $V_e = \sqrt{k_B T_e / m_e}$ is the electron thermal speed, k_B is Boltzmann's constant, and T_e is the electron temperature. Dispersion relations for this mode and the following modes are shown in Fig. 1.1.

The transverse mode in a plasma is the counterpart of the free-space elec-
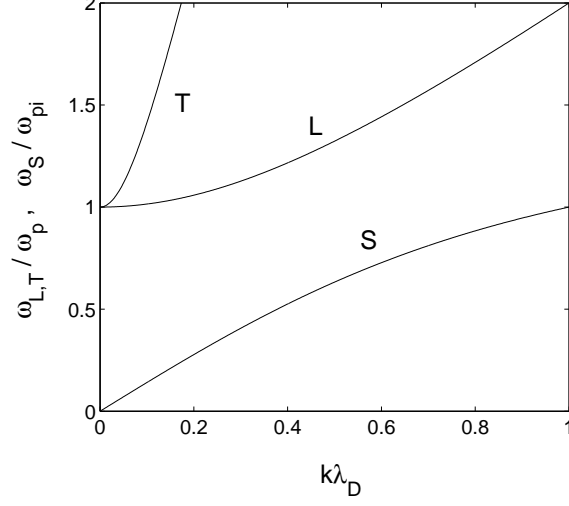
Figure 1.1: Dispersion relations for Langmuir (L), transverse (T), and ion sound (S) modes in an unmagnetized thermal plasma. Langmuir and transverse frequencies are normalized by ω_p whereas the ion sound frequency is normalized by $\omega_{pi} = (m_e/m_i)^{1/2}\omega_p \approx \omega_p/43$.

tromagnetic mode, with dispersion relation (e.g. *Chen* [1974])

$$\omega_T(\mathbf{k}) = (\omega_p^2 + k^2c^2)^{1/2}, \tag{1.7}$$

where c is the speed of light. Radio waves and other "light waves" exist in the transverse mode (and its magnetized counterparts).

The ion sound mode is a low-frequency electrostatic mode with dispersion relation

$$\omega_S(\mathbf{k}) = \frac{kv_S}{\sqrt{1 + k^2\lambda_D^2}}, \tag{1.8}$$

where $v_S = V_e\sqrt{\gamma m_e/m_i}$ is the ion sound speed, m_i is the ion mass, $\gamma = 1 + 3T_i/T_e$, T_i is the ion temperature, and $\lambda_D = V_e/\omega_p$ is the Debye length. In the long-wavelength limit $k\lambda_D \ll 1$, (1.8) becomes

$$\omega_S = kv_S. \tag{1.9}$$

1.1.2 Magnetoionic and cold plasma modes

Magnetoionic theory [*Appleton*, 1932] models the plasma as a cold, magnetized electron fluid, thereby ignoring ion effects. In this case there are four wave modes: o, x, z, and whistler. The o and x modes are magnetized counterparts

3

of the transverse mode and are left- and right-hand circularly polarized, respectively. The o mode is the lower-frequency mode and has a cutoff frequency of ω_p, whereas the x mode has a cutoff frequency of $\frac{1}{2}\Omega_e + \frac{1}{2}\sqrt{\Omega_e^2 + 4\omega_p^2}$, where $\Omega_e = eB/m_e$ is the electron cyclotron frequency and B is the magnetic field strength.

The z mode has a cutoff frequency of $-\frac{1}{2}\Omega_e + \frac{1}{2}\sqrt{\Omega_e^2 + 4\omega_p^2}$ and resonance frequencies of ω_p for parallel propagation and $\omega_{uh} = \sqrt{\omega_p^2 + \Omega_e^2}$ for perpendicular propagation. Here ω_{uh} is termed the upper hybrid frequency. The polarization of the z mode is left-handed below ω_p and right-handed above ω_p. When $\Omega_e = 0$ the z mode dispersion relation reduces to $\omega(\mathbf{k}) = \omega_p$; i.e., the unmagnetized Langmuir mode (1.6) described above but with $V_e = 0$.

The whistler mode has no counterpart in unmagnetized plasma theory. It has right-hand polarization and is restricted to frequencies below the minimum of ω_p and Ω_e.

The generalization of magnetoionic theory to multiple particle species is known as cold plasma theory [*Åström*, 1950]. Specifically, the magnetoionic modes become modified at frequencies on the order of the ion plasma frequency $\omega_{pi} = \omega_p\sqrt{m_e/m_i}$ and the ion cyclotron frequency $\Omega_i = q_i B/m_i$, while new modes appear. These include a magnetized ion sound mode, the Alfvén mode, and cyclotron modes for each of the ion species present.

1.1.3   Warm magnetized modes

The mode structure for the case of a warm magnetized plasma is more complicated than for the unmagnetized or cold plasma approximations. Specifically, it is not immediately clear whether the modes derived in these two approximations remain separate or combine when both magnetization and thermal effects are important. Recently, numerical solutions of the Vlasov dispersion equation obtained by *Willes and Cairns* [2000] have confirmed analytic arguments (e.g. *Melrose* [1980a]) for the existence of a generalized Langmuir mode. At large k this mode has Langmuir-like dispersion and for small k combines with either the z mode or the whistler mode for weakly magnetized ($\Omega_e < \omega_p$) or strongly magnetized ($\Omega_e > \omega_p$) plasmas, respectively. These generalized modes are often termed the Langmuir-z and Langmuir-whistler modes. Typical dispersion relations for these modes are presented in Fig. 1.2, for both strongly and weakly magnetized plasmas.

The polarization characteristics of the Langmuir-z and Langmuir-whistler modes also have important differences from the Langmuir mode. As demon-
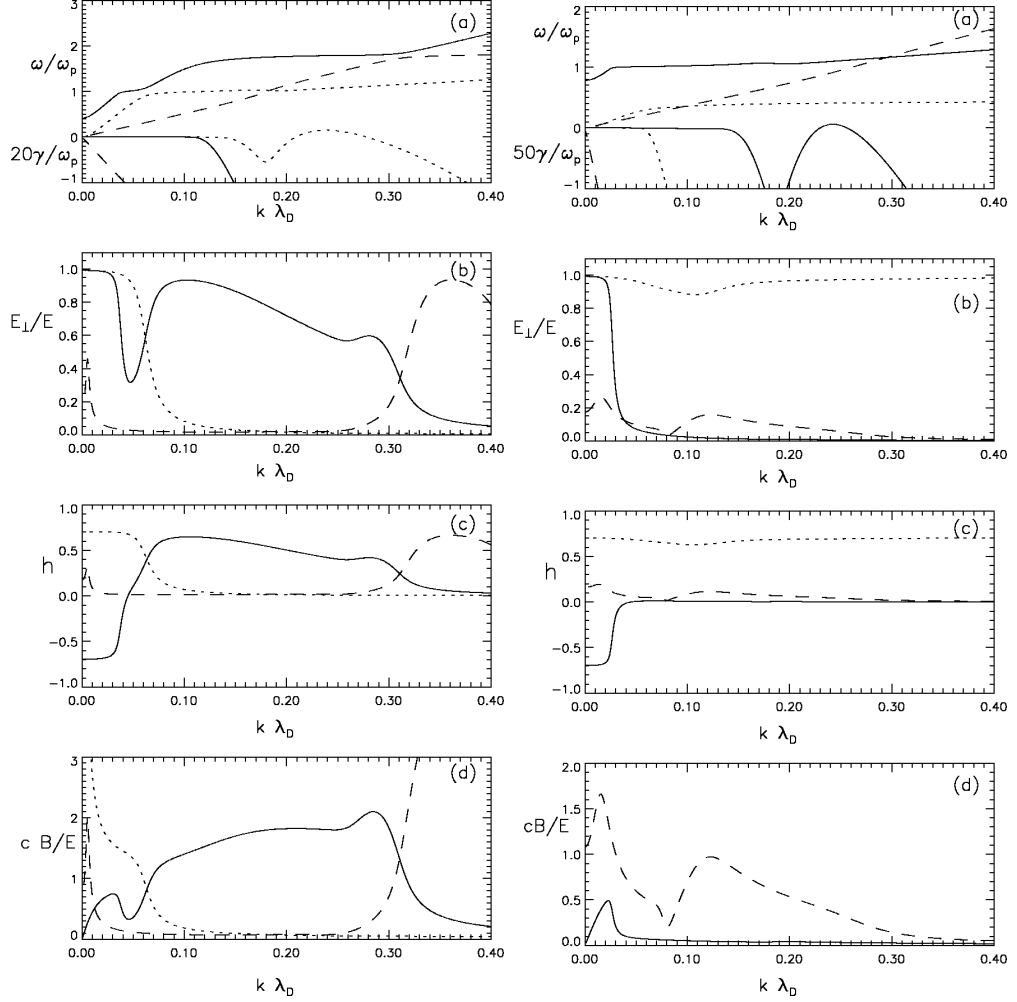
Figure 1.2: Exact solutions of the linear Vlasov dispersion equation, for $\Omega_e = 0.5\omega_p$ and $\Omega_e = 2\omega_p$, with $\theta = 10°$, $V_e/c = 4.5 \times 10^{-2}$, and a weak beam $(n_b/n_e = 10^{-3})$ of speed $v_b = 5V_e$ [*Willes and Cairns*, 2000]. (a) Dispersion relations ω/ω_p and growth rates γ/ω_p, where the solid (dotted) line represents the mode that is z-mode-like (whistler-like) at low k. A beam mode represented by a dashed line also exists but is unimportant for this literature review. (b) The normalized magnitude of the perpendicular electric field, $E_\perp/E$. (c) The handedness parameter h which is positive (negative) for right-hand (left-hand) polarized waves. (d) Dimensionless ratio of wave magnetic to electric field strengths, cB/E.

strated in Fig 1.2, at large k these modes are electrostatic like the Langmuir mode, but at small k are electromagnetic like the magnetoionic z and whistler modes [*Willes and Cairns*, 2000]. Thus, a mechanism that shifts Langmuir waves from high to low k can result in development of electromagnetic polarization. In Chapters 3–5 this is discussed with respect to recent STEREO observations of Langmuir wave polarization in type III solar radio bursts [*Malaspina et al.*, 2010].

1.2 Wave growth and damping

1.2.1 Collisionless damping

Interaction between plasma particles and waves can result in energy transfer between them. Consider a charged particle of velocity $\mathbf{v}$ moving in the electric field of a wave with frequency ω, wave vector $\mathbf{k}$, and phase velocity $v_\phi = \omega/k$. If the component of $\mathbf{v}$ parallel to $\mathbf{k}$ (which we denote as $v_\parallel$) approximately equals v_ϕ, then the particle experiences a nearly static electric field that will accelerate or decelerate the particle depending on the phase of the wave; this transfers energy from wave to the particle, or the particle to the wave, respectively. This situation results in the so-called Cherenkov resonance, which can be stated as $\omega - \mathbf{k} \cdot \mathbf{v} = 0$.

Analysis of first and second order perturbations of the equation of motion [*Melrose*, 1986a] shows that particles with $v_\parallel$ slightly smaller than v_ϕ tend to be accelerated, whereas those with $v_\parallel$ slightly larger than v_ϕ tend to be decelerated. If $\partial f/\partial v|_{v=v_\phi} < 0$ then there are more particles that gain energy from the waves than lose energy, resulting in a net transfer of energy from the waves to the particles. This collisionless damping process is known as Landau damping [*Landau*, 1946]. In a Maxwellian plasma, Landau damping of Langmuir waves takes the form

$$\gamma_L(k) = \left(\frac{\pi}{2}\right)^{1/2} \frac{\omega_L^4(k)}{k^3 V_e^3} \exp\left[-\frac{\omega_L^2(k)}{2k^2 V_e^2}\right]. \qquad (1.10)$$

The inverse process occurs when $\partial f/\partial v|_{v=v_\phi} > 0$ and results in energy transfer to the waves. It is referred to as a bump-on-tail (or beam or streaming) instability if the nonthermal particles are from an electron beam.

In a magnetized plasma the appropriate resonance condition for particles of species α is no longer the Cherenkov resonance condition but the gyroresonance condition $\omega - k_\parallel v_\parallel - s\Omega_e(1 - v^2/c^2)^{1/2} = 0$, where s is an integer and $\parallel$

denotes components parallel to the magnetic field **B**. Growth or damping associated with this resonance is referred to as cyclotron emission or absorption, respectively.

1.2.2 Collisional damping

Charged plasma particles in close proximity scatter each other through electrostatic interactions termed collisions. The frequency of electron-ion collisions is (e.g., *Chen* [1974])

$$\nu = \frac{\omega_p^2 q_i e}{4\pi\epsilon_0 m_e V_e^3} \log \Lambda, \tag{1.11}$$

where q_i is the ion charge and $\log \Lambda \approx 10$ is the Coulomb logarithm. Such collisions can attenuate waves by damping the oscillations of the associated particle species. Collisional processes dominate in cold and dense plasmas, where $\nu \gg \omega_p, \Omega_e$; they are negligible for hot and diffuse plasmas. Plasma parameters for ionospheric and space plasmas are predominantly of the latter kind and thus collisional processes will be neglected in this thesis.

1.2.3 Quasilinear theory

Quasilinear theory [*Drummond and Pines*, 1962; *Vedenov et al.*, 1962] models the coupled evolution of an ensemble of waves and particles, including the effects of emission and absorption of waves by the particles. An essential assumption in this theory is "weak turbulence": namely, the wave energies are sufficiently small that phase information is unimportant. This allows phase to be averaged over so that wave interactions can be described solely in terms of their intensities [*Robinson*, 1997]. A semiclassical formalism can then be employed, in which waves in a mode M are regarded as a collection of wave quanta, each with momentum $\hbar\mathbf{k}$ and energy $\hbar\omega_M(\mathbf{k})$. An occupation number $N_M(\mathbf{k})$ is then defined as the number density of quanta in the range $d^3\mathbf{k}$ of $\mathbf{k}$. The one-dimensional quasilinear equations for $N(k)$ and $f(v)$ are [*Melrose*, 1986a]

$$\frac{dN(k)}{dt} = \alpha(k) - \gamma(k)N(k), \tag{1.12}$$

$$\frac{df(v)}{dt} = \frac{\partial}{\partial v}\left[A(v)f(v) + D(v)\frac{\partial f(v)}{\partial v}\right], \tag{1.13}$$

where

$$\alpha(k) = \frac{e^2}{4\epsilon_0\hbar}\frac{v^3}{V_e^2}(1 - k^2\lambda_D^2)f(v)\bigg|_{v=\omega/k}, \qquad (1.14)$$

$$\gamma(k) = -\frac{\pi e^2}{m_e\epsilon_0}\frac{v^3}{V_e^2}k\lambda_D^2\frac{\partial f(v)}{\partial v}\bigg|_{v=\omega/k}, \qquad (1.15)$$

$$A(v) = \frac{e^2}{8\pi m_e\epsilon_0}\frac{v^2}{V_e^2}k^2(1 - k^2\lambda_D^2)\bigg|_{k=\omega/v}, \qquad (1.16)$$

$$D(v) = \frac{e^2\hbar}{2m_e^2\epsilon_0}\frac{v^2}{V_e^2}k^3\lambda_D^2 N(k)\bigg|_{k=\omega/v}. \qquad (1.17)$$

Here D is a diffusion coefficient, γ is the damping rate associated with stimulated absorption and emission (which is proportional to the wave levels), where $\gamma > 0$ ($\gamma < 0$) corresponds to Landau damping (growth), and α and A are coefficients related to spontaneous emission (which are independent of the wave levels). Collisional damping processes can also be included by introducing appropriate terms into (1.12).

Equations (1.12)–(1.17) contain a mechanism known as quasilinear relaxation by which waves can react back on the particles. Consider an unstable particle distribution, i.e., one with $\partial f/\partial v|_{v=u} > 0$ for some u. From (1.15) this gives $\gamma(k)|_{k=\omega/u} < 0$, causing exponential growth of $N(k)|_{k=\omega/u}$ via (1.12) (neglecting spontaneous emission). Since $D(u)$ is proportional to $N(k)|_{k=\omega/u}$ from (1.17) there is greater particle-velocity diffusion in (1.13), which flattens $f(v)$ about $v = u$ and thus saturates the instability.

Another approach is to find asymptotic solutions for $f(v)$ by solving (1.13) with $\partial f/\partial t = 0$. Provided spontaneous emission terms are neglected (i.e., $A(v) = \alpha(k) = 0$) one obtains a steady-state solution $\partial f(v)/\partial v = 0$, corresponding to a "plateau" distribution with $f(v)$ constant over some region of velocity space and zero elsewhere. If spontaneous emission terms are included then no such stable state exists, but numerical simulations of the quasilinear equations [*Grognard*, 1975] qualitatively resemble the asymptotic solutions at times much greater than the growth time and before spontaneous emission has become important.

Quasilinear relaxation is expected to saturate instabilities unless some process removes waves from resonance before they reach significant levels. Such suppression mechanisms can include linear and nonlinear processes, which are discussed in the following section.

1.3   Mode Conversion in Plasmas

Mode conversion is the transfer of energy between different wave modes. There are many mode conversion mechanisms in plasmas and their efficiencies depend either linearly or nonlinearly on the amplitudes of the participating wave fields. Here we discuss some examples of linear and nonlinear conversion processes.

1.3.1   Linear mode conversion

Plasmas with uniform density have wave modes that are distinct and uncoupled. However, the presence of density fluctuations can introduce complex-valued modes that connect previously uncoupled modes in frequency-wavevector space [*Kim et al.*, 2007]. Wave energy entering the inhomogeneous region in one mode can tunnel via these complex modes and be reflected in a different mode, in a process known as linear mode conversion [*Field*, 1956; *Budden and Jones*, 1986; *Hinkel-Lipsker et al.*, 1992; *Yin et al.*, 1998].

Linear mode conversion is relevant to a variety of modes, including magnetohydrodynamic modes such as the Alfvén mode [*Stix*, 1992], but here we focus on the magnetoionic and warm plasma modes. The coupling between Langmuir-z and o modes in particular has been invoked in a number of contexts: producing the "z trace" in ionospheric modification experiments [*Ellis*, 1956; *Budden*, 1985]; converting beam-driven Langmuir waves to radiation in type III solar radio bursts [*Field*, 1956; *Willes and Cairns*, 2001; *Kim et al.*, 2007]; and as a mechanism for generating nonthermal continuum radiation in planetary magnetospheres [*Jones*, 1976a; *Budden and Jones*, 1986; *Leblanc et al.*, 1986] and for the ionospheric "auroral roar" emissions [*LaBelle et al.*, 1995; *Weatherwax et al.*, 1995; *Yoon et al.*, 1998; *Willes and Cairns*, 2003].

1.3.2   Three-wave processes

Three-wave processes are nonlinear instabilities involving the decay of a wave into two product waves, or the coalescence of two waves to produce a third [*Tsytovich*, 1970; *Davidson*, 1972; *Melrose*, 1986a]. These can be represented by $M \rightarrow P+Q$ and $M+P \rightarrow Q$ respectively, where M, P, and Q correspond to the participating waves, each in a particular mode. If the bandwidth of the waves is small relative to the nonlinear growth rate, then the waves remain phase-coherent over timescales comparable with the instability. A so-called strong turbulence description must then be used, with the appropriate equations being

the Zakharov equations [*Zakharov*, 1972]. Conversely, if the waves have a relatively large bandwidth, then the waves' fast decoherence renders phase information unimportant and one can use the random-phase approximation to obtain a weak-turbulence (or random-phase) description of the instability with a semiclassical formalism (cf. Sec. 1.2.3). This approach allows conservation of energy and momentum to be imposed on a microscopic level to obtain the kinematics of the process. Different space physics contexts will favor either weak or strong turbulence processes depending on the intensity and bandwidth of the waves, though weak turbulence processes are thought to be dominant in Earth's foreshock [*Cairns et al.*, 1998], planetary foreshocks [*Cairns and Robinson*, 1992], and type II and III radio bursts [*Cairns and Robinson*, 1998; *Knock et al.*, 2001].

Electrostatic decay is a weak-turbulence process in which a Langmuir wave L decays to another Langmuir wave L' and an ion sound wave S (i.e., $L \rightarrow L' + S$). Conservation of energy and momentum gives

$$\omega_L = \omega_{L'} + \omega_S, \tag{1.18}$$

$$\mathbf{k}_L = \mathbf{k}_{L'} + \mathbf{k}_S, \tag{1.19}$$

respectively. For an unmagnetized plasma, dispersion relations (1.6) and (1.9) are substituted into (1.18) and (1.19) to obtain the kinematics. When $\mathbf{k}_L$ and $\mathbf{k}_{L'}$ are anti-parallel the rate of the process is maximized [*Melrose*, 1980a; *Cairns*, 1987a; *Robinson et al.*, 1993a], and the kinematics are given by

$$k_{L'} = -k_L + k_0, \tag{1.20}$$

$$k_S = 2k_L - k_0, \tag{1.21}$$

where $k_0 = 2\omega_p v_S / 3V_e^2$.

The nonlinear rate of electrostatic decay in the weak-turbulence regime can be obtained by appealing to detailed balance, which relates the rate of emission of waves to the rate of absorption. One can then derive the kinetic equations for the process $M \rightarrow P + Q$ (e.g. *Tsytovich* [1966]; *Melrose* [1980a, 1986a]):

$$\frac{\partial N_M(\mathbf{k})}{\partial t} = \int \frac{d^3\mathbf{k}'}{(2\pi)^3} \frac{d^3\mathbf{k}''}{(2\pi)^3} u_{MPQ}(\mathbf{k}, \mathbf{k}', \mathbf{k}'')$$
$$\times [N_P(\mathbf{k}')N_Q(\mathbf{k}'') - N_M(\mathbf{k})\{N_P(\mathbf{k}')N_Q(\mathbf{k}'')\}], \tag{1.22}$$

$$\frac{\partial N_P(\mathbf{k}')}{\partial t} = -\int \frac{d^3\mathbf{k}}{(2\pi)^3} \frac{d^3\mathbf{k}''}{(2\pi)^3} u_{MPQ}(\mathbf{k}, \mathbf{k}', \mathbf{k}'')$$
$$\times [N_P(\mathbf{k}')N_Q(\mathbf{k}'') - N_M(\mathbf{k})\{N_P(\mathbf{k}')N_Q(\mathbf{k}'')\}], \tag{1.23}$$

$$\frac{\partial N_Q(\mathbf{k}'')}{\partial t} = -\int \frac{d^3\mathbf{k}}{(2\pi)^3}\frac{d^3\mathbf{k}'}{(2\pi)^3} u_{MPQ}(\mathbf{k},\mathbf{k}',\mathbf{k}'')$$
$$\times [N_P(\mathbf{k}')N_Q(\mathbf{k}'') - N_M(\mathbf{k})\{N_P(\mathbf{k}')N_Q(\mathbf{k}'')\}], \quad (1.24)$$

where u_{MPQ} is proportional to the probability of the transition $M \to P + Q$ (which is equal to the probability of the transition $P + Q \to M$).

A closely related process to electrostatic decay is electromagnetic decay, represented by $L \pm S \to T$ (which collectively denotes $L + S \to T$ and $L \to S+T$), where T is a transverse wave. Proceeding in the same manner as before, the kinematics are given by [*Cairns*, 1987b]

$$k_T \approx \sqrt{3}\frac{V_e}{c}k_L, \qquad k_S \approx k_L. \qquad (1.25)$$

Equivalent phase-coherent (parametric) versions of the above processes also exist [*Melrose*, 1986b] with identical kinematics but different growth rates. In addition, for the above electrostatic and electromagnetic decay processes, the collective ion sound wave response can be replaced by the single particle response of a thermal ion. These processes are termed scattering off thermal ions [*Tsytovich*, 1970; *Melrose*, 1980a; *Muschietti and Dum*, 1991]. Here, a Langmuir wave scatters off the polarization cloud of an ion into either the Langmuir mode or the transverse mode.

The kinematics and dynamics of electrostatic decay has thus far in the literature been considered only in the unmagnetized limit. However, solutions of the wave equation in magnetized plasmas [*Willes and Cairns*, 2000], as well as *in situ* observations in the terrestrial foreshock [*Bale et al.*, 1998], show that plasma magnetization can significantly modifiy dispersion and polarization of the Langmuir mode (cf. 1.1.3). Furthermore, the range of validity for the unmagnetized approximation has not yet been addressed. In Chapters 3–5 we investigate the effect of magnetization on electrostatic decay through calculations of kinematics and quasilinear simulations.

1.3.3 Four-wave processes

While three-wave processes dominate in weak-turbulence theory, four-wave processes are important in strong turbulence when the waves have small k [*Zakharov*, 1972; *Robinson*, 1997]. One class of four-wave interactions is modulational instabilities, in which a spatially uniform Langmuir wave envelope breaks up into shorter wavelengths [*Vedenov and Rudakov*, 1964; *Vladimirov et al.*, 1995], corresponding to wave energy being pumped to larger k.

In the semiclassical framework, modulational instabilities correspond to two Langmuir quanta exchanging an ion sound quantum [*Melrose*, 1986a; *Robinson*, 1997]. Classically, localized enhancements in the electric field energy density of Langmuir waves expel plasma: firstly the more mobile electrons electrons via the ponderomotive force, then the ions through the resulting ambipolar electric field. This lower plasma frequency increases the refractive index of the Langmuir waves in that region, so they will refract into these cavities, resulting in self-focusing. This further intensifies and confines the Langmuir waves, fuelling the instability. This process can cause runaway wave collapse, where the waves are trapped in density wells of increasingly smaller length scales, increasing k until the waves are dissipated by Landau damping and transit time damping (both of which increase with k).

1.3.4   Langmuir eigenmodes

In the presence of density cavities or enhancements, localization of Langmuir waves can occur. This behavior can be described through the high-frequency Zakharov equation [*Ergun et al.*, 2008], assuming a preexisting density structure, e.g., a parabolic density cavity. The resulting equation for the wave electric field is analogous to the Schrodinger equation, the solutions of which are a set of discrete frequencies and associated eigenmode solutions. Localized Langmuir waves with fine frequency structure in the auroral ionosphere [*McAdams et al.*, 2000; *Yoon and LaBelle*, 2005] and the solar wind [*Ergun et al.*, 2008; *Malaspina and Ergun*, 2008; *Hess et al.*, 2010; *Graham and Cairns*, 2013a] have been interpreted in terms of these eigenmodes. Langmuir waves in eigenmodes can either be driven directly [*Hess et al.*, 2010] or form as the result of decay processes producing a low wavenumber condensate [*Henri et al.*, 2011] or result from refraction into density wells as in wave collapse. Stable eigenmodes are of necessity below the threshold energy density for wave collase.

Radio emission can be generated from Langmuir eigenmodes by a so-called antenna mechanism [*Malaspina et al.*, 2010, 2012]. Here, the electric field of the Langmuir wave **E** at a frequency near ω_p induces electron oscillations at ω_p and $2\omega_p$ that constitute a nonlinear current **J**. The work done by the field on the current, $-\mathbf{J} \cdot \mathbf{E}$, is a source term for the electromagnetic fields, which radiate as transverse waves at ω_p and $2\omega_p$. The efficiency of this process depends on the local plasma parameters and wavepacket properties such as spatial scale [*Hess et al.*, 2010; *Malaspina et al.*, 2010, 2012].

1.4   Observational context

1.4.1   Auroral waves

Earth's auroral ionosphere is located approximately 60–600 km above Earth's surface and at magnetic dipole latitudes of approximately 60°–80°. It is a region of intense radio emission and plasma wave generation by high energy auroral electrons. Both *in situ* and ground-based observations have identified numerous types of emissions, including the predominantly x-mode auroral kilometric radiation [*Gurnett*, 1974; *Melrose*, 1976; *Wu and Lee*, 1979], whistler-mode auroral hiss [*Gurnett*, 1966; *James*, 1976; *Gurnett et al.*, 1983; *Santolík et al.*, 2001], and auroral roar [*LaBelle et al.*, 1995; *Tsurutani et al.*, 1998; *Yoon et al.*, 1998; *LaBelle and Weatherwax*, 2002] emissions. These are driven by nonthermal features in the electron distribution function either parallel or perpendicular to Earth's magnetic field. Variation of the plasma density with altitude and the development of parallel electric fields via Alfvén wave reflection and other processes (e.g. *Chaston et al.* [1999]) leads to regions of both overdense ($\omega_p > \Omega_e$) and underdense ($\omega_p < \Omega_e$) plasma.

Both satellite [*Beghin et al.*, 1989] and sounding rocket [*McAdams and La-Belle*, 1999; *McAdams et al.*, 1999] experiments have observed certain types of emissions, termed HF (high-frequency) spikes, HF bands, and HF chirps, which were observed at, above, and below the local plasma frequency, respectively. These emissions were correlated with local energetic electron precipitation (i.e., earthward propagation). By comparing the observed wave frequencies with the dispersion relations of possible wave modes, it was proposed that electron beams drive Langmuir waves (HF spikes), which then undergo mode conversion to generate either whistler-mode waves (HF bands) or z-mode waves (HF chirps) [*Beghin et al.*, 1989; *McAdams and LaBelle*, 1999]. It was also suggested from theoretical arguments that such HF bands and chirps should become electrostatic as they propagate [*Beghin et al.*, 1989].

In Chapter 2 we investigate both the generation mechanism and expected polarization of these emissions. In particular, we analyze the wave modes of warm magnetized plasmas in order to determine whether a mode conversion process is necessary. We also use ray-tracing techniques to examine whether these emissions should become electromagnetic or whether they remain electrostatic as they propagate from their generation region into the observation site.
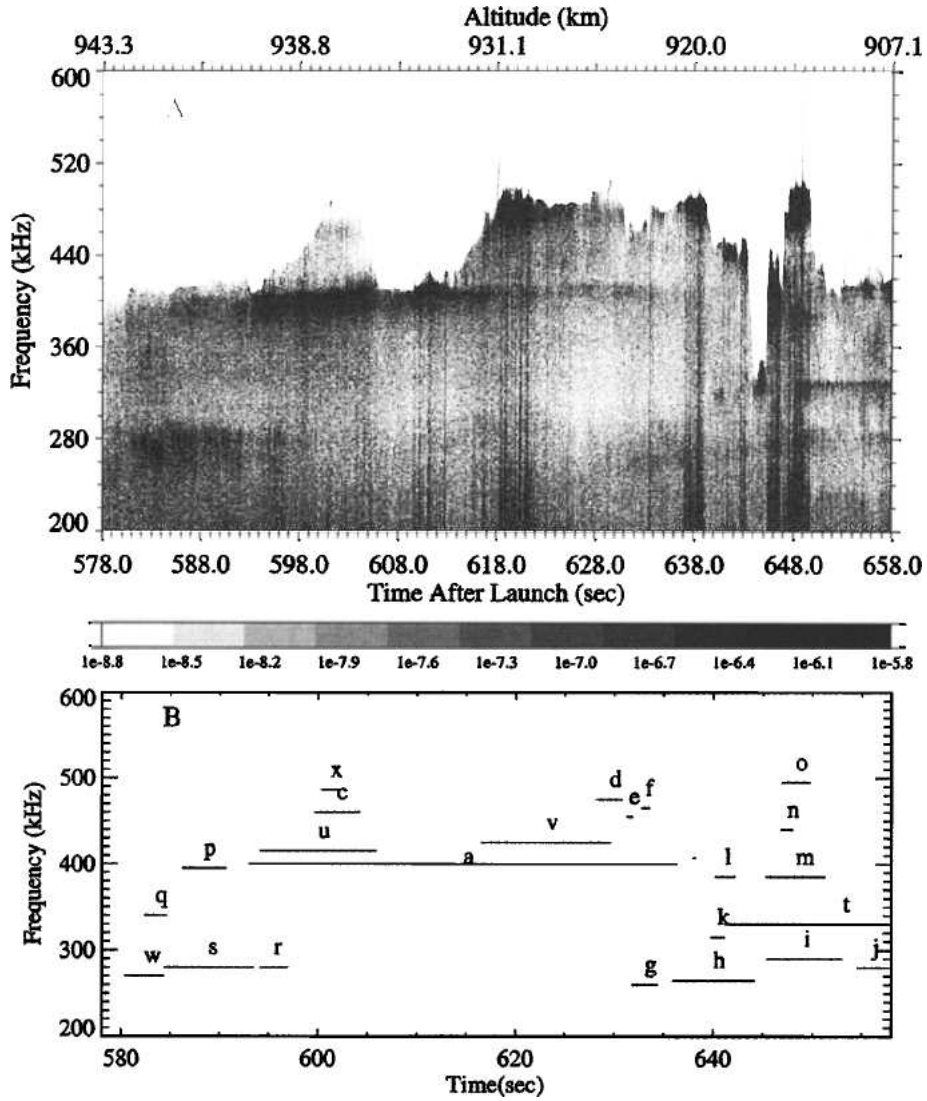
Figure 1.3: (a) HF spectrogram of Langmuir wave bursts, variation in the upper cutoff frequency (f_p), and many HF band emissions. (b) Identification and locations of HF band emissions. Read 1e−8.8 as $1 \times 10^{-8.8}$. Adapted from *McAdams and LaBelle* [1999].

1.4.2 Solar type III bursts

Type III solar radio bursts are intense radio emissions generated in the solar corona and interplanetary medium. They are distinguished from the other four main types of solar radio bursts by their fast negative frequency drift ($df/dt < 0$), short durations of a few seconds from ~ 200 MHz to 30 MHz, frequencies from several hundred MHz down to 20 kHz, and the common presence of harmonic structure (i.e., bands of emission at integer multiples of the lowest frequency) [*Wild*, 1950]. Such features can be seen in Fig. 1.4.

The standard interpretation of these frequency components is in terms of the plasma hypothesis, where fundamental and harmonic frequencies are identified as the local plasma frequency and twice that frequency, respectively. It is also widely accepted that the energy source for type III radio bursts is flare-accelerated electrons [*Scarf et al.*, 1971; *Gurnett and Anderson*, 1976; *Lin et al.*, 1986] of energies 1–100 keV which stream along interplanetary magnetic field lines. In this hypothesis the negative frequency drift is due to the local plasma frequency (density) decreasing as the beam propagates outwards from the Sun into the interplanetary medium. The process for generating type III bursts is presented schematically in Fig. 1.5.

Ginzburg and Zhelezniakov [1958] proposed the first quantitative theory for type III radio bursts, as follows. Energetic electrons streaming out from the Sun along magnetic field lines form a beam in velocity space due to advection. This nonthermal feature of the electron particle distribution drives Langmuir waves via a bump-on-tail instability (cf. Sec. 1.2.1). These Langmuir waves scatter off the electron polarization cloud around thermal ions into transverse waves, constituting fundamental radio emission near ω_p, or coalesce with oppositely-propagating thermal Langmuir waves to give harmonic radiation near $2\omega_p$.

It has since been recognized that this model cannot account for the observed brightness temperatures of the radiation [*Melrose*, 1980b]. This led *Melrose* [1982] and others to propose more efficient nonlinear wave-wave processes such as electrostatic and electromagnetic decay instead of induced scattering for fundamental emission, and coalescence of beam-driven Langmuir waves with nonthermal product (backscattered) Langmuir waves from the electrostatic decay process for second harmonic emission. The presence of Langmuir waves in type III bursts has been confirmed by *in situ* observations [*Gurnett and Anderson*, 1976; *Lin et al.*, 1986], and ion sound waves have also been detected that have wavelengths consistent with parametric or electrostatic decay [*Lin et al.*, 1986; *Cairns*, 1995; *Cairns and Robinson*, 1995a; *Henri et al.*, 2009].

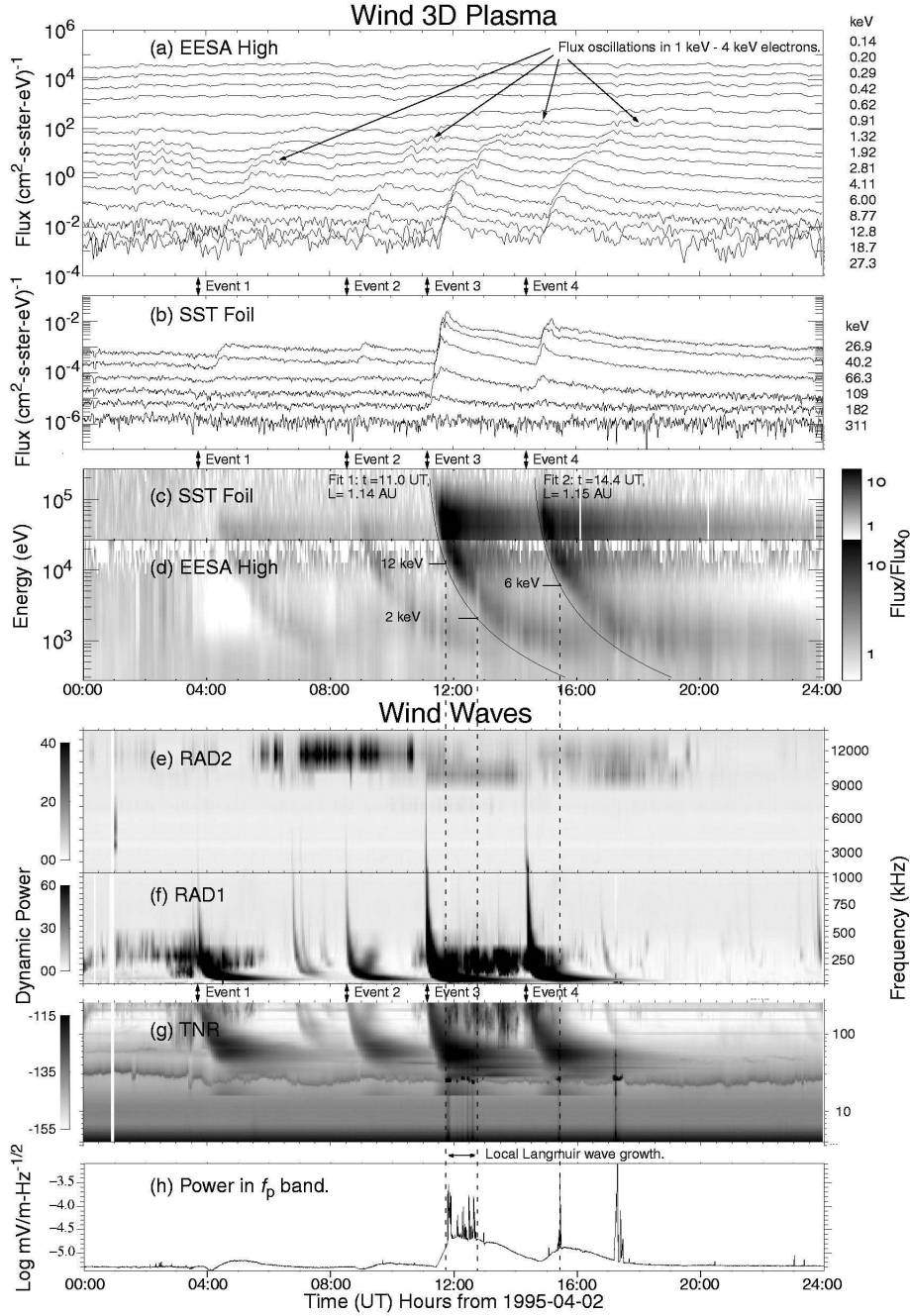Figure 1.4: Interplanetary type III radio bursts measured by WIND [*Ergun et al.*, 1998]. (a, b) Electron fluxes. (c, d) Relative change in electron fluxes (F/F_0), from a reference flux (F_0). (e, f, and g) Dynamic spectrum of radio emissions with power relative to cosmic background. (h) Electric-field wave power in the frequency band (19–41.5 kHz) encompassing the local Langmuir frequency.
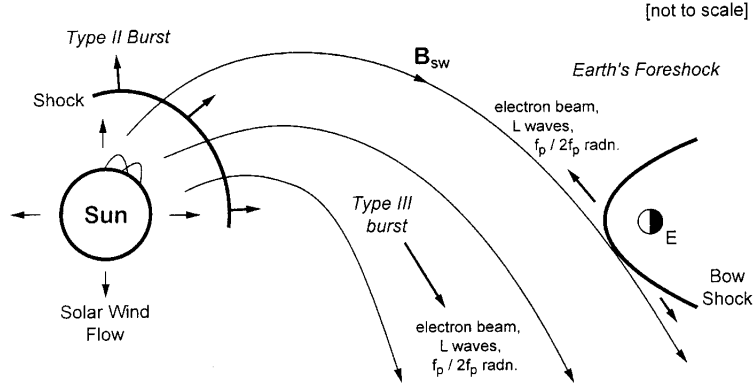
Figure 1.5: Schematic illustration of the source regions and phenomena involved in type II and III solar radio bursts in the corona and solar wind and those observed in Earth's foreshock. From *Cairns et al.* [2000a].

Various other theories of type III radio emission have been proposed in the literature: electron cyclotron maser emission [*Wu et al.*, 2002], linear mode conversion [*Field*, 1956; *Hinkel-Lipsker et al.*, 1992; *Kim et al.*, 2007, 2008], radiation at f_p and $2f_p$ from localized Langmuir waves [*Malaspina et al.*, 2010, 2012], nonlinear beam instabilities [*Yoon*, 1995], and modulational instabilities and wave collapse [*Papadopoulos et al.*, 1974; *Thejappa et al.*, 2012a,b]. The latter are disputed based on nonlinear thresholds derived from observed wave-forms, and spectra and detailed fits of theoretical wavepacket structure to these observed waveforms [*Cairns and Robinson*, 1995b; *Nulsen et al.*, 2007; *Graham et al.*, 2012a,b].

Theories for type III bursts must also account for Sturrock's dilemma [*Sturrock*, 1964; *Melrose*, 1980a], namely that in the absence of a mechanism for removing resonant Langmuir waves, quasilinear relaxation should flatten non-thermal features of the electron distribution long before the electrons reach the observed distances of 1 AU and greater. In addition to the nonlinear mechanisms above, other mechanisms such as stochastic growth theory (SGT) [*Robinson*, 1992; *Robinson et al.*, 1993b] have been proposed. In SGT it is argued that density fluctuations in the solar wind often suppress the growth of Langmuir waves through refraction away from resonance, such that high lev-els of Langmuir waves occur only in localized clumps and the electron beam fluctuates around marginal stability.

Strong evidence exists for SGT in type III radio sources [*Robinson et al.*, 1993b], principally involving the observed field statistics satisfying the lognor-mal prediction for the probability distribution of electric field strength $P(E)$.

Similar results are found in planetary foreshocks [*Cairns and Robinson*, 1997, 1999; *Cairns et al.*, 2000b] and for Langmuir waves in Earth's auroral iono-sphere [*Samara et al.*, 2008; *LaBelle et al.*, 2010]. SGT can also co-exist with nonlinear processes, with SGT dominant at low to moderate wave fields below the nonlinear threshold and nonlinear processes at high wave fields above the nonlinear threshold [*Robinson et al.*, 1993b; *Cairns and Robinson*, 1997, 1998, 1999].

Simulations of type III bursts employing the aforementioned processes have been reported in the literature. For example, *Li et al.* [2002, 2008] have per-formed large-scale quasilinear simulations of coronal and interplanetary type III bursts, including nonlinear electrostatic and electromagnetic decay processes. Semiquantitative agreement was found between observed and predicted features of dynamic spectra such as frequency drift rate, radio flux, brightness temper-ature, and temporal profile of the radiation. Smaller-scale ($\sim 10^3$–$10^4 \lambda_D$) sim-ulations focusing on particular aspects of type III generation mechanisms have also been performed. *Henri et al.* [2010] investigated the electrostatic decay of localized Langmuir wavepackets through Vlasov-Poisson simulations using typical solar wind parameters. They found nonlinear thresholds of electro-static decay consistent with inferred thresholds from STEREO data, providing evidence for the electrostatic decay process being relevant to type III bursts.

Recently, the STEREO spacecraft have provided *in situ* measurement of all three components of wave electric fields in type III sources, allowing mea-surement of Langmuir-wave polarization [*Bougeret et al.*, 2008]. About 40% of events display beating Langmuir waveforms and have split spectral peaks [*Malaspina et al.*, 2010; *Graham and Cairns*, 2013b], which has recently been interpreted as evidence for electrostatic decay [*Graham and Cairns*, 2013b]. Events associated with slower electron beams ($v_b \lesssim 0.1c$) have electric fields $\mathbf{E}$ predominantly aligned with the background magnetic field $\mathbf{B}_0$. However, events associated with faster beam speeds ($v_b \gtrsim 0.1c$) often have one spectral peak with $\mathbf{E}$ nearly perpendicular to $\mathbf{B}_0$, inconsistent with the properties of unmagnetized Langmuir waves but consistent with Langmuir-z waves at low k [*Malaspina et al.*, 2010; *Graham and Cairns*, 2013b]. In Chapter 3 we pro-pose a mechanism for generating such waves, based on electrostatic decay of Langmuir-z waves in a magnetized plasma, and develop this mechanism in detail in Chapters 4 and 5.

Chapter 2

Changes in mode properties versus mode conversion for waves in Earth's auroral ionosphere

2.1 Abstract

The generation mechanism and properties of auroral waves near, above, and below the electron plasma frequency ω_{pe} are investigated. Calculations of wave dispersion in a warm, magnetized plasma show that these waves propagate in a single mode, the generalized Langmuir-z mode or generalized Langmuir-whistler mode of magnetized kinetic plasma theory, depending on whether ω_{pe} exceeds or is less than the electron gyrofrequency Ω_e, respectively. The characteristics of the modes change as the waves propagate through density gradients and move to lower or higher wave numbers. This corrects previous assertions that these waves undergo a conversion between distinct Langmuir and whistler or Langmuir and z modes. Using ray-tracing techniques, it is predicted that both the waves below ω_{pe} and above ω_{pe} should remain predominantly electrostatic, in contrast to previous interpretations of these waves becoming electromagnetic.

2.2 Introduction

Plasmas support a variety of wave modes, the number and characteristics of which are determined by plasma properties such as temperature, magnetiza-

tion, and particle distribution functions. Properties of these modes can be derived using fluid or kinetic theory and Maxwell's equations. For instance, cold magnetized electron plasmas are described by magnetoionic theory at high frequencies, and its wave modes are the o, x, whistler, and z modes. If instead the plasma is unmagnetized and has a Maxwellian particle distribution, then the corresponding wave modes include the Langmuir mode and transverse mode [*Stix*, 1962; *Melrose*, 1980a].

While the wave modes described above are distinct for a homogeneous plasma, there are numerous mechanisms by which wave energy can be transferred between modes. One such mechanism is linear mode conversion [*Budden*, 1961; *Oya*, 1971; *Jones*, 1976a; *Bell and Ngo*, 1988, 1990; *Hinkel-Lipsker et al.*, 1992; *Willes and Cairns*, 2001; *Kim et al.*, 2007], which involves the conversion of waves propagating in a density gradient. Complex-valued modes arise in the inhomogeneous region, connecting previously uncoupled modes at a single point in frequency-wave number space. Wave energy can couple to these evanescent modes and then be reflected from the density gradient in a different mode which also couples to them. Linear mode conversion can be relevant to waves described by unmagnetized and magnetized kinetic wave theory, magnetoionic theory, and fluid theory [*Stix*, 1962].

Nonlinear mechanisms [*Sagdeev and Galeev*, 1969; *Tsytovich*, 1970; *Melrose*, 1980a; *Sitenko*, 1982] also permit mode conversion. Some nonlinear wave-wave interactions involve coalescence of two waves (possibly in different modes) into a third wave (again, possibly in a separate mode). Similarly, there can also be decay of one wave into two, which can result in conversion of wave energy into distinct modes.

The focus of this chapter is a specific mode-conversion process invoked by *Beghin et al.* [1989], *McAdams and LaBelle* [1999], and *McAdams et al.* [1999] to explain their observations of waves in the auroral ionosphere. These workers observed waves near the angular electron plasma frequency ω_{pe} in both overdense and underdense (defined as $\Omega_e < \omega_{pe}$ and $\Omega_e > \omega_{pe}$, respectively) regions of the auroral ionosphere. Their observations were interpreted in terms of the following "mode conversion" involving Langmuir waves and either whistler waves or z-mode waves:

(i) electron beams generate electrostatic Langmuir waves near ω_{pe};

(ii) the Langmuir waves propagate into regions of different plasma density; and

(iii) the waves convert to either whistler waves or z-mode waves depending on the degree of magnetization of the plasma.

Further details of these observations and generation mechanisms are provided in Sec. 2.3 and Sec. 2.4.

More recently *Willes and Cairns* [2000] re-examined the dispersion characteristics of waves in a warm, magnetized plasma, and their relation to the magnetoionic whistler and z modes and the kinetic Langmuir mode. These results are not well known, but have direct relevance to the observations of *Beghin et al.* [1989], *McAdams and LaBelle* [1999] and *McAdams et al.* [1999], and form the crux of this chapter. We detail the results of *Willes and Cairns* [2000] in Sec. 2.2.

Below we address several issues that arise with the mode-conversion mechanism of *Beghin et al.* [1989], *McAdams and LaBelle* [1999], and *McAdams et al.* [1999]. For both sets of observations, we reinterpret the mode identification using the results from *Willes and Cairns* [2000] and our own solutions of the general kinetic dispersion equation. This allows us to discuss the proposed generation mechanisms and to show that no mode-conversion process is necessary. We also analyze the polarization properties of the modes and compare the results with previous predictions.

The organization of the chapter is as follows. In Sec. 2.2, wave modes and their dispersion properties are summarized for different plasma approximations, with emphasis on the wave modes of magnetized kinetic plasmas and the results of *Willes and Cairns* [2000]. In Sec. 2.3 we outline the observations presented by *Beghin et al.* [1989] and their corresponding generation mechanism and "mode conversion". Using the results of Sec. 2.2, we demonstrate that no mode-conversion process is necessary to explain the observations of *Beghin et al.* Instead, these waves propagate in a single mode — either the generalized Langmuir-z mode or the generalized Langmuir-whistler mode — whose properties change with altitude and the plasma parameters. In other words, the waves stay in the same mode as they propagate, while their polarization properties and wave vector change with position. Numerical ray-tracing calculations are also performed to investigate the evolution of the electromagnetic properties of whistler-mode and z-mode wave packets in the auroral ionosphere. Section 2.4 contains our analysis of the results of *McAdams and LaBelle* [1999] and *McAdams et al.* [1999], where we similarly show that mode conversion is not needed to account for their observations of waves near ω_{pe}. Section 2.5 contains a discussion and the conclusions.

2.3 Plasma theory

Wave modes and their properties are determined by the plasma in which they propagate [*Stix*, 1962; *Tsytovich*, 1970; *Melrose*, 1980a]. Simplified models of the plasma are often employed to facilitate analytic calculations of wave properties. An unmagnetized, cold electron fluid supports the Langmuir mode and the transverse electromagnetic mode. The Langmuir mode oscillates at the angular electron plasma frequency $\omega_{pe} = (ne^2/m_e\epsilon_0)^{1/2}$, where n is the electron number density, e is the charge of the electron, and m_e is the mass of the electron [*Tonks and Langmuir*, 1929]. The electromagnetic mode has the dispersion relation $\omega_T^2 = \omega_{pe}^2 + k^2c^2$ (e.g. [*Stix*, 1962; *Chen*, 1974]), where ω_T is the wave angular frequency, k is the wave number, and c is the speed of light in free space.

If the temperature of the plasma is sufficiently high that the cold plasma model is not valid, then thermal corrections to the analysis must be included. These thermal effects do not affect the electromagnetic mode, but the Langmuir mode's dispersion is modified to $\omega_L^2 \approx \omega_{pe}^2 + 3k^2V_e^2$ [*Bohm and Gross*, 1949], where V_e is the electron thermal speed. As can be seen from their dispersion relations, both the electromagnetic mode and the Langmuir mode are restricted to frequencies above ω_{pe}.

In contrast, magnetoionic theory [*Hartree*, 1931; *Appleton*, 1932] ignores ion and thermal effects, assuming a cold electron fluid that is permeated by a static magnetic field. This yields the o and x modes, which are the magnetized counterparts of the free-space transverse mode, and the whistler and z modes. The whistler mode is the lowest-frequency magnetoionic mode, and exists at frequencies from its cutoff frequency

$$\omega_{wc}(\theta) = 0 \tag{2.1}$$

up to its resonance frequency

$$\omega_{wr}(\theta) = \left[\frac{1}{2}(\omega_{pe}^2 + \Omega_e^2) + \frac{1}{2}\sqrt{(\omega_{pe}^2 + \Omega_e^2)^2 - 4\omega_{pe}^2\Omega_e^2\cos^2\theta}\right]^{1/2}, \tag{2.2}$$

where θ is the angle between the wave vector $\mathbf{k}$ and the background magnetic field $\mathbf{B}_0$, and Ω_e is the angular electron cyclotron frequency. Thus the whistler mode is confined to frequencies below the minimum of ω_{pe} and Ω_e. The z mode is a higher-frequency mode, with left-hand polarization below ω_{pe} and right-hand polarization above ω_{pe}. The (low-frequency) cutoff frequency of the

z mode is

$$\omega_{zc} = \frac{1}{2}\sqrt{\Omega_e^2 + 4\omega_{pe}^2} - \frac{1}{2}\Omega_e, \tag{2.3}$$

and its resonance frequency is

$$\omega_{zr}(\theta) = \left[\frac{1}{2}(\omega_{pe}^2 + \Omega_e^2) - \frac{1}{2}\sqrt{(\omega_{pe}^2 + \Omega_e^2)^2 - 4\omega_{pe}^2\Omega_e^2\cos^2\theta}\right]^{1/2}. \tag{2.4}$$

For propagation very near parallel ($\theta \approx 0$) in magnetoionic theory, the z-mode and o-mode dispersion relations approach the same frequency and wave number at $\omega = \omega_{pe}$ and $kc/\omega_{pe} = (1 + \omega_{pe}/\Omega_e)^{-1/2}$, allowing conversion of wave energy between the modes. This coupling point is the well-known first Ellis window [*Ellis*, 1956; *Yoon et al.*, 1998]. For exactly parallel propagation ($\theta = 0$), the z mode and o mode dispersion relations merge at this coupling point and form a combined z/o mode. If $\Omega_e > \omega_{pe}$ for nearly parallel propagation, then there is analogous coupling between the z mode and the whistler mode at a higher wave number $kc/\omega_{pe} = (1 - \omega_{pe}/\Omega_e)^{-1/2}$ (called the second Ellis window) [*Jones*, 1976b; *Yoon et al.*, 1998], and formation of a combined whistler/z mode when $\theta = 0$. In both cases, for $\theta = 0$ the dispersion relation $\omega = \omega_{pe}$ is a solution of the magnetoionic dispersion equation for all k; that is, the unmagnetized cold Langmuir mode reappears ($V_e = 0$). However, for $\theta > 0$ a single continuous Langmuir mode is not a solution in magnetoionic theory.

A more general analysis of plasma waves includes both magnetic and thermal effects, and can be achieved with the kinetic Vlasov description of a plasma. The wave modes and their properties in this case have been investigated by previous workers, e.g. *Stix* [1962], *Melrose* [1980a], and *André* [1985], who calculate dispersion relations for all angles of propagation and for a range of plasma parameters. Here, our focus is on the relationship between the thermal modes and magnetoionic modes described above and the modes in a kinetic magnetized plasma. This has been studied both analytically [*Melrose*, 1976, 1980a] and, more recently, numerically [*Willes and Cairns*, 2000]. The latter showed that distinct Langmuir and magnetoionic modes no longer exist in a kinetic magnetized plasma. Instead, in the overdense regime the magnetoionic whistler mode remains, but a generalized Langmuir-z mode appears and replaces the previously distinct Langmuir and z modes. This mode has Langmuir-like dispersion for high k and magnetoionic z mode dispersion for low k. Conversely, in the underdense regime there is a distinct z mode and a generalized Langmuir-whistler mode, which replaces the previously distinct Langmuir and whistler modes and has whistler-like dispersion for low k and Langmuir-like dispersion for high k.

We now confirm the results of *Willes and Cairns* [2000] on the existence of combined Langmuir-z and combined Langmuir-whistler modes for oblique propagation angles. For the Langmuir-z mode, we numerically solve the general kinetic dispersion equation using nominal parameters for the auroral ionosphere: $\omega_{pe}/\Omega_e = 1.2$, $V_e/c = 7 \times 10^{-4}$, and $\theta = 1°, 20°$. These solutions are compared with numerical calculations of the dispersion of the magnetoionic z mode and the thermal Langmuir mode in Figs 2.1(a) and 2.1(b). Magnetoionic theory (circles) provides a good approximation to the dispersion of the Langmuir-z mode (solid line) for low k and both θ. As k increases, the thermal Langmuir mode (filled squares) better approximates the Langmuir-z dispersion. The Langmuir-z mode is thus unlike the combined magnetoionic z/o and whistler$/z$ modes that occur for the radio windows described above; the Langmuir-z mode is a single mode that exists for all oblique propagation angles, whereas the combined z/o mode is present only for a very narrow range of θ.

Our calculations for the Langmuir-whistler mode are performed using the same parameters, except that $\omega_{pe}/\Omega_e = 0.8$. The results are shown in Figs 2.1(c) and 2.1(d). For low k the whistler-mode dispersion relations obtained from magnetoionic theory (circles) are a good approximation to the Langmuir-whistler mode (short-dashed line); at high k the dispersion of the Langmuir-whistler mode resembles the thermal Langmuir mode (filled squares). In a similar manner to the overdense regime in Figs 2.1(a) and 2.1(b), distinct Langmuir and whistler modes do not exist in a thermal magnetized plasma.

These results are crucial for understanding the properties and evolution of waves in kinetic magnetized plasmas, both in the underdense and overdense regimes.

2.4 Auroral waves of Beghin et al.

Beghin et al. [1989] presented observations of high-frequency waves in the auroral ionosphere from the AUREOL/ARCAD 3 satellite, for both overdense and underdense plasma conditions at altitudes of 400–2000 km. Three types of emissions were observed:

(A) narrowband emissions near the local value of ω_{pe}, termed "HF spike" emissions, identified as electrostatic Langmuir waves;

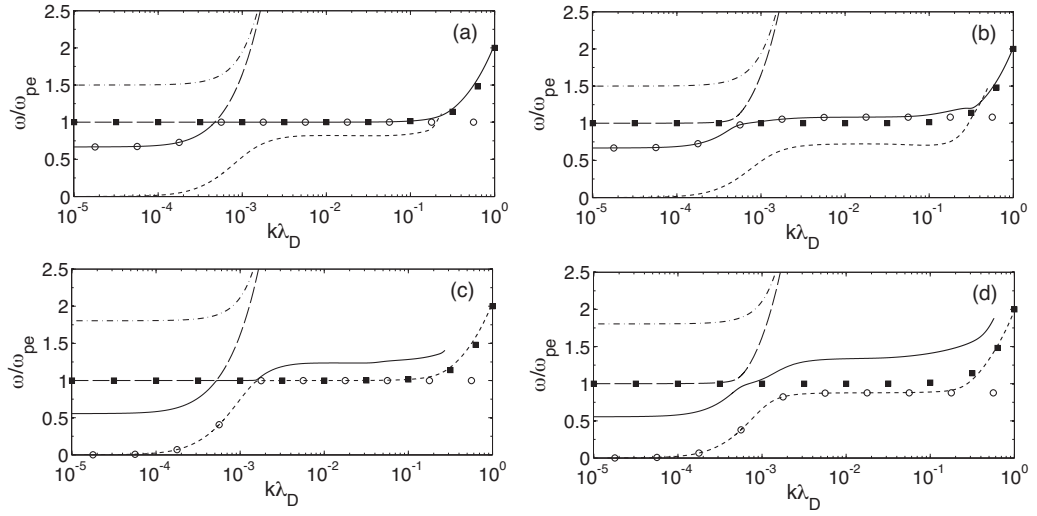(B) wideband emissions below the local value of ω_{pe}, identified as electromagnetic whistler waves; and

Figure 2.1: Dispersion relations $\omega(k)$ for (a) $\omega_{pe}/\Omega_e = 1.2$, $\theta = 1°$, (b) $\omega_{pe}/\Omega_e = 1.2$, $\theta = 20°$, (c) $\omega_{pe}/\Omega_e = 0.8$, $\theta = 1°$, and (d) $\omega_{pe}/\Omega_e = 0.8$, $\theta = 20°$. Numerical calculations of dispersion using magnetized kinetic theory are represented by long-dashed lines (o mode), dash-dotted lines (x mode), solid lines (mode with z-type dispersion at low k), and short-dashed lines (mode with whistler-type dispersion at low k). Also shown are the thermal Langmuir mode's approximate dispersion relation (filled squares) and calculations of dispersion using magnetoionic theory (circles) for the z-mode in (a) and (b) and whistler mode in (c) and (d). Modes cease to be plotted if damping becomes strong, defined here as $\text{Im}(\omega) < -\text{Re}(\omega)$.

(C) wideband emissions between the local value of ω_{pe} and the upper hybrid frequency ω_{uh}, identified as electromagnetic z-mode waves.

The wave modes were inferred from the values of the ratios ω/ω_{pe} and Ω_e/ω_{pe} and the cutoff and resonance frequencies predicted by magnetoionic theory. Since *Beghin et al.* [1989] had only electric field data (not magnetic field data) for these emissions, the polarizations were not measured directly, but were inferred from ω/ω_{pe}, Ω_e/ω_{pe}, and the known properties of magnetoionic modes.

2.4.1 Mode conversion

Beghin et al. [1989] postulated the generation mechanism for the above emissions to be:

(i) electron beams drifting parallel to $\mathbf{B}_0$ drive electrostatic Langmuir waves near the local value of ω_{pe} at a range of altitudes in the source region, observed as the emissions in (A) above;

(ii) the waves propagate into regions of the ionosphere with different ω_{pe};

(iii) the waves are observed by the satellite as wideband emissions and interpreted as either whistler-mode waves for (B) above or z-mode waves for (C) above in underdense or overdense regions of the ionosphere, respectively.

Point (i) was supported by instability calculations for waves in a warm, magnetized plasma with an isotropic Maxwellian background component and a weaker isotropic Maxwellian beam drifting parallel to $\mathbf{B}_0$ [*Beghin et al.*, 1989]. To facilitate their calculations they employed the electrostatic approximation [*Stix*, 1962], which is valid for high k. Calculations were performed for two sets of parameters: one for an underdense plasma ($\omega_{pe}/\Omega_e = 1.2$), and the other for an overdense plasma ($\omega_{pe}/\Omega_e = 0.8$). The dispersion relations and growth rates calculated by *Beghin et al.* [1989] are displayed in Figs 2.2 and 2.3 for the underdense and overdense cases, respectively. These calculations predict that the "whistler" mode has a positive growth rate for underdense parameters, and similarly for the "z mode" in overdense conditions.

Several features of the above warm plasma dispersion relations differ from magnetoionic predictions. Firstly, Beghin et al.'s cutoff frequencies $\Omega(K_\parallel = 0)$ in Figs 2.2 and 2.3 are θ-dependent. However, cutoff frequencies predicted by magnetoionic theory for the whistler and z modes, given by (2.1) and (2.3),
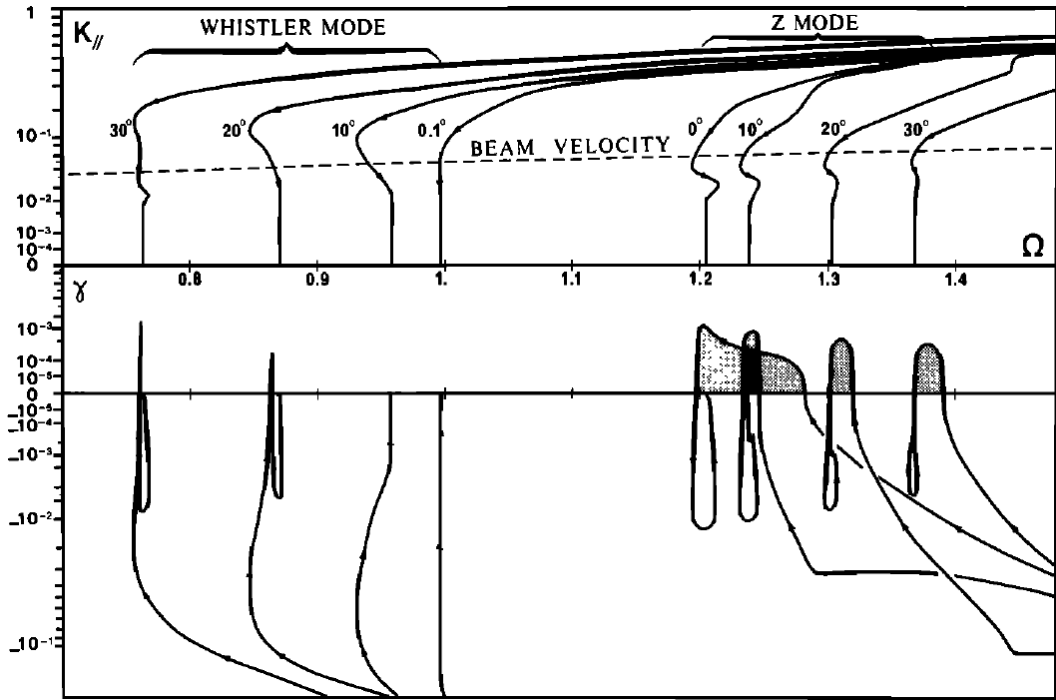
Figure 2.2: Beghin et al.'s dispersion relations (top) and corresponding growth rates (bottom) for $\omega_{pe}/\Omega_e = 1.2$. Here $K_\parallel = kV_e \cos\theta/\Omega_e$ is the normalized parallel wave number, $\Omega = \text{Re}(\omega)/\Omega_e$ is the normalized frequency, and $\gamma = \text{Im}(\omega)/\Omega_e$ is the normalized growth rate. Reproduced from Fig. 2.11 in *Beghin et al.* [1989].
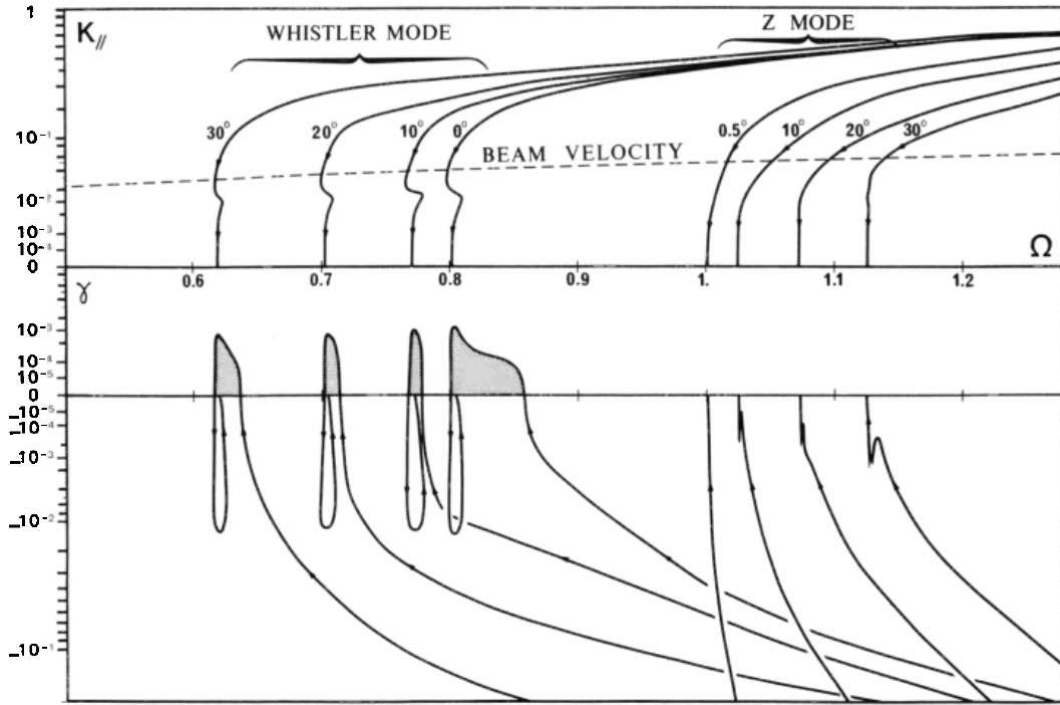
Figure 2.3: Same as Fig. 2.2, except $\omega_{pe}/\Omega_e = 0.8$. Reproduced from Fig. 2.12 in *Beghin et al.* [1989].

respectively, are independent of θ. This is required for all modes, since θ is not uniquely defined at $k = 0$ [*Robinson*, 1986]. Our solutions of the electrostatic and fully electromagnetic dispersion equation (not provided) indicate that the incorrect cutoff frequencies in Figs 2.2 and 2.3 are the result of applying the electrostatic approximation, which is inaccurate for low values of k.

Secondly, whistler-mode and z-mode frequencies in magnetoionic theory are bounded above by the resonance frequencies given by (2.2) and (2.4), respectively. Conversely, to a good approximation the dispersion curves in Figs 2.2 and 2.3 are bounded below by the magnetoionic resonance frequencies, and have no upper frequency bound, although they are strongly damped as Ω increases. Unlike the cutoff frequencies, this behavior cannot be the result of the electrostatic approximation, which is valid for large k.

These inconsistencies with magnetoionic theory were not commented on by *Beghin et al.* [1989]. Here, we present our interpretation of the modes based on the work of *Willes and Cairns* [2000] and solutions of the electromagnetic warm magnetized dispersion equation.

As stated in Sec. 2.2, distinct (magnetoionic) whistler and z modes do not typically exist when one considers a warm, magnetized plasma, which is the general case considered here. Instead, for an overdense plasma (see Fig. 2.2), the wave modes include the whistler mode and the generalized Langmuir mode (here, the combined Langmuir-z mode). Interpreting Beghin et al.'s "z mode" as the generalized Langmuir-z mode, the characteristics for large k are easily understood as being Langmuir-like, while the "z-mode" waves can also be on the Langmuir-z mode but now at lower k with ω above the local ω_{pe}. Thus, Langmuir-z waves generated by the electron beam appear Langmuir-like in the source region but then propagate into a higher-density region, preserving ω but moving to higher ω/ω_{pe} and lower k while still on the same mode and yet now having z-mode-like character. That is, the waves stay in the same mode but move to lower k where the mode character is different.

We propose a similar interpretation for the "whistler mode" in Fig. 2.3. In this interpretation, the "whistler mode" waves of Beghin et al. are in fact in the combined Langmuir-whistler mode at low k, as predicted in Fig. 2.1, while the HF spikes they observed are driven on the same mode at high k where the mode is Langmuir-like. Again propagation effects in a density gradient lead to waves on the same mode having very different characteristics and being incorrectly identified as being in different magnetoionic or unmagnetized thermal kinetic wave modes.

These interpretations allow us to explain why "spike-like emissions near f_{pe} are most likely electrostatic, like the similar phenomena called plasma resonances or longitudinal Langmuir oscillations" [*Beghin et al.*, 1989], and are still on the same mode as the whistler-like or z-mode-like waves at low k: the waves are driven at high k, where the generalized Langmuir wave has Langmuir-like characteristics, but move to low k due to propagation into regions with higher plasma density. We note that in both the underdense and overdense cases, wave growth resulting from the interaction of a relatively weak electron beam is always on the generalized Langmuir mode (whether Langmuir-z or Langmuir-whistler) and never on the magnetoionic mode that remains distinct (whistler or z mode, respectively), as found by *Willes and Cairns* [2000] and confirmed by our calculations (not shown here). Furthermore our calculations confirm the growth rates and real frequencies found by *Beghin et al.* [1989] in their Figs 11 and 12, with the correction that the unstable mode is the generalized Langmuir mode. Accordingly, there is no need to provide additional figures for the wave growth here. For a suitably strong beam the growth can be on a "beam mode" with $\omega \sim k v_b$ [*Melrose*, 1980a; *Gary*, 1985; *Willes and Cairns*, 2000] instead but the standard expectation is that wave energy moves into the generalized Langmuir mode (conserving frequency) at times when or in spatial regions where the beam weakens and disappears, since the beam mode is then not a solution of the dispersion equation and the energy will otherwise be reabsorbed by the plasma.

There is a question of whether one would expect auroral electron beams to drive waves near the lower hybrid frequency (ω_{LH}) rather than near ω_{pe}, since waves near ω_{LH}, such as auroral hiss and "spikelet" emissions, are often observed in the presence of energetic electron beams (e.g. [*Kintner et al.*, 1992; *Vago et al.*, 1992; *McAdams et al.*, 1998]). However, these emissions are generally considered to be driven in the whistler mode near ω_{pe} and thereafter propagate downwards into higher plasma density where they are observed near the local ω_{LH} [*Swift and Kan*, 1975], rather than being driven directly at ω_{LH}.

The identification of the observed waves as generalized Langmuir waves has major implications for other statements made by Beghin et al. For instance, they stated that there is a mode-coupling mechanism which allows the narrowband emissions to convert to wideband emissions. However, we have shown above that the observed waves are expected to be generated and propagate only in the generalized Langmuir mode, which has Langmuir-like character at high k and the appropriate whistler or z-mode character at low k. It is therefore unnecessary to invoke a mode-conversion process to explain the observation of

both narrowband and wideband emissions, as these waves simply propagate in a single mode whose characteristics change as the waves propagate through the inhomogeneous plasma.

2.4.2   Wideband and narrowband polarization

Here, we examine the polarization of the waves described by *Beghin et al.* [1989]. This involves modeling the dispersion properties and propagation of "z mode" and "whistler mode" waves by solving the dispersion equation and performing ray-tracing calculations. The focus is on whether Beghin et al.'s spike and wideband emissions are indeed electrostatic and electromagnetic, respectively.

We assume an Earth-centered magnetic dipole, a vertically stratified slab model for the auroral ionospheric plasma, and wave propagation in a magnetic meridian plane. The plasma density is assumed to depend only on altitude h, decreasing monotonically with increasing h. The magnetic field $\mathbf{B}_0$ is inclined at an angle ψ to the slab normal, and we assume that ψ remains constant for the waves during propagation. These assumptions allow us to employ Poeverlein's construction [*Poeverlein*, 1950; *Budden*, 1961] for ray tracing in a stratified medium.

The parameters we use in our investigation are the nominal parameters of *Beghin et al.* [1989], as follows. We consider plasma temperatures $T_e = T_i = 1000\,\mathrm{K}$. We take invariant latitudes of 65° to 85° and altitudes of 400 to 2000 km. Then ψ (which depends on h and Λ_0) lies in the range 3° to 15°, as shown in Fig. 2.4. An electron beam is assumed to drive waves at $\mathbf{k}$ nearly parallel to $\mathbf{B}_0$, i.e., $\theta \approx 0$. However, since $\theta = 0$ is a special case for mode structure (as described above in Sec. 2.2), we take a small but nonzero angle of $\theta = 1°$ for our calculations. The electron beam speed is taken to be $v_b = 6 \times 10^6$ m s^{-1}, which gives the refractive index of the waves being initially $n = 50$.

We now calculate the evolution of the wave's refractive index during propagation. Defining a refractive-index vector $\mathbf{n} = c\mathbf{k}/\omega$ and a unit vector $\hat{\mathbf{s}}$ that is parallel to the slab, Snell's law states that $\mathbf{n} \cdot \hat{\mathbf{s}}$ is constant. We choose a 2-D coordinate system whose axes are aligned parallel and perpendicular to $\mathbf{B}_0$, such that $\mathbf{n} = (n_\parallel, n_\perp) = (n\cos\theta, n\sin\theta)$ and $\hat{\mathbf{s}} = (\sin\psi, \cos\psi)$. Snell's law then becomes

$$n_\parallel + n_\perp \tan\psi = \text{constant}, \qquad (2.5)$$

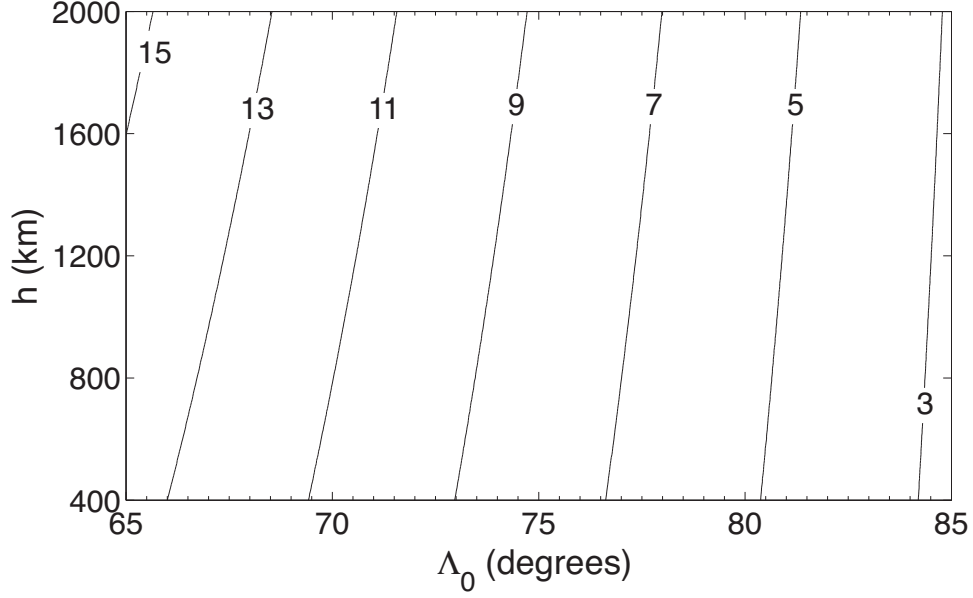which gives straight lines in $(n_\parallel, n_\perp)$-space as illustrated in Fig. 2.5 for a range of ψ values.

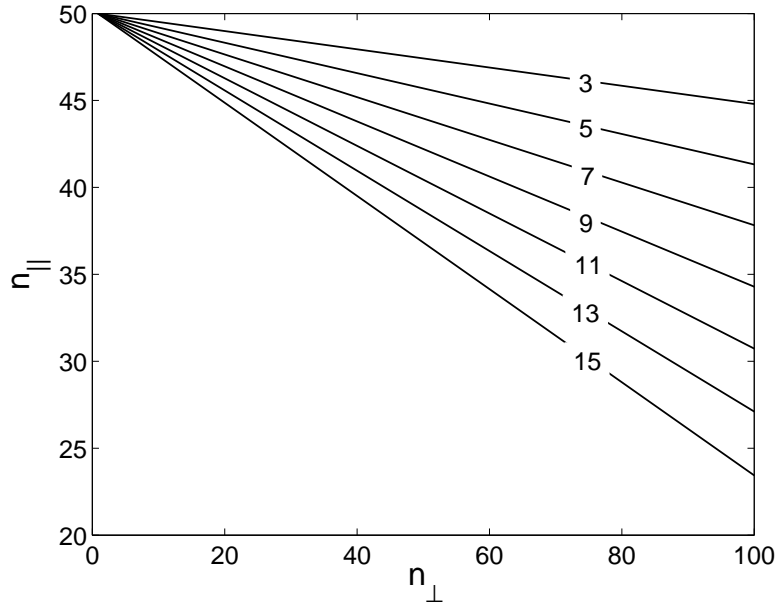Figure 2.4: Contour plot of ψ (degrees) as a function of Λ_0 and h.

Figure 2.5: Poeverlein's construction for waves generated with $n = 50$ and $\theta = 1°$. Lines represent the paths of wave packets in refractive-index space for the labeled values of ψ (degrees) from the initial point at $(n_\parallel, n_\perp) = (50\cos 1°, 50\sin 1°)$.
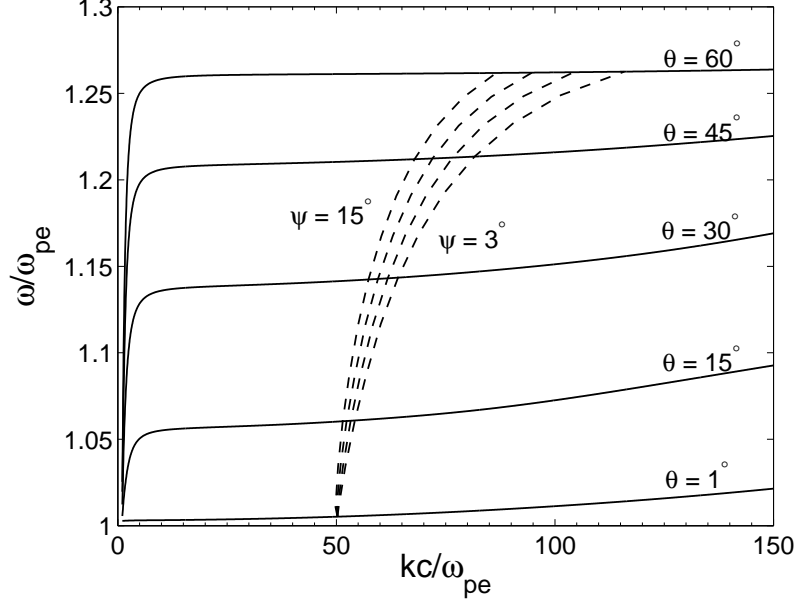
Figure 2.6: Numerically calculated dispersion relations $\omega(k)$ for the Langmuir-z mode, for a range of propagation angles θ. Dashed lines demonstrate evolution of wave number and frequency for ψ between $3°$ and $15°$ in increments of $4°$.

As the waves propagate with constant ω and ψ but varying $\omega/\omega_{pe}(h)$ and $\mathbf{k}(h)$, θ increases from its initial value of $1°$. To relate the as yet unknown evolution of ω/ω_{pe} and k to the known evolution of $n(\theta)$, we numerically calculate the dispersion relation $\omega(k)$ for waves in a warm magnetized plasma for a range of θ. For each θ we find the corresponding k and $\omega/\omega_{pe}(k)$ that gives the required n, and determine the polarization characteristics from the dispersion relation.

Fig. 2.6 displays the evolution of ω/ω_{pe} and kc/ω_{pe} for the Langmuir-z waves, calculated for a range of ψ. Waves are generated on the $\theta = 1°$ dispersion curve. As the waves propagate, θ increases and the waves remain on the Langmuir-z mode while kc/ω_{pe} and ω/ω_{pe} increase as indicated by the dashed lines. For a given θ, waves that propagate where ψ is greater have larger kc/ω_{pe}.

The polarization of the waves is quantified by $E_\perp^2/E^2$, the fraction of electric-field energy in the direction perpendicular to $\mathbf{k}$. The initial waves with $\omega \approx \omega_{pe}$ and $\theta = 1°$, corresponding to Beghin et al.'s spike-like emissions, have a negligible transverse electric field ($E_\perp^2/E^2 = 6.2 \times 10^{-10}$), which we interpret as the waves being on the Langmuir-like Section 2.of the Langmuir-z mode. Fig. 2.7
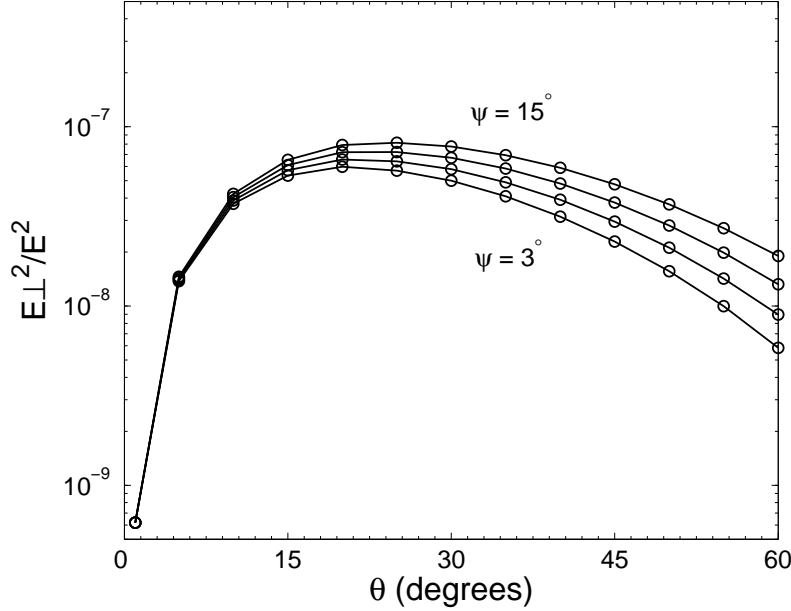
Figure 2.7: Plot of $E_\perp^2/E^2$ versus θ for the Langmuir-z mode for ψ between $3°$ and $15°$ in increments of $4°$.

shows how $E_\perp^2/E^2$ changes with θ for given ψ. We consider values of θ between $1°$ and $60°$, which is sufficient to demonstrate the general behavior. As θ increases $E_\perp^2/E^2$ increases and becomes at most $\sim 8.2 \times 10^{-8}$, which is achieved for $\psi = 15°$ and $\theta \approx 25°$. These waves then become more electrostatic for $\theta \gtrsim 25°$. We thus conclude that Beghin et al.'s wideband "z-mode" (actually Langmuir-z) waves remain predominantly electrostatic, in contrast to the assertion of *Beghin et al.* [1989].

We also perform the corresponding calculations for the Langmuir-whistler mode. These waves are also initially electrostatic ($E_\perp^2/E^2 = 6.2 \times 10^{-10}$), being generated on the part of the Langmuir-whistler mode that is closely Langmuir-like. The evolution of n and θ for the Langmuir-whistler waves is identical to that of the Langmuir-z waves, but here ω/ω_{pe} decreases as they move to lower kc/ω_{pe} so that the Langmuir-whistler dispersion relation is satisfied. Fig. 2.8 shows the polarization of the Langmuir-whistler waves as a function of θ. The maximum $E_\perp^2/E^2$ for these waves is $\sim 1.0 \times 10^{-6}$, which is attained when $\psi = 15°$ and $\theta = 85°$, the largest value of θ that we consider. Since $E_\perp^2/E^2$ remains very small during propagation, we predict that the wideband waves below ω_{pe} also remain electrostatic.
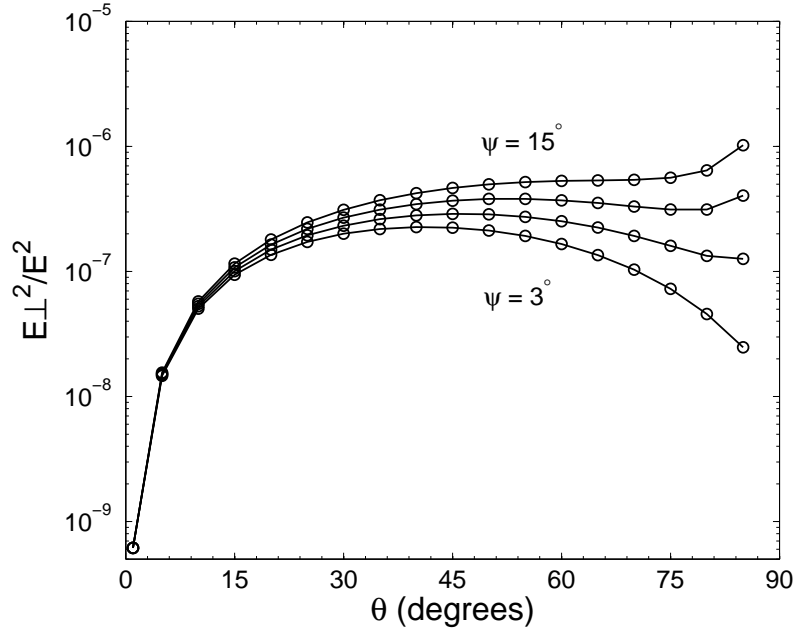
Figure 2.8: Same as Fig. 2.7, but for the Langmuir-whistler mode.

2.5 Auroral waves of McAdams et al., and McAdams and LaBelle

McAdams et al. [1999] presented observations from the PHAZE II rocket of high-frequency waves in the auroral ionosphere at altitudes of 390–945 km in underdense conditions. Termed "HF bands", these waves were monochromatic, long-lived, narrowband emissions with frequencies at and below the electron plasma frequency. They were postulated to be identical to the HF spike emissions reported by *Beghin et al.* [1989] in the underdense regions of the ionosphere but now observed using higher time resolution. Emissions just above the electron plasma frequency were also observed by the PHAZE II rocket, at altitudes below 420 km where the ionospheric plasma was overdense [*McAdams and LaBelle*, 1999].

2.5.1 Mode conversion

McAdams et al. [1999] proposed the following generation mechanism for HF bands:

(i) A positive slope in the electron distribution function (i.e., an electron

beam) drives Langmuir waves at ω_{pe};

(ii) Langmuir waves propagate into a region of higher plasma density (and thus higher local ω_{pe}), while their frequency remains constant;

(iii) as ω/ω_{pe} decreases, the wave moves from the Langmuir branch onto the whistler-mode branch and converts to a whistler-mode wave;

(iv) whistler-mode waves have a higher group speed and range of ω/ω_{pe} than Langmuir waves, and are detected as HF bands.

This mechanism was stated by *McAdams et al.* [1999] to be the same as that proposed by *Beghin et al.* [1989] for their spike emissions.

HF chirps were proposed by *McAdams and LaBelle* [1999] to be generated in a similar manner to HF bands. In this case the waves are generated as Langmuir waves, which then linearly convert into electromagnetic z-mode waves.

In the above mechanism for HF bands, it was stated that there is a connection between Langmuir and whistler modes for an underdense plasma. This is the basis for the conversion of Langmuir waves to whistler waves as they propagate into regions of higher plasma density. However, distinct Langmuir and whistler modes do not exist in an underdense kinetic magnetized plasma, but instead there exists a single Langmuir-whistler mode with the properties described in Sec. 2.2 [*Willes and Cairns*, 2000]. Our interpretation of the generation mechanism is thus that HF bands are generated by an electron beam instability near ω_{pe} on the Langmuir-whistler mode, where its properties are similar to those of the Langmuir mode. The wave then propagates on the Langmuir-whistler mode into regions where it has a lower value of ω/ω_{pe}, and the dispersion and polarization properties of the mode change smoothly to being more similar to the whistler mode in magnetoionic theory, without a conversion between distinct modes.

Similarly, distinct Langmuir and z modes do not exist in a magnetized kinetic plasma, and hence there cannot be a conversion between these modes to account for HF chirps. Instead the waves are generated on the Langmuir-like part of the generalized Langmuir-z mode, whose properties become more similar to the magnetoionic z mode as the wave propagates into regions with decreasing plasma density.
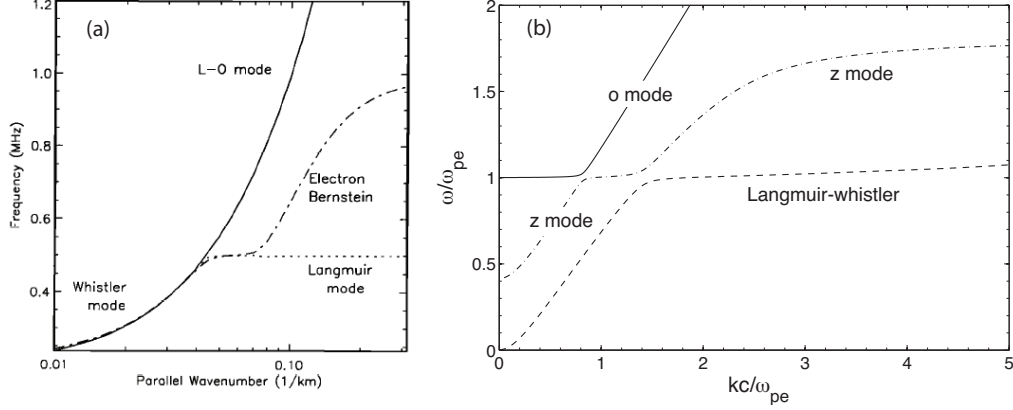
Figure 2.9: Comparison of (a) McAdams et al.'s calculations of wave dispersion using WHAMP for $f_{pe} = 0.5$ MHz and $f_{ce} = 1.0$ MHz (i.e., $\Omega_e/\omega_{pe} = 2.0$) and $k_\perp \ll k_\parallel$ (reproduced from Fig. 2.8 in *McAdams et al.* [1999]), and (b) our full numerical calculations of wave dispersion (EM magnetized kinetic theory) for $\Omega_e/\omega_{pe} = 2.0$ and $\theta = 5°$.

2.5.2 Dispersion relations

Dispersion relations were calculated by *McAdams et al.* [1999] using the WHAMP dispersion-solving code [*Rönnmark*, 1982] to show the connection between the Langmuir and whistler modes, and are reproduced in Fig. 2.9(a). Using our own dispersion-solving code, we here calculate dispersion relations for the same plasma parameters and model the plasma by Maxwellian distributions of background electrons and protons and a Maxwellian electron beam. These codes solve the same dispersion equation, but differ in the numerical methods used (for instance, in the calculation of the plasma dispersion function and Bessel functions).

The results of our calculations are shown in Fig. 2.9(b), from which we presently identify corrections to the dispersion curves of *McAdams et al.* [1999]. (Figure 2.9(b) with $\omega_{pe}/\Omega_e = 0.5$ has identical mode structure to that calculated by *André* [1985] for the case of $\omega_{pe}/\Omega_e = 0.64$ — see the $k_\parallel = 0$ face of his Fig. 2.2.)

(i) The "whistler mode" in Fig. 2.9(a) has a nonzero cutoff frequency, similar to *Beghin et al.* [1989]'s dispersion relations in Figs 2.2 and 2.3. Our numerical kinetic calculations show that the Langmuir-whistler mode actually has a lower frequency bound below $10^{-3}\omega_{pe}$, which agrees with semi-quantitatively with the magnetoionic prediction of zero for a single

ion population or no ions. A possible reason for this difference is that the WHAMP code jumps from the correct Langmuir-whistler mode to the z mode when these modes are nearby in (ω, k); i.e., near the second Ellis window. Comparisons between Figs 2.9(a) and 2.9(b) show this reason to be plausible, because the z-mode cutoff given by (2.3) in magnetoionic theory equals 207 kHz for these parameters, in excellent agreement with the observed cutoff. It is noted that WHAMP can properly calculate this situation if an adequate resolution is used, as seen in Fig. 2.2 of *André* [1985].

(ii) The "L-O mode" (synonymous with the o mode) in Fig. 2.9(a) extends below the cutoff frequency f_{pe} predicted from magnetoionic theory, at which it (wrongly) appears to have a dispersion relation very similar to the z mode. In contrast, the o mode in our numerical calculations (Fig. 2.9(b)) shows the expected cutoff at f_{pe}. Again, it is likely that as frequency decreases the WHAMP code has jumped from the o mode to the z mode, this time near the first Ellis window coupling point.

(iii) The "electron Bernstein" mode shown by the dash-dot line in Fig. 2.9(a) is actually the z mode, since Bernstein modes only exist with weak damping for nearly perpendicular propagation [*Bernstein*, 1958; *Robinson et al.*, 1988].

Despite these differences, there are a number of features which Figs 9(a) and 9(b) share:

(i) McAdams et al.'s dispersion relation for the electron Bernstein mode in Fig. 2.9(a) and our dispersion relation for the z mode in Fig. 2.9(b) are almost precisely the same at $kc/\omega_p \gtrsim 1.5$.

(ii) For frequencies above f_{pe}, their L-O mode and our o mode have very similar dispersion; this is also true for their Langmuir mode and our Langmuir-whistler mode.

Fig. 2.9(b) shows that for parallel propagation and $\omega_{pe}/\Omega_e = 0.5$, as appropriate for "band" emissions observed on PHAZE II [*McAdams et al.*, 1999], there is a limiting parallel electron beam speed of $0.7c$, corresponding to 43 keV, for which the beam can resonate with the Langmuir-whistler mode. Higher energies can only resonate with the z mode. From Fig. 2.1 of *Arnoldy et al.* [1999], the beam energies observed during the times of the "band" emissions

range from about 4–14 keV, well below this limiting energy. This supports the interpretation that the waves are excited by the beam on the Langmuir-whistler surface (the "Langmuir mode" in the parlance of *McAdams et al.* [1999]). As Fig. 2.9b) shows, the waves remain on this surface as they propagate into increasing electron density; there is no requirement for the mode conversion asserted by *McAdams et al.* [1999].

2.6   Conclusions

We investigated "mode conversion" phenomena proposed for auroral waves near ω_{pe} by *Beghin et al.* [1989], *McAdams and LaBelle* [1999], and *McAdams et al.* [1999], with the results summarized as follows.

(i) *Beghin et al.* [1989] observed waves above and below ω_{pe}, which they interpreted as electromagnetic z-mode and whistler-mode waves, respectively. However, their instability calculations showed that wave growth was confined to frequencies greater than the magnetoionic resonance frequencies for these wave modes. We argue that these waves must be understood in terms of the wave modes of magnetized kinetic plasmas, specifically the generalized Langmuir modes called the Langmuir-z and Langmuir-whistler modes [*Willes and Cairns*, 2000]. These generalized Langmuir modes possess the standard (thermal) Langmuir mode's characteristics at high k and either whistler-mode or z-mode characteristics at low k. Wave growth at frequencies greater than magnetoionic resonance frequencies is then easily explained as the waves being generated on the Langmuir-like part of the Langmuir-z or Langmuir-whistler mode. As these waves propagate in the inhomogeneous ionosphere, they remain on the Langmuir-z or Langmuir-whistler mode but move to lower k where the mode properties are different. No mode conversion process is necessary.

(ii) *Beghin et al.* [1989] also proposed that these waves undergo a change in wave character from electrostatic to electromagnetic during propagation. For a simplified model of the ionosphere we have shown that both their "whistler-mode" and "z-mode" (actually Langmuir-whistler and Langmuir-z) waves remain predominantly electrostatic.

(iii) *McAdams et al.* [1999] described HF bands at and below the plasma frequency, which were proposed to be generated through mode conversion from Langmuir waves into whistler waves. We instead propose that there is no conversion between distinct Langmuir and whistler modes, which do not exist as separate modes in a warm magnetized underdense plasma, but that the

HF bands are in a single mode, the generalized Langmuir-whistler mode, the properties of which change from being Langmuir-like to whistler-like as the wave propagates in the inhomogeneous plasma and moves to lower wave numbers. We put forward a similar interpretation for HF chirps [*McAdams and LaBelle*, 1999] propagating in the Langmuir-z mode.

We have shown that mode conversion is not required to account for observed waves near the electron plasma frequency, and can be replaced simply by propagation on the generalized Langmuir modes. However, mode conversion is undoubtedly necessary for processes that involve distinct modes, such as conversion between the Langmuir-z and o and x modes that can occur in radio windows [*Budden*, 1961; *Jones*, 1976a; *Kim et al.*, 2007].

Chapter 3

Electrostatic decay in a magnetized plasma

[Published as A. Layden *et al.*, *Phys. Rev. Lett. 110*, 18, 2013]

3.1 Abstract

The kinematics of the electrostatic (ES) decay of a Langmuir wave into a Langmuir wave and an ion sound wave are generalized to a weakly magnetized plasma. Unlike the unmagnetized case, ES decay in a magnetized plasma is always kinematically permitted and can produce daughter Langmuir waves with very small wave numbers, which we demonstrate by quasilinear simulations. The simulations further show that ES decay in magnetized plasmas is consistent with STEREO spacecraft observations of transversely polarized Langmuir waves in the solar wind.

3.2 Introduction

Electrostatic (ES) decay is a nonlinear three-wave process in which a primary Langmuir wave L decays into a product Langmuir wave L' of smaller wave number and an ion sound wave S [*Tsytovich*, 1970]. For Langmuir waves driven by electron beams [*Benford et al.*, 1980; *Melrose*, 1980b; *Cheung et al.*, 1982], one of the most fundamental systems in plasma physics, it is expected to be the dominant nonlinear process [*Cairns*, 2000]. The reduction in wave number of Langmuir waves via ES decay takes them out of resonance with the beam, and at sufficiently low wave numbers they can become localized in density wells, possibly triggering wave collapse [*Robinson et al.*, 1988] and dissipating energy

into the background plasma. ES decay is also crucial to generating radiation at multiples of the (angular) plasma frequency ω_p (plasma emission), one of four known coherent emission processes in space and astrophysical plasmas, vital for type II and III solar radio bursts [*Ginzburg and Zhelezniakov*, 1958; *Melrose*, 1980b] and the intense 2–3 kHz outer heliospheric emissions [*Kurth et al.*, 1984]. It provides S waves that stimulate production of electromagnetic waves near ω_p [*Ginzburg and Zhelezniakov*, 1958; *Melrose*, 1980b; *Cairns*, 1987b; *Robinson et al.*, 1993a], and counterpropagating L and L' waves that coalesce to give harmonic radiation near $2\omega_p$ [*Ginzburg and Zhelezniakov*, 1958; *Melrose*, 1980b; *Cairns*, 1987a; *Robinson et al.*, 1993a].

Previous analyses of ES decay assumed an unmagnetized plasma and calculated the kinematics in detail [*Melrose*, 1982; *Cairns*, 1987b,a]. However, magnetic fields are always present in space and astrophysical plasmas, and can significantly modify Langmuir dispersion [*Bale et al.*, 1998; *Willes and Cairns*, 2000], so ES decay in a magnetized plasma may have fundamentally different characteristics. Furthermore, it is not yet known under what conditions the unmagnetized approximation is valid. In this chapter, the first detailed kinematic calculations of ES decay in magnetized plasmas are presented and are compared with the unmagnetized results. First, quasilinear simulations of decay are performed using these new kinematics. We then show that these results can explain semi-quantitatively some recent STEREO spacecraft observations of transversely polarized Langmuir waves in the solar wind [*Malaspina et al.*, 2011].

3.3   Derivation of kinematics

The kinematics of ES decay can be derived using a semiclassical formalism [*Tsytovich*, 1970], where Langmuir and ion sound wave fields are quantized. Imposing conservation of energy ($\hbar\omega$) and momentum ($\hbar\mathbf{k}$) for the decay gives the wave-matching conditions $\omega_L = \omega_{L'} + \omega_S$ and $\mathbf{k}_L = \mathbf{k}_{L'} + \mathbf{k}_S$, which imply

$$\omega_{L'}(\mathbf{k}_{L'}) = \omega_L(\mathbf{k}_L) - \omega_S(\mathbf{k}_L - \mathbf{k}_{L'}). \tag{3.1}$$

In an unmagnetized plasma, the Langmuir ($l = L$ or L') and ion-sound dispersion relations are

$$\omega_l(k_l) = \omega_p + 3k_l^2 V_e^2/2\omega_p, \tag{3.2}$$

$$\omega_S(k_S) = k_S v_S, \tag{3.3}$$

respectively, where $k = |\mathbf{k}|$, V_e is the electron thermal speed, $v_S = V_e\sqrt{\gamma m_e/m_i}$ is the ion sound speed, and $\gamma = 1+3T_i/T_e$ with T_i/T_e the ratio of ion to electron temperatures. Unmagnetized kinematics are derived by substituting (3.2) and (3.3) into (3.1) and solving for $\mathbf{k}_{L'}$ in terms of $\mathbf{k}_L$.

Here, we consider a fully ionized electron-proton plasma, which gives $m_i/m_e = 1836$, and set $\gamma = 2$. Also, we restrict our analysis to the case where $\theta_{LL'}$, the angle between $\mathbf{k}_L$ and $\mathbf{k}_{L'}$, is 0 (forward-scatter) or π (backscatter), since this is where the ES decay rate is maximal [*Robinson et al.*, 1993a]. Forward- and backscatter will be represented by positive and negative $k_{L'}$, respectively. Solutions to (3.1) are amenable to graphical interpretation; setting $\mathbf{k}_L$ constant, solutions for $\mathbf{k}_{L'}$ occur where the left-hand side (LHS) and right-hand side (RHS) of (3.1) intersect. Figure 3.1(a) shows this graphical construction for the unmagnetized case, where points on the solid curve (RHS) that are intersected by a dashed curve (LHS) are solutions for k_L and $k_{L'}$. As k_L decreases past $k_0 = 2\omega_p v_S/3V_e^2$ (point A) the decay swaps from backscatter to forward-scatter, and stops altogether at $k_L = k_0/2$ (point B) where the LHS and RHS are tangential and the only solution is $k_L = k_{L'}$. These results can also be represented by plotting $k_{L'}$ versus k_L [Fig. 3.1(b)]. Backscatter has $k_{L'} = k_L - k_0$ for $k_L > k_0$ and forward-scatter has $k_{L'} = k_0 - k_{L'}$ for $k_0/2 < k_L < k_0$. The minimum $k_{L'}$ is 0 (at $k_L = k_0$), which corrects the assertion by previous authors [*Tsytovich*, 1970; *Cairns*, 1987a] that it is $k_0/2$.

For the first time we now include magnetization of the plasma in ES decay kinematics by using the dispersion relations of magnetized wave modes when solving (3.1). The magnetized counterpart of the Langmuir mode in a weakly magnetized plasma (i.e., $\omega_p > \Omega_e$, where Ω_e is the electron gyrofrequency) is the Langmuir-z mode [*Willes and Cairns*, 2000; *Layden et al.*, 2011], which has Langmuir-like dispersion at high k but z-mode-like dispersion at low k. Dispersion for this mode is a function of the angle θ_B between $\mathbf{k}$ and the ambient magnetic field $\mathbf{B}$, and plasma's magnetization, which we quantify by $\omega_p/\Omega_e \propto |\mathbf{B}|^{-1}$. As there is no simple, accurate, analytic approximation for the Langmuir-z mode, we calculate the dispersion relation numerically from the 3D homogeneous, magnetized, kinetic dispersion equation (e.g. [*Melrose*, 1980a]), with typical examples shown in Fig. 3.2. The unmagnetized Langmuir dispersion relation $\omega(k)$ is a convex function, with smaller $\partial\omega/\partial k$ for smaller k. In contrast, the Langmuir-z mode has much larger $\partial\omega/\partial k$ where the magnetized and unmagnetized dispersion relations diverge from each other; for $\theta_B \approx 0$ this occurs at

$$k_*\lambda_D = (V_e/c)(1 + \omega_p/\Omega_e)^{-1/2}, \tag{3.4}$$
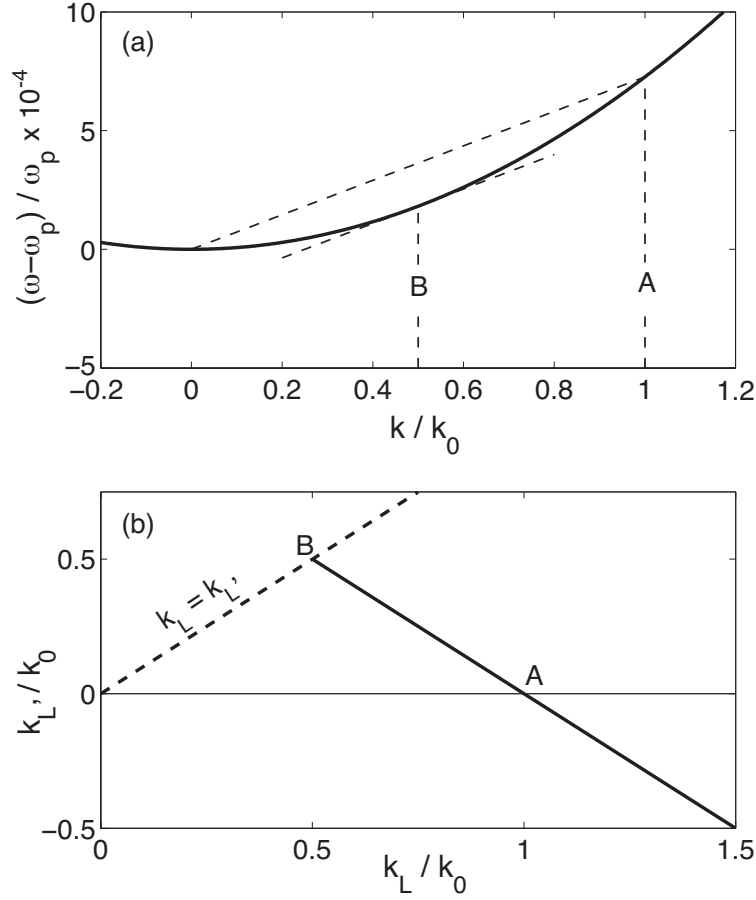
Figure 3.1: (a) LHS (solid line) and RHS (dashed line) of (3.1) as functions of $k_{L'}$ for an unmagnetized plasma, for (A) $k_L = k_0$, and (B) $k_L = k_0/2$. (b) $k_{L'}$ versus k_L for the same situation, where the solid line represents solutions for the decay.

which proves to be an important parameter. This is also the characteristic wave number of the radio window for linear mode conversion between the Langmuir-z and o modes at density gradients [*Ellis*, 1956; *Budden*, 1961; *Yoon et al.*, 1998]. Numerical solution of the dispersion equation shows that magnetization has a negligible effect on ion sound dispersion, so we keep the unmagnetized relation (3.3). Henceforth we will assume $\theta_B = 0$ in our calculations; this is a good approximation, since electron beams streaming along magnetic field lines drive Langmuir waves centered about $\theta_B = 0$.

We first present a representative magnetized case: $\omega_p/\Omega_e = 2$. Figure 3.3(a), analogous to Fig. 3.1(a), shows solutions for various k_L. At point α,
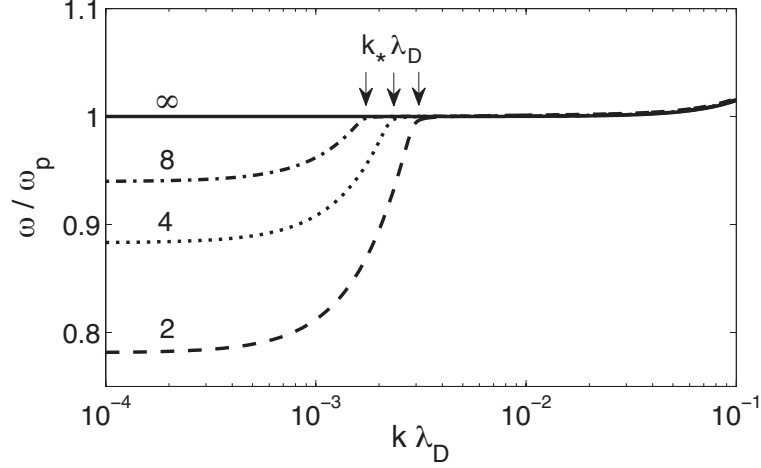
44

Figure 3.2: Langmuir-z dispersion relations for $V_e/c = 5 \times 10^{-3}$, $\theta_B = 0$, and $\omega_p/\Omega_e = 2, 4, 8, \infty$.

where $k_L > k_0 + k_*$, thermal effects dominate over magnetic effects and the magnetized and unmagnetized results coincide. However, fundamental changes in decay properties are seen for $k_L < k_0 + k_*$. At A, $k_L = k_0$, and the decay is a backscatter to $k_{L'} \approx -k_*$ rather than $k_{L'} = 0$, due to the lower frequency of the Langmuir-z mode compared to the unmagnetized Langmuir mode. ES decay remains purely a backscatter process until $k_L = k_0 - k_*$ at β, where there is an extra forward-scatter solution that does not appear in the unmagnetized approximation. As k decreases further between β and B (where $k_L = k_0/2$), there are two forward-scatter solutions (one near $k_L = k_*$) and one backscatter solution (near $k_L = -k_*$). Between B and δ where $k_L = k_*$, there are no solutions for an unmagnetized plasma, but the magnetized case has one backscatter and one forward-scatter solution. At lower k than δ there is one backscatter solution.

We now focus on the wave numbers of these decays, shown in Fig. 3.3(b). Compared to the unmagnetized results in Fig. 3.1(b), magnetization splits solutions into two branches with opposite signs of $k_{L'}$. For $k_* \lesssim k_L \lesssim k_0 - k_*$, the lower portion of the positive-$k_{L'}$ (forward-scatter) branch has $k_{L'} \approx k_*$, so all forward-scatters in this k_L range give $k_{L'} \approx k_*$. Similarly, the negative-$k_{L'}$ (backscatter) branch has $k_{L'} \approx -k_*$ for $k_* \lesssim k_L \lesssim k_0 + k_*$. For $k_L \lesssim k_*$, backscatter changes only the sign of the wave number ($k_{L'} \approx -k_L \approx -k_*$), corresponding to a reversal of its propagation.

Taking the limit $\omega_p/\Omega_e \to \infty$ (so that $k_* \to 0$), the backscatter and forward-scatter solutions merge at $k_L = k_0$ and the unmagnetized results are recovered.
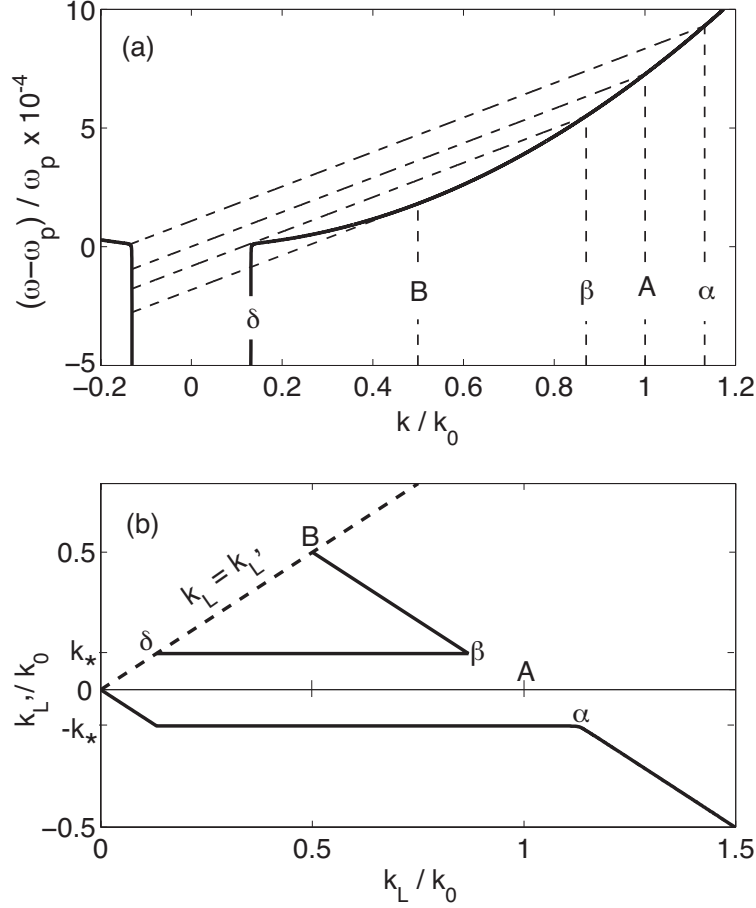
Figure 3.3: Analog of Fig. 3.1 for the magnetized case with $\omega_p/\Omega_e = 2$ and $\theta_B = 0$. At points α, β, and δ, $k_L = k_0 + k_*$, $k_0 - k_*$, and k_*, respectively.

However, surprisingly, the extra solutions that appear in our magnetized calculations exist even for very large ω_p/Ω_e. These solutions, which have not been recognized previously, have wide-reaching applications, some of which are discussed below.

3.4   Applications

The STEREO spacecraft recently observed Langmuir-like waves with large transverse polarization in association with type III solar radio bursts [*Malaspina et al.*, 2011], where the transverse component of electric field is $E_\perp = |\mathbf{E} \times \mathbf{B}|/|\mathbf{B}|$. Values of $F = E_\perp^2/E^2$ of 0 to 0.8 were found, with larger values correlated with higher v_b, the speed of the electron beam that drives the Langmuir
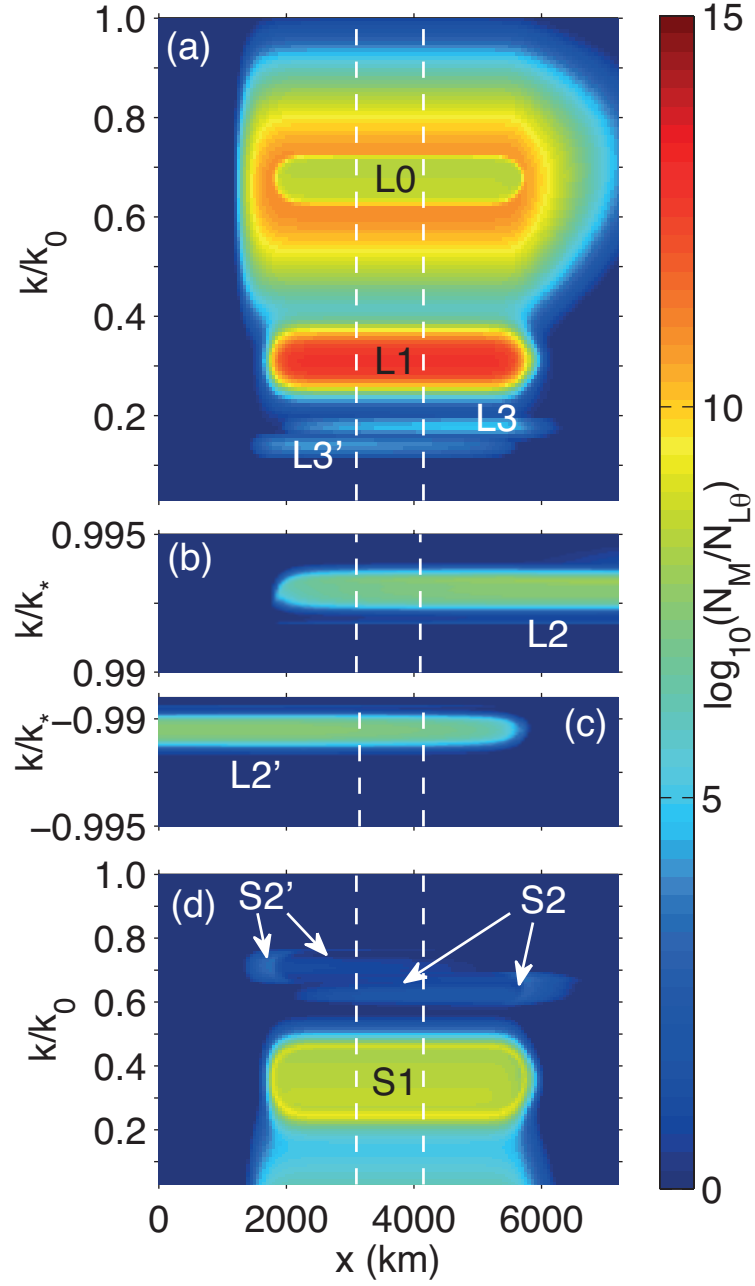
Figure 3.4: (a)-(c) $N_L(x, k)/N_{L\theta}$ and (d) $N_S(x, k)/N_{L\theta}$ at $t = 15$ s without reflecting boundaries. White dashed lines represent where reflecting boundaries are situated in the subsequent simulation, to aid comparison.
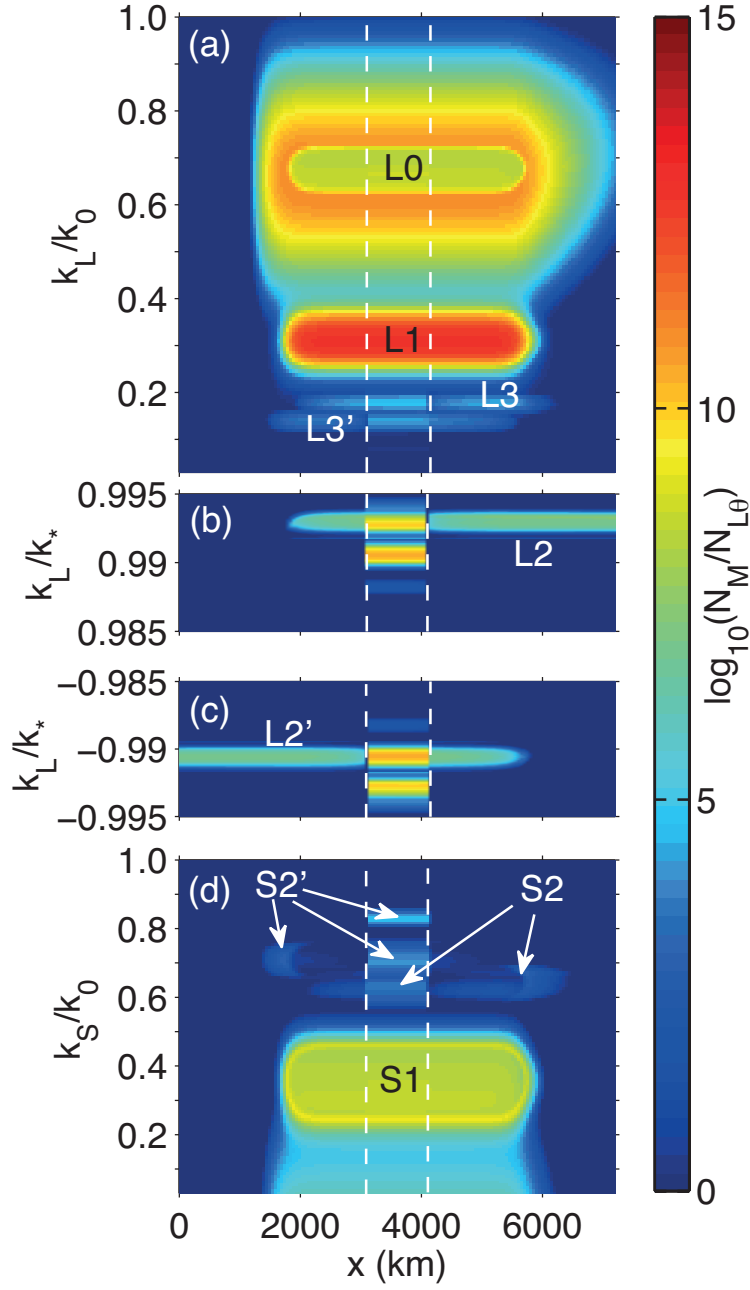
Figure 3.5: (a)-(c) $N_L(x,k)/N_{L\theta}$ and (d) $N_S(x,k)/N_{L\theta}$ at $t = 15$ s, where white dashed lines represent reflecting boundaries for Langmuir waves with $|k_L| < k_*$.

waves. Large F was also often accompanied by a double-peak feature in the frequency spectrum. These waves were interpreted as a beam-driven Langmuir-z component with wave number $k_b \approx \omega_p/v_b$ and small to moderate $E_\perp$, and a separate Langmuir-z component at low k (actually near k_*) where $E_\perp$ becomes large [*Willes and Cairns*, 2000]. The origin of these low-k Langmuir-z waves is an open question, and we here propose a generation mechanism based on ES decay.

To simulate ES decay in the magnetized solar wind, we use a 1D simulation code [*Li et al.*, 2008] with quasilinear electron-Langmuir wave physics and nonlinear electrostatic decay, but with the decay kinematics modified as above. Waves are treated semiclassically, i.e., as a collection of wave quanta with occupation number $N_M(x,k) = W_M(x,k)/\hbar\omega_M(x,k)$, where W_M is the energy density in the wave mode M. Parameters chosen are [*Malaspina et al.*, 2011]: $\omega_p = 2\pi \times 20000$ s^{-1}, $\omega_p/\Omega_e = 50$, $V_e/c = 5 \times 10^{-3}$, and $T_i/T_e = 1/3$ (i.e. $\gamma = 2$), giving $k_* = 3.2 \times 10^{-2}k_0$. We assume a source term of initial Langmuir waves

$$\frac{\partial N_L}{\partial t} = S_0 \exp\left[- \left(\frac{t - t_c}{\Delta t}\right)^2 - \left(\frac{x - x_c}{\Delta x}\right)^{16} - \left(\frac{k - k_c}{\Delta k}\right)^2\right], \qquad (3.5)$$

where $S_0 = 2E_{\max}^2/\epsilon_0\hbar\omega_p\Delta t\Delta k$. As $t \to \infty$ the source has $E = E_{\max}$ at $x = x_c$, in the absence of any other sources of growth or damping. Here we choose $t_c = 20$ s, $\Delta t = 5$ s, $x_c = 3600$ km, $\Delta x = 4000$ km, $k_c = 0.68k_0$, $\Delta k = 0.1k_c$, and $E_{\max} = 100$ mV/m. This k_c corresponds to a point between B and β in Fig. 3.3(a). We also simulate with and without a background plasma density well, with boundaries at $x = 3600 \pm 500$ km, that reflects Langmuir waves with $|k_L| < k_*$.

Figure 3.4 displays $N_L(x,k)/N_{L\theta}$ and $N_S(x,k)/N_{L\theta}$ at $t = 15$ s without reflecting boundaries, where $N_{L\theta} = k_B T_e/4\pi\hbar\omega_p\lambda_D^2$ is the thermal level of L waves at $k_L = 0$ [*Li et al.*, 2002]. The features of the spectra are produced by the following processes. (i) Decay from $L0$ ($k_L = k_c$) to $L1$ ($k_{L'} = k_0 - k_c = 0.32k_0$), producing $S1$ ($k_S = 2k_c - k_0 = 0.36k_0$). We note that $L0$ is "hollowed out" because the Langmuir waves decay exponentially with a rate proportional to the initial N_L, which is larger at the center of L_0. (ii) Decay from $L1$ to $L2$ ($k_{L'} = k_*$) and $L2'$ ($k_{L'} = -k_*$), stimulated by $S1$ waves. (iii) Decay from $L0$ to $L2$ and $L2'$, producing $S2$ and $S2'$, respectively. (iv) Decay from $L0$ to $L3$ and $L3'$, stimulated by $S2$ and $S2'$, respectively.

Figure 3.5 shows the corresponding results for the reflecting case, with the reflecting boundaries represented by white dashed lines. The processes are the same as described above. However, $L2$ and $L2'$ have larger N_L because these
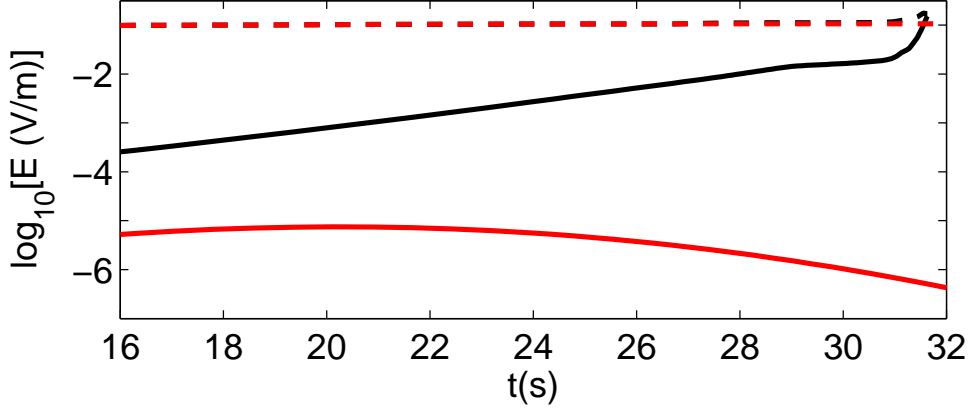
49

Figure 3.6: Time series of $E_{||}$ (dashed line) and $E_{\perp}$ (solid line) at $x = 3600$ km, with reflection of low-k Langmuir-z waves (black) and without reflection (red).

low-k waves, which have large group velocities, now cannot propagate away from the source region. Also, larger $L2$ and $L2'$ give increased $S2$ and $S2'$. Increasing Δx produces similar effects, since L and S waves remain longer in the source region.

Integrating $N_L(x, k)$ over k we obtain the time-varying total electric fields of Langmuir waves with $k \leq k_*$ ($E_{\perp}$) and $k > k_*$ ($E_{||}$), shown in Fig. 3.6. When there is no region of Langmuir-z wave trapping due to a density well, $E_{\perp}$ does not grow to very large levels at $x = 3600$ km, and then falls off as the Langmuir-z waves near k_* propagate away. However, when the density well is present we see an approximately exponential increase in $E_{\perp}$, and near $t = 30$ s $E_{\perp} \approx 40$ mV/m at k_*, giving $F \approx 0.5$. This is sufficient to account for some STEREO spacecraft polarization observations [*Malaspina et al.*, 2011].

Another application is to localized Langmuir wave packets in the solar wind, termed intense localized structures (ILS), that are trapped in density cavities of length $10^3 \lambda_D$ [*Nulsen et al.*, 2007; *Ergun et al.*, 2008]. These density perturbations can be caused by ion sound waves with wavelength λ_S similar to the length scale of the cavity. From our results, after Langmuir waves undergo an ES decay cascade to $k_L = k_*$ they will backscatter to $k_{L'} = -k_*$ and generate ion sound waves with $k_S = \pm 2k_*$. Since the rate of ES decay increases as k_L decreases [*Robinson et al.*, 1993a], we predict multiple backscatters and so a strong population of such ion sound waves. These waves have $\lambda_S = 2\pi/2k_* \approx 5 \times 10^3 \lambda_D$, which is comparable to the sizes of the density cavities observed. We suggest

that some, perhaps most, ILS develop in density depressions produced by the evolution of S waves with $|k_S| \approx 2k_*$ formed by ES decay. This is an unexpected coupling between ES decay and ILS events which is present only with $B \neq 0$.

3.5 Conclusion

We have generalized the kinematics of ES decay to magnetized plasmas and found fundamental differences for $k_L \lesssim k_0 + k_*$, the most significant of which is the existence of solutions with very low $k_{L'} \approx k_*$ and large $E_\perp/E$. These solutions should be essential for modeling phenomena involving low-k Langmuir waves from ES decay, such as wave collapse and transverse Langmuir polarization. Future work may involve implementing these kinematics in numerical simulations of solar radio bursts [*Li et al.*, 2008], or in simulations of strong Langmuir turbulence in a magnetized plasma [*Graham et al.*, 2011].

Chapter 4

Kinematics of decay in magnetized plasmas

4.1 Abstract

The kinematics for electrostatic decay of Langmuir-like waves in weakly and strongly magnetized plasmas in two dimensions are derived. Low-wave number solutions for the decay that were found to exist in 1D for a weakly magnetized plasma are also obtained in 2D, where the primary Langmuir wave can have an arbitrary direction with respect to the background magnetic field. Kinematics are also calculated for a strongly magnetized plasma where the appropriate wave modes are the Langmuir-whistler mode and an ion-sound/ion-cyclotron mode.

4.2 Introduction

Electrostatic (ES) decay is a nonlinear three-wave process in which a primary Langmuir wave L decays into a product Langmuir wave L' of smaller wave number and an ion sound wave S [*Tsytovich*, 1970]. ES decay is crucial to generating radiation via plasma emission at multiples of the (angular) plasma frequency ω_p vital for type II and III solar radio bursts [*Ginzburg and Zhelezniakov*, 1958; *Melrose*, 1980b] and the intense 2–3 kHz outer heliospheric emissions [*Kurth et al.*, 1984]. It provides S waves that stimulate production of electromagnetic waves near ω_p [*Ginzburg and Zhelezniakov*, 1958; *Melrose*, 1980b; *Cairns*, 1987b; *Robinson et al.*, 1993a], and counterpropagating L and L' waves that coalesce to give harmonic radiation near $2\omega_p$ [*Ginzburg and Zhelezniakov*, 1958; *Melrose*, 1980b; *Cairns*, 1987a; *Robinson et al.*, 1993a].

Previous analyses of ES decay assumed an unmagnetized plasma, but recent results (Chapter 3 and *Layden et al.* [2013]) have shown magnetization effects to modify the decay significantly when considering a weakly magnetized ($\omega_p > \Omega_e$) plasma with waves parallel to the ambient magnetic field; i.e., $\mathbf{k}_L || \mathbf{B}_0$ and $\mathbf{k}_{L'} || \mathbf{B}_0$. In this chapter, we investigate more thoroughly the decay kinematics that result when these assumptions are relaxed.

The structure of the chapter is as follows: Section 4.3 outlines the background theory of wave modes in unmagnetized, weakly magnetized, and strongly magnetized plasmas. Section 4.4 describes the process for calculating kinematics of three-wave decay. Section 4.5 reviews the kinematics for an unmagnetized plasma in both 1D and 2D. Section 4.6 outlines the 1D results derived in Chapter 3 and *Layden et al.* [2013] for a weakly magnetized plasma and then provides the first 2D results where primary and product wave vectors have arbitrary directions with respect to each other and $\mathbf{B}_0$. Section 4.7 presents the corresponding results for a strongly magnetized plasma, where magnetization effects become important for the low frequency mode. We then discuss the applications of the previous sections in Sec. 4.8 and conclusions in Sec. 4.9.

4.3   Wave modes in warm magnetized plasmas

In a warm, unmagnetized plasma, the dispersion relations for the Langmuir and ion sound waves (in the limit $k\lambda_D \ll 1$) are

$$\omega_L(k_L) = \omega_p + 3k_L^2 V_e^2/2\omega_p, \tag{4.1}$$

$$\omega_S(k_S) = k_S v_S, \tag{4.2}$$

respectively, where $k = |\mathbf{k}|$, V_e is the electron thermal speed, $v_S = V_e\sqrt{\gamma m_e/m_i}$ is the ion sound speed, $\gamma = 1 + 3T_i/T_e$, and T_i/T_e is the ratio of ion to electron temperatures.

It is known that magnetic fields affect the dispersion of Langmuir waves as k becomes small; in a weakly magnetized plasma ($\omega_p > \Omega_e$), the Langmuir mode becomes z-mode-like at low k, whereas for a strongly magnetized plasma ($\omega_p < \Omega_e$) the dispersion approaches that of the whistler mode [*Willes and Cairns*, 2000]. For both weakly and strongly magnetized plasmas, when $\mathbf{k}$ is perpendicular or highly oblique to $\mathbf{B_0}$ there is an "upper-hybrid" plateau with $\omega \approx \omega_{uh} + 3k^2 V_e^2/2\omega_p$ for large k, where $\omega_{uh} \approx \sqrt{\omega_p^2 + \Omega_e^2}$.

For a weakly magnetized plasma, the unmagnetized approximation (4.2) to the ion sound mode is valid. For a more strongly magnetized plasma, both

the ion sound mode and the ion cyclotron mode are relevant to decay, as well as the whistler/lower-hybrid mode. The unmagnetized approximation to the ion acoustic mode is valid in this case only for $\omega_S(k) \gg \Omega_i$, or when $\theta_B = 0$ [*Melrose*, 1986a; *Hellberg and Mace*, 2002]; this will be discussed in detail in later sections.

4.4 Method

In the following, we use a semiclassical formalism in which the wave fields in a mode M are considered to be composed of a collection of wave quanta, each with energy $\hbar\omega_M$ and momentum $\hbar\mathbf{k}_M$. Conservation of energy and momentum for the process $L \to L' + S$ requires that

$$\mathbf{k}_{L'} = \mathbf{k}_L - \mathbf{k}_S, \tag{4.3}$$

$$\omega_{L'} = \omega_L - \omega_S, \tag{4.4}$$

which can be combined to give

$$\omega_{L'}(\mathbf{k}_{L'}) = \omega_L(\mathbf{k}_L) - \omega_S(\mathbf{k}_L - \mathbf{k}_{L'}), \tag{4.5}$$

Dispersion relations $\omega_M(\mathbf{k})$ are calculated numerically using a code that solves the dispersion equation for waves in a thermal magnetized plasma, as described in *Willes and Cairns* [2000] and Chapters 3 and 4. For each $\mathbf{k}_L$, we impose the wave-matching condition (4.5) to find the kinematically allowed values of $\mathbf{k}_{L'}$.

4.5 Kinematics in unmagnetized plasmas

The kinematics of ES decay, which are well known [*Melrose*, 1982; *Cairns*, 1987b,a], are summarized here. Ion sound parameters may be eliminated by substituting (4.1) into (4.4) to give

$$\omega_S(\mathbf{k}_S) = |\mathbf{k}_L - \mathbf{k}_{L'}|v_S. \tag{4.6}$$

Defining the quantity $\theta_{LL'} = \cos^{-1}(\mathbf{k}_L \cdot \mathbf{k}_{L'})$, (4.6) can be rewritten as

$$\omega_S(\mathbf{k}_S) = (k_L^2 + k_{L'}^2 - 2k_L k_{L'} \cos\theta_{LL'})v_S. \tag{4.7}$$

Substituting (4.7) and (4.1) into (4.4) and defining $k_0 = 2\omega_p v_s/3V_e^2$ and $K_M = k_M/k_0$ yields

$$\cos\theta_{LL'} = \frac{K_L^2 + K_{L'}^2 - (K_L^2 - K_{L'}^2)^2}{2K_L K_{L'}}. \tag{4.8}$$

4.5.1 Decay in 1D

From here we first address the special case where primary and product Langmuir wave vectors are parallel or antiparallel. To obtain the kinematics for 1D we substitute $\theta_{LL'} = 0, \pi$ into (4.8). After simplification this reduces to $k_{L'} = k_0 - k_L$ for $k_L \geq k_0/2$ and has no solution for $k_L < k_0/2$, as discussed in Sec. 3.3.

4.5.2 Decay in 2D

We now address the general case where primary and product Langmuir wave vectors have arbitrary relative positions. Returning to the quartic equation (4.8), it is convenient to introduce the variables $\Delta = K_L - K_{L'}$ and $\Theta = \sin^2(\theta_{LL'}/2)$. The allowed ranges of these variables are $0 \leq \Delta \leq K_L$ and $0 \leq \Theta \leq 1$, where $\Theta = 0$ and $\Theta = 1$ correspond to forward-scatter and backscatter, respectively. Substitution of Δ and Θ into (4.8) yields

$$\Theta(\Delta) = \frac{\Delta^2 (\Delta - 2K_L + 1)(\Delta - 2K_L - 1)}{2K_L(K_L - \Delta)}. \tag{4.9}$$

Stationary points of (4.9), which will be useful in the following analysis, are found by differentiating (4.9) with respect to Δ, giving

$$\Theta'(\Delta) = -\frac{\Delta(\Delta - 2K_L)(\Delta + \sqrt{(1 - K_L^2)/3} - K_L)(\Delta - \sqrt{(1 - K_L^2)/3} - K_L)}{4K_L(K_L - \Delta)^2} \tag{4.10}$$

and calculating its roots, which are $\Delta = 0$, $2K_L$, and $K_L \pm \sqrt{(1 - K_L^2)/3}$. Of these, only $\Delta = K_L - \sqrt{(1 - K_L^2)/3}$ satisfies $0 < \Delta < K_L$, and then only for $1/2 \leq K_L \leq 1$.

A trivial solution $\Theta(0) = 0$ exists for all K_L, corresponding to $\mathbf{k}_L = \mathbf{k}_{L'}$ and $\mathbf{k}_S = 0$. For the remaining solutions, there exist four regimes which must be considered separately: (i) $K_L > 1$, (ii) $K_L = 1$, (iii) $1/2 \leq K_L < 1$, and (iv) $K_L < 1/2$. Figure 4.1 displays $\Theta(\Delta)$ for K_L that lies in each of these regions.

In region (i), the only root is the trivial root $\Theta(0) = 0$, so there is exactly one forward-scatter solution. There is also exactly one backscatter solution, $\Theta(1) = 1$. Since Θ has no turning points in the allowed domain of Δ and has an asymptote at $\Delta = K_L$, we see that $\Theta > 1$ for $\Delta > 1$, so that there are no solutions for $\Delta > 1$. We also note that in there is a one-to-one correspondence between Δ and Θ in their allowed regions.

Region (ii) also has solutions for all $0 \leq \Delta \leq 1$, but with some important differences. Firstly, Θ has a maximum of $1/2$ rather than 1; i.e., $|\theta_{LL'}| < \pi/2$.
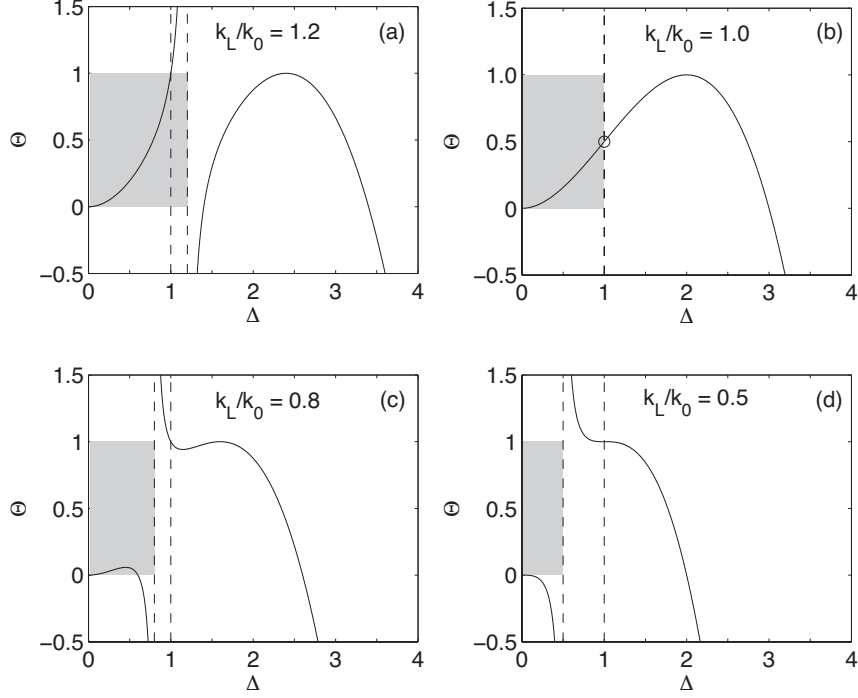
Figure 4.1: Plots of $\Theta(\Delta)$ as defined in (4.9) for the labeled values of k_L/k_0. Dashed lines represent the denominator of (4.9) and $\Delta = k_L/k_0$, and the gray shaded area represents the permissible range of solutions for Δ. At the circle in panel (c) Θ is undefined.
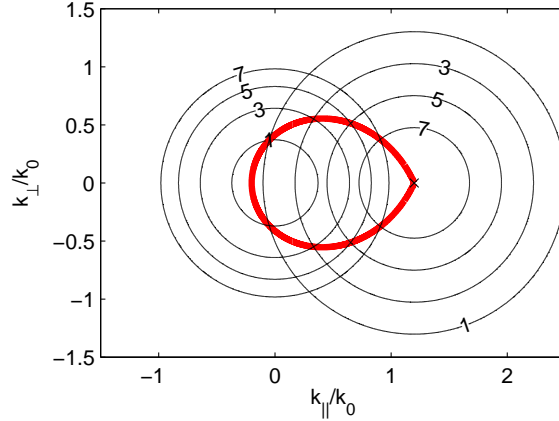

Figure 4.2: Graphical construction for 2D unmagnetized decay kinematics, with primary wave vector $k_L/k_0 = 1.2$ indicated by a cross. Contours centered at $k = 0$ and $k = 1.2k_0$ correspond to the LHS and RHS of (4.5), i.e., $\omega_{L'}$ and $\omega_L - \omega_S$, respectively. These frequencies are scaled as $(\omega/\omega_p - 1) \times 10^4$. The red line corresponds to $k_{L'}$ solutions, where equal contours intersect.

Secondly, Θ is undefined at $\Delta = 1$ as can be seen from the denominator of (4.9), corresponding to $\theta_{LL'}$ being undefined at $K_{L'} = 0$.

In region (iii), there now exists both a second root (forward-scatter solution) at $\Delta = 2K_L - 1$ and a turning point at $\Delta = K_L - \sqrt{(1 - K_L^2)/3}$. For each Θ there exist two solutions for Δ, except at the turning point where the maximum Θ is obtained.

Region (iv) has $\Theta < 0$ for all Δ in the allowed range, so there are no solutions and decay cannot proceed.

In addition to the analytic approach above, the 2D case is also amenable to graphical interpretation. Figure 4.2 shows the graphical construction for $k_L = 1.2k_0$, where the LHS and RHS of (4.5) are shown as contour plots in $(k_\parallel, k_\perp)$ space. The intersection of these contours, indicated by a red line, gives the solutions for $\mathbf{k}_{L'}$. This figure comports with the ranges of Δ and Θ in Fig. 4.1, namely $\theta_{LL'}$ from 0 to 2π and Δ from 0 to 1.

4.6 Kinematics in weakly magnetized plasmas

In a weakly magnetized plasma and for propagation nearly (but not exactly) parallel to the ambient magnetic field, the counterpart of the unmagnetized Langmuir mode is the Langmuir-z mode, with Langmuir-like dispersion at high k and z-mode-like dispersion at low-k [*Willes and Cairns*, 2000]. For propagation perpendicular to the magnetic field, the relevant mode is an upper-hybrid-like mode.

4.6.1 Decay in 1D, wave vectors perpendicular to $\mathbf{B}_0$

Here, we describe the kinematics for decay of an upper hybrid wave to another upper hybrid wave and an ion sound wave. Upper hybrid waves have wave vectors perpendicular to the background magnetic field; i.e., $\theta_B = \pi/2$. For large k, upper hybrid waves have the approximate dispersion relation $\omega_{UH}^2(k) = \omega_{uh}^2 + 3k^2 V_e^2$ [*Melrose*, 1986a], where $\omega_{uh} = (\omega_p^2 + \Omega_e^2)^{1/2}$. Since $\omega_{UH}(k)$ differs from $\omega_L(k)$ only by an additive constant ($\omega_{uh} - \omega_p \approx \Omega_e^2/2\omega_p$), the kinematics for large k are essentially the same as those for an unmagnetized plasma.

Like the decay of the Langmuir-z mode, numerically calculated dispersion relations of the upper-hybrid mode are needed for the calculation of kinematics. Typical upper-hybrid dispersion relations are shown in Figure 4.3, for $V_e/c = 5 \times 10^{-3}$ and a range of ω_p/Ω_e. At $\omega = \omega_p$ these waves have $k\lambda_D = V_e/c$; this

wave number is greater than that of the Langmuir-z mode, viz.,

$$k_* \lambda_D = (V_e/c)(1 + \omega_p/\Omega_e)^{-1/2}. \tag{4.11}$$

As k increases the frequency increases steadily until it plateaus at ω_{uh}.

A notable feature of upper-hybrid decay is that there do not always exist solutions $\mathbf{k}_{L'}$ that are parallel to $\mathbf{k}_L$ (as opposed to antiparallel), in contrast to the $k_{L'} = k_*$ solution branch for the Langmuir-z mode. The condition for parallel solutions is that $v_S > v_g$ at some k, which can be understood as follows. Figure 4.4 shows v_g for the Langmuir/upper-hybrid mode and the S mode for $\omega_p/\Omega_e = 50$ and $V_e/c = 5 \times 10^{-3}$. For $\gamma = 1 + 3T_i/T_e = 2$, $v_S < v_g$ for all k, whereas $\gamma = 4$ has $v_S > v_g$ for a range of k. Looking at the graphical construction for wave-matching shown in Fig. 4.5, we see that $\gamma = 2$ has no intersection with the solid line (L dispersion relation) whereas $\gamma = 4$ does due to its larger v_S. The transition between these two cases is when $v_S = v_g$ at only one k.

Figure 4.6 plots T_i/T_e for which $v_S = v_g$ at a single k, given ω_p/Ω_e and V_e/c; e.g., for $\omega_p/\Omega_e = 50$ and $V_e/c = 5 \times 10^{-3}$, this minimum is $T_i/T_e \approx 0.8$. If the minimum does not appear on the graph (since it is negative), parallel decay is permitted for all T_i/T_e. With this condition stated, we now calculate the decay kinematics for $\omega_p/\Omega_e = 50$ and $V_e/c = 5 \times 10^{-3}$ in the same manner as for the 1D parallel case in Sec. 3.3. Figure 4.7 shows $k_{L'}$ as a function of k_L for a range of $\gamma = (1 + 3T_i/T_e)^{1/2}$. For $\gamma = 2$ there are no parallel $k_{L'}$ (forward scatter) solutions since T_i/T_e is below the minimum required in Fig. 4.6. Comparing Fig. 3.3 and Fig. 4.7 shows that the antiparallel $k_{L'}$ solutions closely resemble those for the Langmuir-z mode, with $k_{L'} \approx k_0 - k_L$ for large k and $k_{L'} \approx -k_*$ when $k_* \lesssim k_L \lesssim k_0 + k_*$. For $\gamma \geq 3$ there are now up to two parallel-$k_{L'}$ solutions, and the range of k_L for which these occur increases with γ.

As well as the difference regarding parallel decay, another difference from Fig. 3.3(b) is that the solutions now do not occur on straight lines with abrupt transitions at intersection points but instead make gradual transitions. This is due to the smoothness of the Langmuir/upper-hybrid dispersion relations which are unlike the abrupt change in frequency at k_* for the parallel Langmuir-z mode.
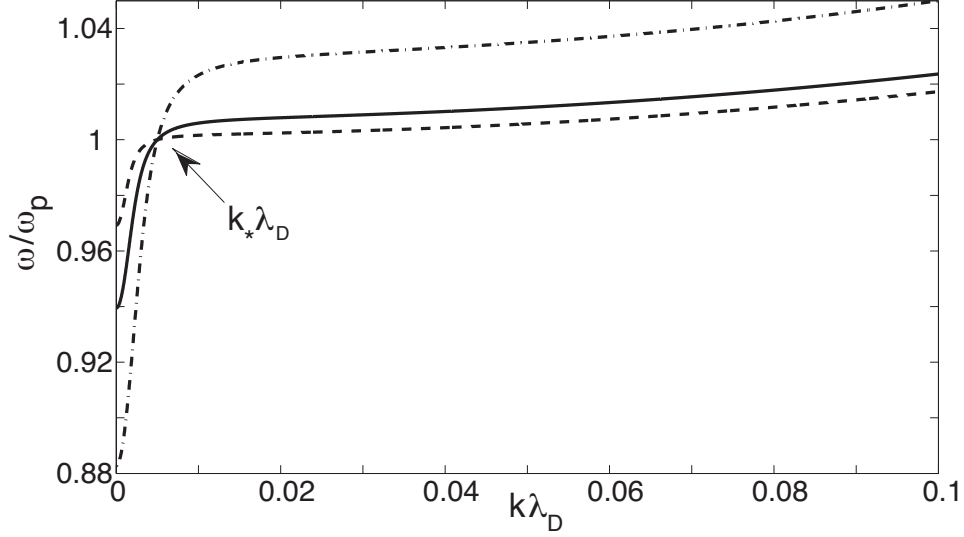
Figure 4.3: Dispersion relations of upper hybrid waves for $\omega_p/\Omega_e = 4$ (dash-dot line), $\omega_p/\Omega_e = 8$ (solid line), $\omega_p/\Omega_e = 16$ (dashed line), for $V_e/c = 5 \times 10^{-3}$.
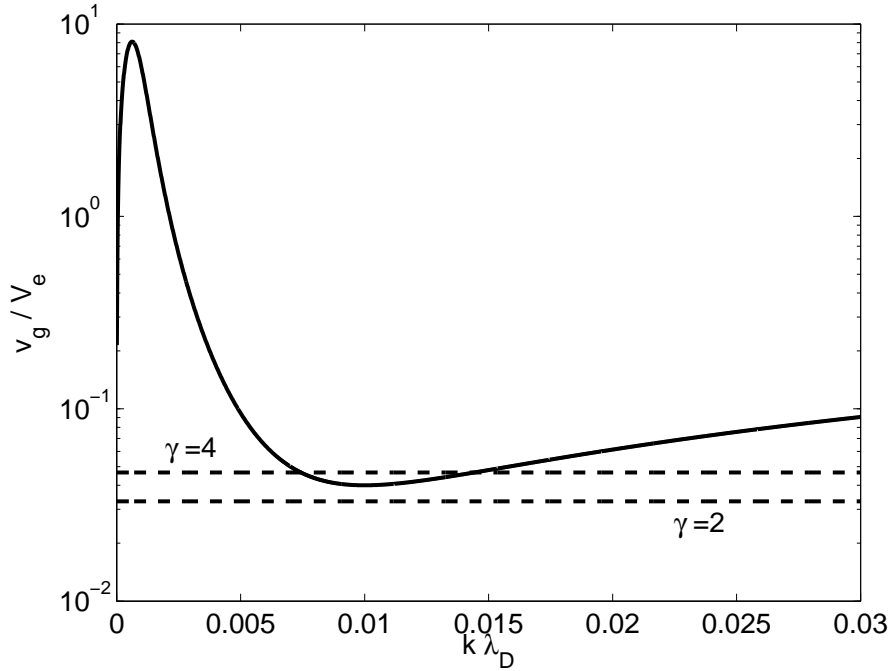

Figure 4.4: Group velocity of Langmuir/upper-hybrid waves (solid line) and ion sound waves (dashed lines) for $V_e/c = 5 \times 10^{-3}$, $\omega_p/\Omega = 50$, and $\gamma = 2, 4$.
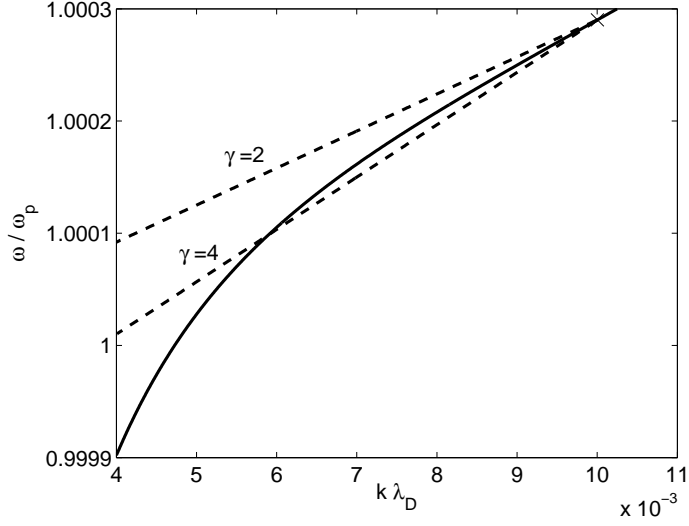
Figure 4.5: Graphical construction for decay of upper hybrid waves with $\theta_B = 90°$ using the same parameters as in Fig. 4.4, with primary wave number $k_L \lambda_D = 10^{-2}$ marked by a cross. The LHS and RHS of (4.5) are represented by solid lines and dashed lines, respectively. The LHS and RHS have no non-trivial intersection for $\gamma = 2$ but one intersection point for $\gamma = 4$.
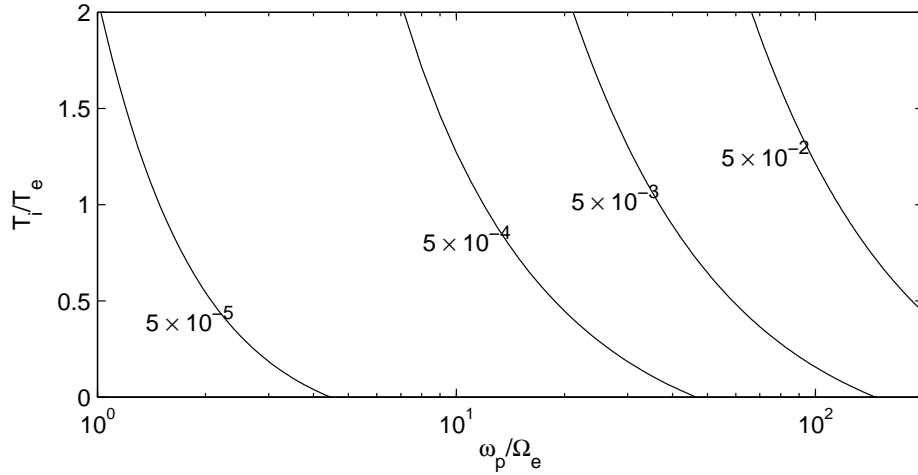

Figure 4.6: Minimum T_i/T_e as a function of ω_p/Ω_e for primary and daughter upper hybrid waves (with $\theta_B = 90°$) to have the same sign of $k_\perp$. Labeled values correspond to V_e/c.
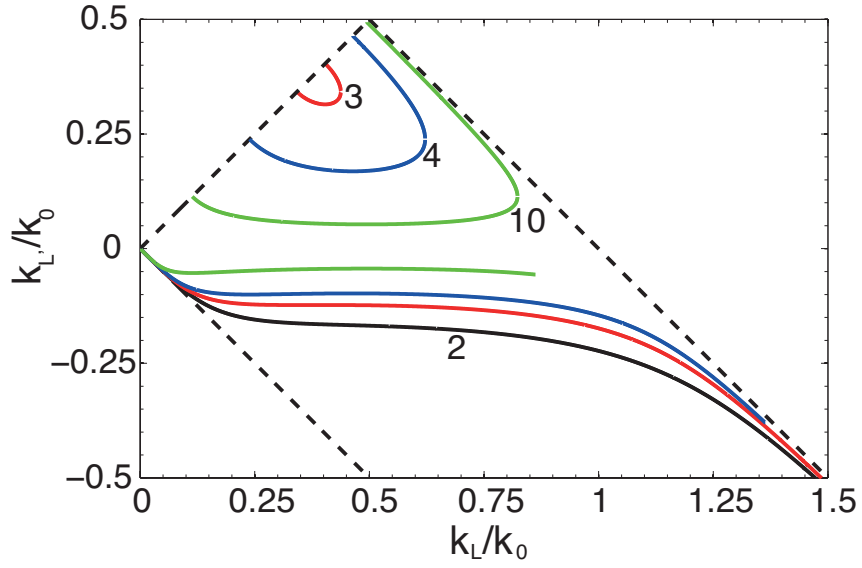
61

Figure 4.7: $k_{L'}$ versus k_L for upper hybrid waves with $\theta_B = 90°$ and $\omega_p/\Omega_e = 50$, for $\gamma = 2$ (black), $\gamma = 3$ (red), $\gamma = 4$ (blue), and $\gamma = 10$ (green).

Figure	ω_p/Ω_e	θ_B	γ	Low-f mode	k_L/k_0	Low $k_{L'}$	Orientation
4.9	50	0°	2	Ion sound	1.25	None	$\parallel$ to $\mathbf{B}_0$
4.10	50	0°	2	Ion sound	1.0	$-k_*$	$\parallel$ to $\mathbf{B}_0$
4.11	50	0°	2	Ion sound	~ 0.81	$\pm k_*$	$\perp$ to $\mathbf{B}_0$
4.12	50	0°	2	Ion sound	$0.2k_*$–$1.0k_*$	$< |\pm k_*|$	$\perp$ to $\mathbf{B}_0$
4.14	50	90°	2	Ion sound	2.0	None	$\perp$ to $\mathbf{B}_0$
4.15	50	90°	2	Ion sound	1.25	None	$\perp$ to $\mathbf{B}_0$
4.16	50	90°	2	Ion sound	0.1–1.0	$\pm k_*$	$\perp$ to $\mathbf{B}_0$
4.17	50	90°	2	Ion sound	0.466	$\pm k_*$	$\perp$ to $\mathbf{B}_0$
4.18	50	90°	3	Ion sound	0.466	$\pm k_*$	$\perp$ to $\mathbf{B}_0$
4.19	50	45°	2	Ion sound	1.0	None	Oblique
4.20	50	45°	2	Ion sound	0.6	$\pm k_*$	$\perp$ to $\mathbf{B}_0$
4.27	0.5	0°	2	Generalized $\omega_+(k)$	0.25–1.5	$\pm k_*$	$\parallel$ to $\mathbf{B}_0$
4.28	0.5	0°	2	Generalized $\omega_-(k)$	0.25–1.5	$-k_*$	$\parallel$ to $\mathbf{B}_0$

Table 4.1: Summary of kinematics calculations presented in Chapter 4.

4.6.2 Decay in 2D, primary wave vector parallel to $\mathbf{B}_0$

In this and later sections, the kinematics of electrostatic decay are calculated for a wide range of parameters. A summary of the various cases that are considered is presented in Table 4.1. The first of these cases is the 2D decay solutions obtained when the primary Langmuir wave-vectors are parallel to the magnetic field (i.e., $\theta_{B,L} = 0$). The dispersion surface for the Langmuir-z mode is shown in Fig. 4.8. We note that $\omega(k)/\omega_p$ increases faster along the parallel axis than the perpendicular axis.

For $k_L \gtrsim 2k_0$ magnetization effects become negligible and the magnetized decay solutions are approximated well by the unmagnetized kinematics. Figure 4.9 displays the decay solutions for $k_L/k_0 = 1.25$ for an unmagnetized (red) and magnetized (black) plasma. Decay solutions for the magnetized and unmagnetized plasma coincide along the $k_{\parallel}$ axis, as expected from the 1D analysis. However, for $\theta_{B,L'} > 0$ (where $\theta_{B,L'}$ is the angle between $\mathbf{k}_{L'}$ and $\mathbf{B}_0$) magnetized solutions have smaller $|\mathbf{k}_{L'}|$. This is because $\omega_L(k_{\parallel}, k_{\perp})$ increases faster along the $k_{\perp}$ axis than the $k_{\parallel}$ axis, as seen in Fig. 4.8 from the non-circular shape of the constant-frequency contours.
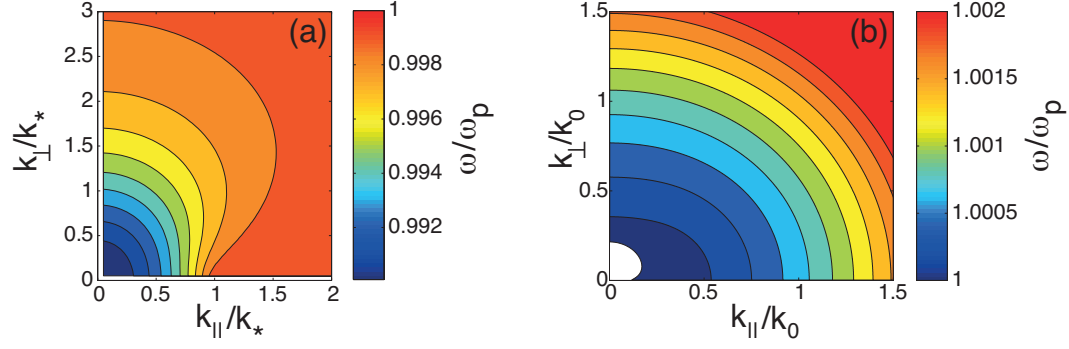
Figure 4.8: Dispersion surface for Langmuir-z mode, with wave number normalized by (a) k_* and (b) k_0.
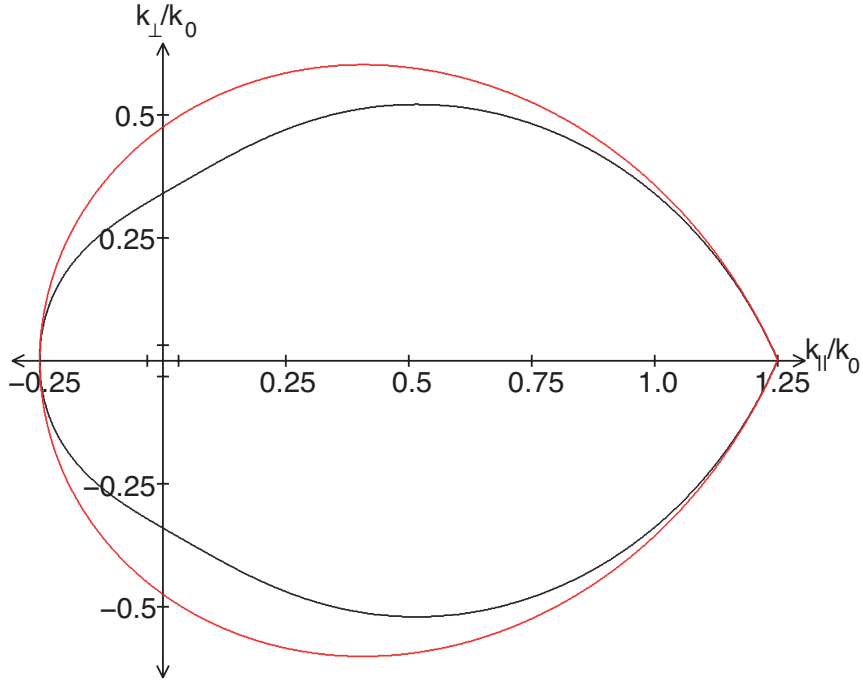

Figure 4.9: Solutions $k_{L'}$ for $k_L/k_0 = 1.25$ for magnetized Langmuir-z waves with $\omega_p/\Omega_e = 50$ and $\theta_B = 0$ (black line) and unmagnetized Langmuir waves (red line). Innermost ticks to the origin are $\pm k_*$.
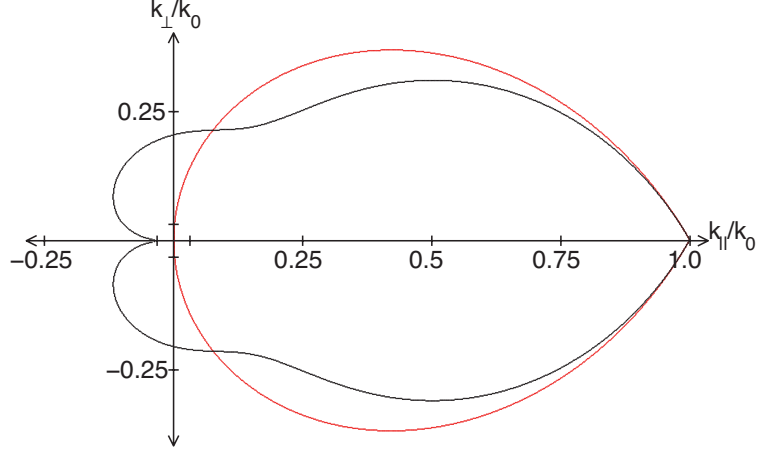
Figure 4.10: Solutions $k_{L'}$ for $k_L/k_0 = 1.0$ and otherwise identical conditions to Fig. 4.9.

Figure 4.10 displays the solutions for $k_{L'}$ given $k_L/k_0 = 1.0$. Solutions for the 1D case can be seen along the $k_{||}$ axis, with unmagnetized decay giving $k_{L'} = 0$ and magnetized decay giving $k_{L'} = -k_*$. In contrast to $k_L/k_0 = 1.25$, the magnetized solutions have greater $|\mathbf{k}_{L'}|$ for $\theta_{B,L'} \gtrsim 75°$. Also, solutions with $\theta_{LL'} > \pi/2$ are kinematically allowed only for a magnetized plasma.

Figure 4.11(a) shows $k_{L'}$ solutions for $k_L = 0.813k_0$. The solutions now form an inner and outer curve, with the inner curve containing the k_* solution on the parallel axis and the outer curve containing the $-k_*$ solution. As k_L decreases to $0.810k_0$ shown in Fig. 4.11(b), the topology of these solutions changes. There is now one closed curve which contains the $\pm k_*$ solutions, which are intrinsically associated with magnetization effects, and another closed curve which is well approximated by the unmagnetized forward-scatter results. For $k_L/k_0 = 0.6$ (Fig. 4.12), the forward-scatter solution curve centered at $0.5k_0$ has a smaller range of $k_\perp$ and $k_{||}$ than for $k_L/k_0 = 0.81$, but the curve centered at $k = 0$ containing the magnetized solutions remains approximately the same.

Figure 4.13 shows the decay solutions for $k_L/k_* = 0.2, ..., 1.0$. It can be seen that the range of $k_\perp$ for the solution curves becomes significantly smaller as k_L decreases, until at $k_L/k_* = 0.2$ all solutions have approximately the same $|\mathbf{k}_{L'}|$.

We note that Figs 4.10–4.12 demonstrate that low-k solutions for a magnetized plasma exist not only for $\theta_{LL'} = 0$, but occur for a range of $\theta_{LL'}$ albeit with $|k_{L'}|$ somewhat larger than k_*, reaching $\sim 5k_*$ at $\theta_{LL'} = \pi/2$. This demonstrates the important result that the 1D results persist into the general 2D domain.
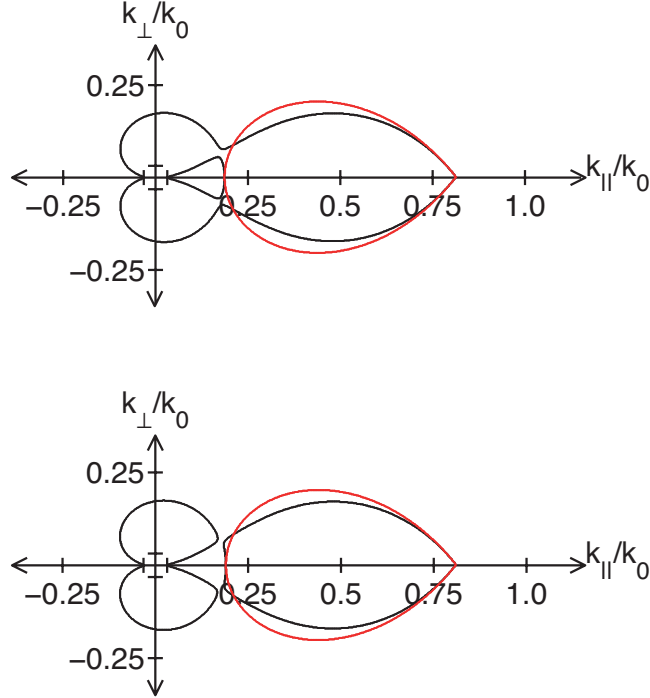
65

Figure 4.11: Solutions $k_{L'}$ for (a) $k_L/k_0 = 0.813$ and (b) $k_L/k_0 = 0.810$ and otherwise identical conditions to Fig. 4.9.
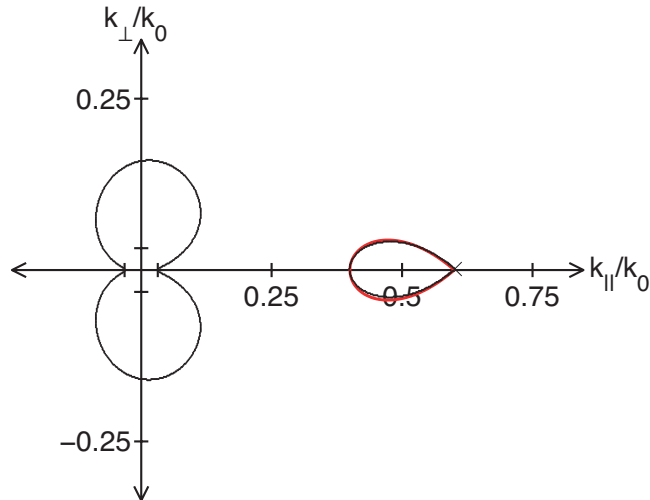

Figure 4.12: Solutions $k_{L'}$ for $k_L/k_0 = 0.6$ and otherwise identical conditions to Fig. 4.9.
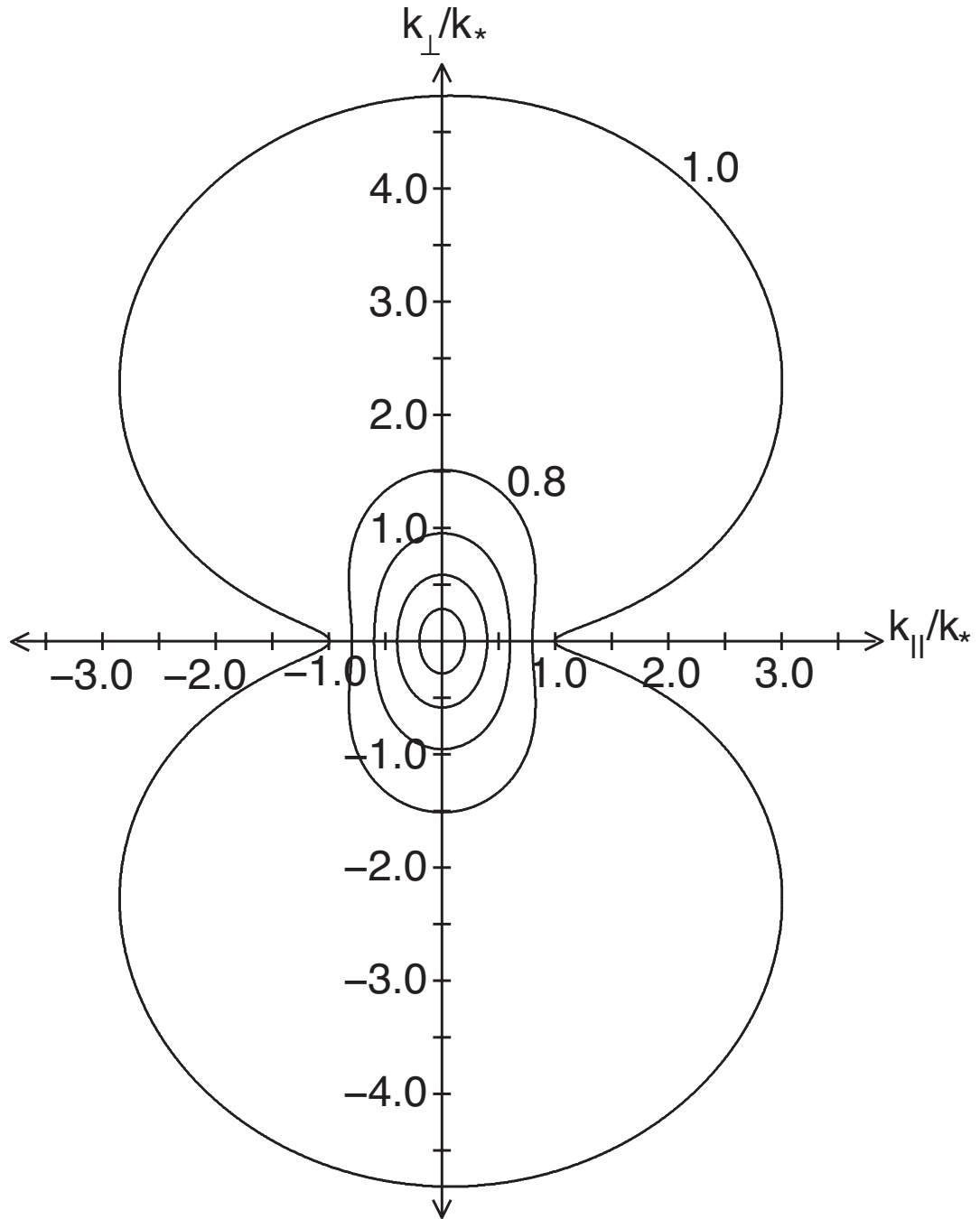
Figure 4.13: Solutions $k_{L'}$ for $k_L/k_* = 0.2, 0.4, ..., 1.0$ and otherwise identical conditions to Fig. 4.9, where the solution curves for 0.8 and 1.0 are labeled.

4.6.3 Decay in 2D, primary wave vector perpendicular to $\mathbf{B}_0$

We now describe the 2D solutions for the decay when the primary wave is a perpendicular upper hybrid wave.

For $k_L \gtrsim 2k_0$, the unmagnetized and magnetized solutions coincide well. For instance, Fig. 4.14 shows the magnetized solutions for $k_L = 2k_0$, which are almost indistinguishable from the unmagnetized solutions at this wave number. For $k_L = 1.25k_0$ (Fig. 4.15) we see that the unmagnetized approximation still gives good agreement with the magnetized results. As opposed to the 2D Langmuir-z decay for $\mathbf{k}||\mathbf{B}_0$, the magnetized results have larger $k_{L'}$, not smaller, for the same $\theta_{B,L'}$, as shown by comparing Figs 4.9 and 4.15.

Figure 4.16 displays the solution curves for a range of k_L/k_0 for $\gamma = 2$. For $k_L \leq 0.6k_0$, the solution curves intersect the $k_{||}$ axis near $\pm k_*$. This demonstrates that the $\pm k_*$ solutions found for the decay of Langmuir-z waves are valid not only for parallel propagation of the primary L wave but also for perpendicular propagation.

We now confirm the 1D result that the possibility of decay to positive (forward-scatter) $k_{L',\perp}$ is dependent on γ. Figure 4.17 shows the decay for $k_L/k_0 = 0.466$ and $\gamma = 2$. It can be seen that the only solution on the $k_\perp$ axis with $k_{L'} > 0$ is the trivial solution $k_L = k_{L'}$. Figure 4.18 shows the corresponding case for $\gamma = 3$, where in addition to the trivial solution $\mathbf{k}_L = \mathbf{k}_{L'}$ we now see a forward-scatter solution at $k_{L'} \approx 0.35k_0$.

4.6.4 Decay in 2D, primary wave vector oblique to $\mathbf{B}_0$

The kinematics for primary Langmuir waves propagating obliquely to the magnetic field are presented here for the particular case of $\theta_B = 45°$. The kinematics for $k_L/k_0 = 1.0$, which is the oblique analog of Fig. 4.10 (parallel) and 4.16 (perpendicular), are shown in Fig. 4.19. Magnetized solutions are well approximated by the unmagnetized solutions, with the main difference being that magnetized solutions are shifted towards more negative $k_\perp$.

Kinematics for $k_L/k_0 = 0.6$ are shown in Fig. 4.20, for which the equivalent parallel and perpendicular results are shown in Fig. 4.12 and Fig. 4.16. In this case unmagnetized kinematics can be seen to be a poor approximation to the magnetized kinematics. Like the perpendicular case, solutions for $\mathbf{k}_{L'}$ comprise one curve and not two as for the parallel case. Solutions at $\pm k_*$ can be seen on the $k_{||}$ axis, again confirming that these low-$k_{L'}$ exist in the general 2D case.
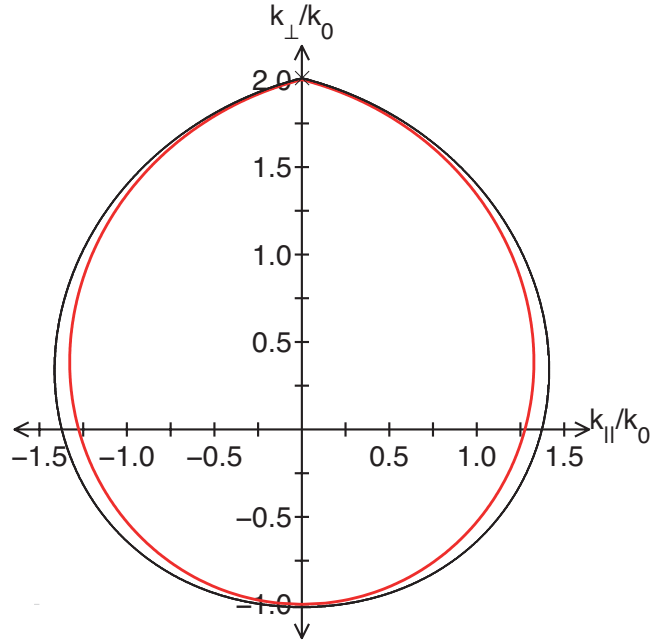
Figure 4.14: Solutions $k_{L'}$ for $k_L/k_0 = 2.0$ and $\gamma = 2$ for upper hybrid waves with $\theta_B = 90°$ and $\omega_p/\Omega_e = 50$.
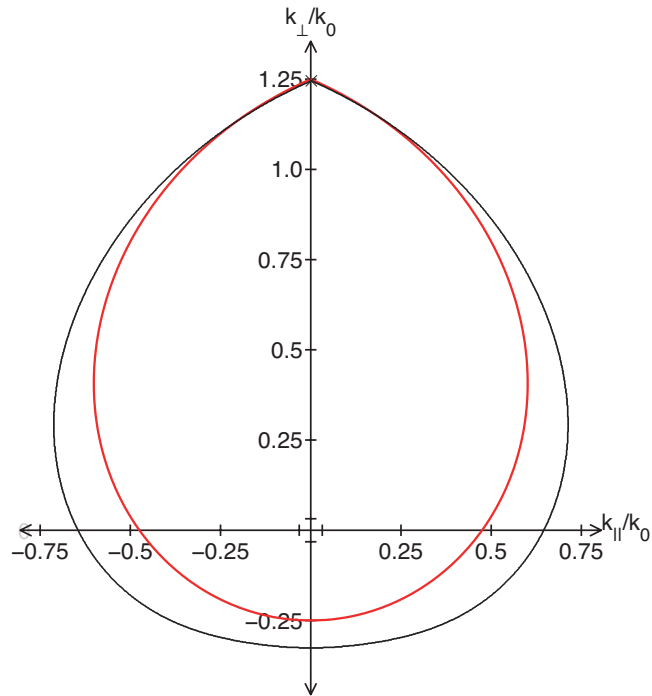

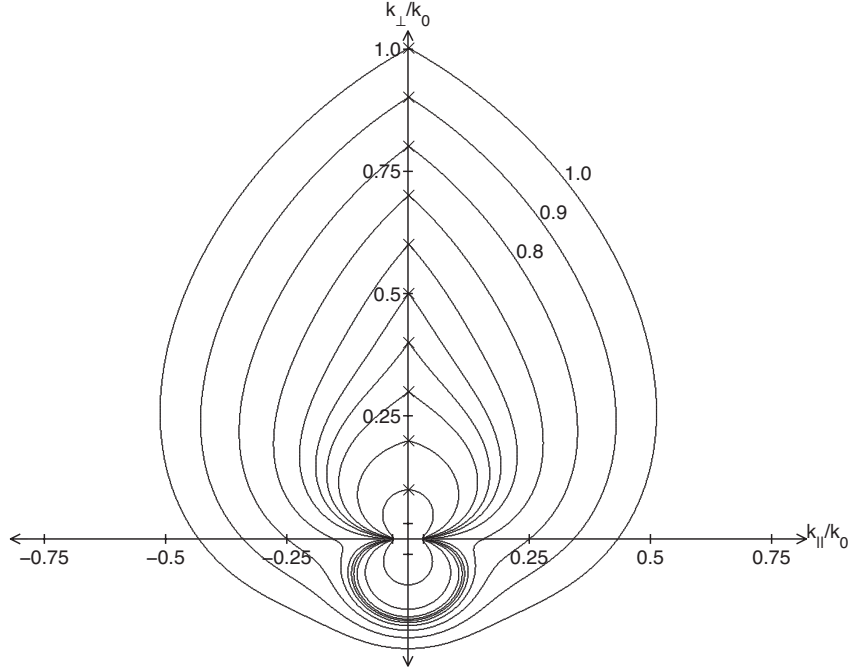Figure 4.15: Solutions $k_{L'}$ for $k_L/k_0 = 1.25$ and otherwise identical conditions to Fig. 4.14.

Figure 4.16: Solutions $k_{L'}$ for $k_L/k_0 = 0.1, 0.2, ..., 1.0$, as labeled, with otherwise identical conditions to Fig. 4.14.
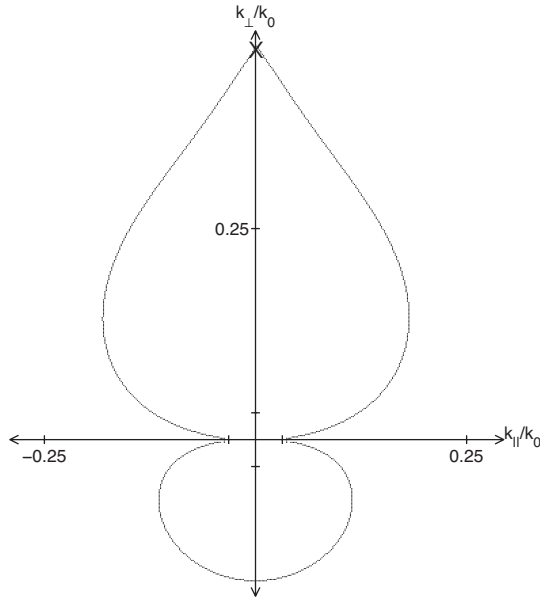

Figure 4.17: Solutions $k_{L'}$ for $k_L/k_0 = 0.466$ (represented by a cross) and otherwise identical conditions to Fig. 4.14.
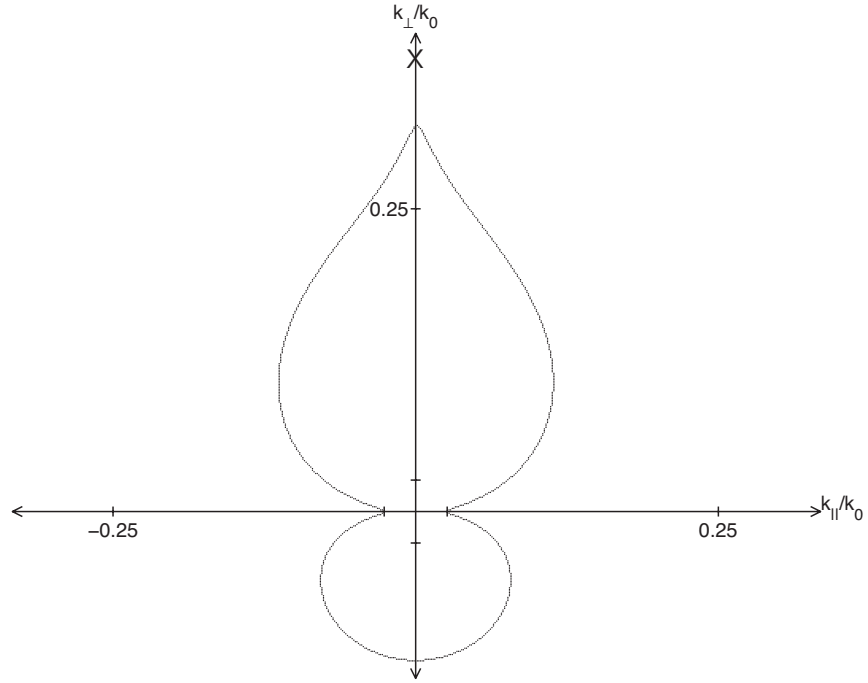
70

Figure 4.18: Solutions $k_{L'}$ for the same parameters as for Fig. 4.17 except that $\gamma = 3$. There are no solutions between the cross and the curve.
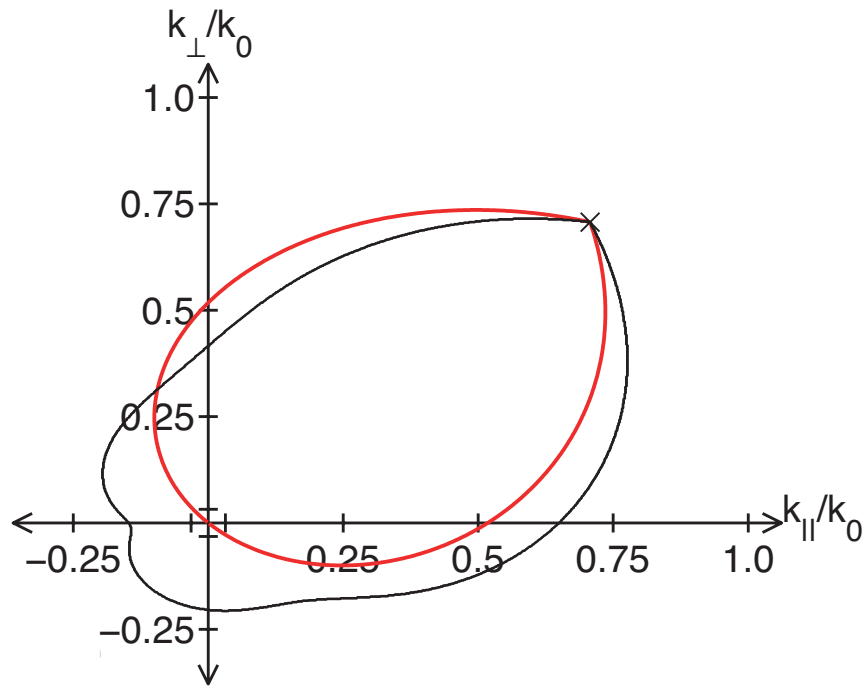

Figure 4.19: Solutions for $\mathbf{k}_{L'}$ for $k_L/k_0 = 1.0$, $\theta_B = 45°$, and $\omega_p/\Omega_e = 50$.
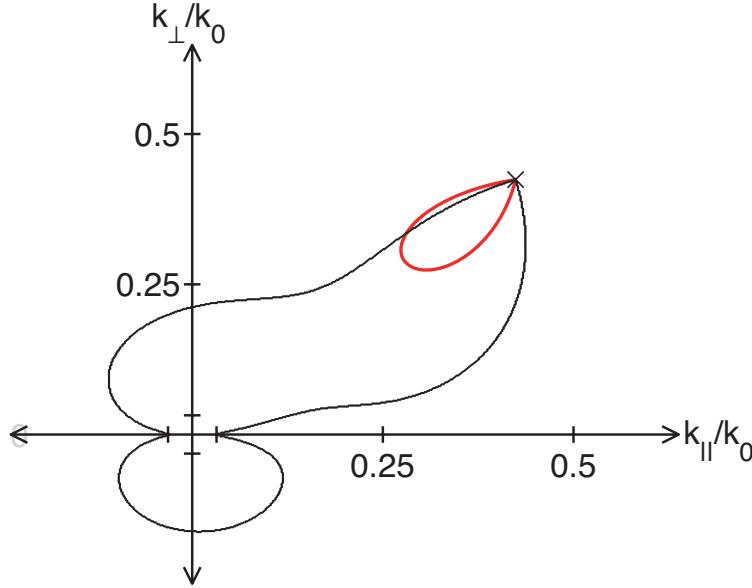
Figure 4.20: Analog of Fig. 4.19 for $k_L/k_0 = 0.6$.

4.7 Kinematics in strongly magnetized plasmas

We now investigate the case where $\Omega_e > \omega_p$. In this case, the mode which has Langmuir-like dispersion at high k has whistler-like dispersion for low k. This is termed the Langmuir-whistler mode. There are two low-frequency modes that are relevant for a strongly magnetized plasma, which in the limit of parallel propagation are the unmagnetized ion sound mode and the magnetized ion cyclotron mode. We discuss the kinematics of decay involving both of these modes. Only the case where $\mathbf{k}_L$ is parallel to $\mathbf{B}_0$ is considered here, since the Langmuir-whistler mode frequency is too small to satisfy the wave-matching conditions when $\mathbf{k}_L$ is perpendicular to $\mathbf{B}_0$.

4.7.1 Low-frequency modes

As stated above, there are two low-frequency modes that exist in a magnetized plasma. Using cold plasma theory, their dispersion relations are [*Melrose, 1986a*]

$$\omega_{\pm}^2 = \frac{1}{2}[\omega_S^2(k) + \Omega_i^2] \pm \frac{1}{2}\{[\omega_S^2(k) + \Omega_i^2]^2 - 4\omega_S^2(k)\Omega_i^2\cos^2\theta\}^{1/2}. \qquad (4.12)$$
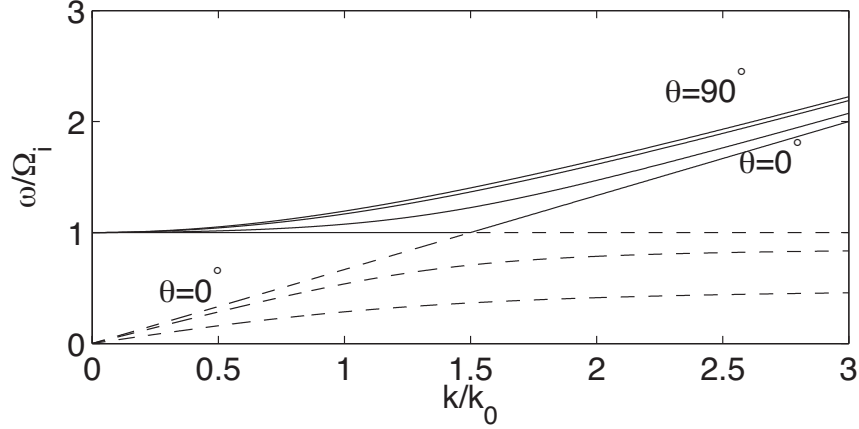
Figure 4.21: Dispersion relations for ω_+ (solid) and ω_- (dashed) from (4.12) for $\Omega_e/\omega_p = 2$, $\gamma = 2$, and $\theta = 0°, 30°, 60°, 90°$, as labeled. For $\theta = 90°$ the ω_- mode has a zero frequency for all k.

Figure 4.21 displays $\omega_\pm(k)$ for various θ. For parallel propagation ($\cos^2\theta = 1$), the dispersion relations reduce to the unmagnetized ion sound mode [Eq. (4.2)] and the ion cyclotron mode ($\omega = \Omega_i$). We will calculate the kinematics for both ion sound waves and ion cyclotron waves in 1D. As θ increases, these dispersion relations split apart in (ω, k); ω_+ has ion-cyclotron-like dispersion at low k and ion-sound-like dispersion at high k, and vice-versa for the ω_- mode. At $\theta = 90°$, $\omega_+(k) = \sqrt{\omega_S(k)^2 + \Omega_e^2}$ and $\omega_-(k) = 0$. Decay kinematics involving both the ω_+ and ω_- modes will be calculated for the 2D case.

4.7.2   Decay in 1D, wave vectors parallel to $\mathbf{B}_0$

The Langmuir-whistler mode has very similar dispersion to the Langmuir-z mode near ω_p, in that there is a rapid change in $\partial\omega/\partial k$ near an equivalent k_*, defined by $k_* = (V_e/c)(1 - \omega_p/\Omega_e)^{-1/2}$. This is demonstrated in Fig. 4.22 for $\Omega_e/\omega_p = 2$ and $V_e/c = 5 \times 10^{-3}$, giving $k_*\lambda_D = 7.1 \times 10^{-3}$. However, the Langmuir-whistler mode differs from the Langmuir-z mode in its cutoff frequency, which is on the order of Ω_i rather than $\omega_p - \Omega_e/2$.

Figure 4.23 shows the graphical construction for wave matching for both the ion sound mode and the ion cyclotron mode. Unlike the ion sound mode, decay solutions for the ion cyclotron mode are symmetric in $\pm k_{L'}$ because its dispersion relation is independent of k.

We first calculate the kinematics for the decay of a Langmuir-whistler wave into another Langmuir-whistler wave and an ion sound wave. The results are

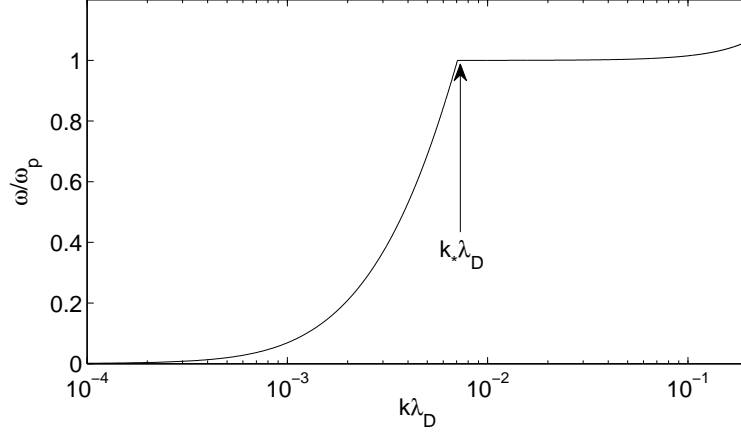Figure 4.22: Langmuir-whistler dispersion relation for $\Omega_e/\omega_p = 2$, $V_e/c = 5 \times 10^{-3}$, and $\theta_B = 0$.
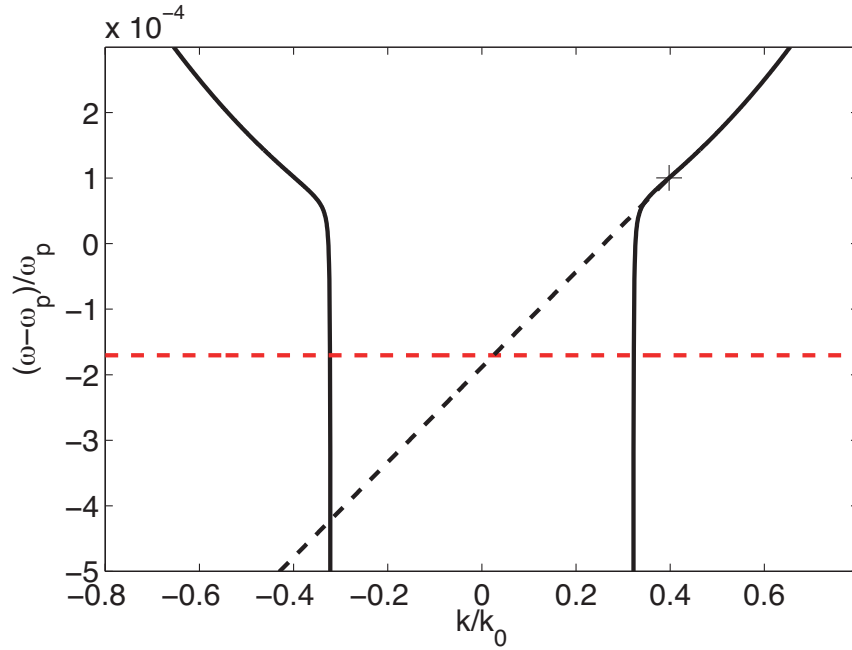

Figure 4.23: Graphical construction for 1D decay solutions for $k_L/k_0 = 0.4$ (+ sign on Langmuir-whistler mode), $\Omega_e/\omega_p = 2$, $V_e/c = 5 \times 10^{-3}$, $\gamma = 2$, and $\theta_B = 0$, for the ion sound mode (black dashed line) and the ion cyclotron mode (red dashed line).

shown as the red curve in Fig. 4.24, for the case $\Omega_e/\omega_p = 2$, $V_e/c = 5 \times 10^{-3}$, and $\gamma = 2$, giving $k_*/k_0 = 0.32$. The kinematics are qualitatively the same as for decay of the Langmuir-z mode for $\theta_B = 0$, including the solutions at $\pm k_*$, as can be seen from comparisons with Fig. 3.3.

We also calculate the kinematics for the decay when the low-frequency mode is the ion cyclotron mode, shown as the black curve in Fig. 4.23. In this case, solutions with negative $k_{L'}$ are approximately equal to those for the ion sound mode when $k_L \lesssim k_0 + k_*$. When $k_{L'} \gtrsim k_0 + k_*$, decay involving the ion cyclotron mode has a larger magnitude of $k_{L'}$. Another difference from decay into ion sound waves is that positive $k_{L'}$ solutions exist for all k_L. This is due to the ion cyclotron mode having a comparatively large frequency of Ω_i for all k, allowing the wave-matching conditions to be satisfied.

4.7.3 Decay in 1D, wave vectors perpendicular to B$_0$

As discussed above, of the $\omega_\pm(k)$ modes only the $\omega_+(k)$ mode has nonzero frequency for $\theta_B = 90°$. The Langmuir-whistler mode for $\theta_B = 90°$ has a frequency near ω_{pi}. Figure 4.25 shows the kinematics for this process. For all k_L there is both a positive $k_{L'}$ solution as well as a negative $k_{L'}$ solution with smaller magnitude. We also note that decay can reduce the Langmuir-whistler wave number significantly, e.g., from $k_L = 4k_0$ to $k_{L'} \approx 0.2k_0$ in a single decay.

4.7.4 Decay in 2D, primary wave vector parallel to B$_0$

The Langmuir-whistler dispersion surface is shown in Fig. 4.26. We note that the contours of ω_L for the Langmuir-whistler mode are dissimilar to those of the Langmuir-z mode in Fig. 4.8. Whereas the Langmuir-z mode had contours that resembled ellipses and had frequency increasing with $k_\perp$, the Langmuir-whistler mode's contours resemble hyperbolas and its frequency decreases with increasing $k_\perp$. This leads to very different kinematics in 2D.

Figure 4.27 shows the kinematics for $k_L/k_0 = 0.25, 0.5, ..., 1.5$, with the ω_+ mode as the low-frequency wave. The solutions obtained resemble pairs of hyperbolas, and unlike the weakly magnetized case there are no closed families of solutions near k_*. For $k_L > k_*$, these hyperbolas have a much smaller range of allowed $\theta_{LL'}$. A surprising result is that $k_{L'} > k_L$ for all k_L, as opposed to the Langmuir-z mode where $k_{L'} < k_L$ for all k_L. The reason for this is that ω_L decreases as $k_\perp$ increases for a given $k_{\|L}$, as described above.

The corresponding calculations for the ω_- mode are shown in Fig. 4.28.
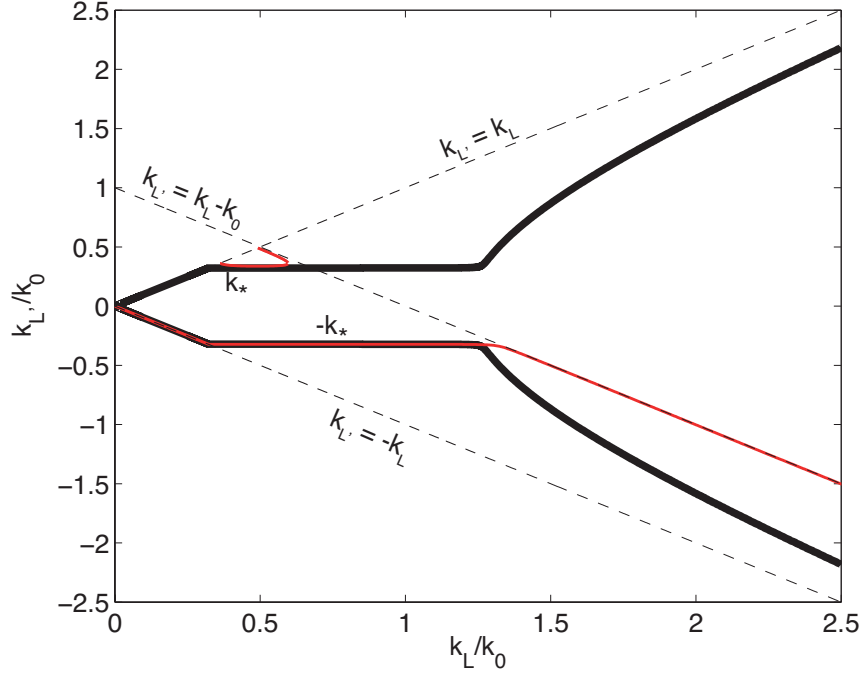
Figure 4.24: Solutions for $k_{L'}$ as a function of k_L for $\Omega_e/\omega_p = 2$ and $\theta_B = 0$, for decay of a Langmuir-whistler wave to an ion sound wave (red) or an ion cyclotron wave (black). Dashed lines represent $k_{L'} = k_L$, $k_{L'} = -k_L$, and $k_{L'} = k_L - k_0$, as labeled. Also, $k_{L'} = \pm k_*$ is labeled.
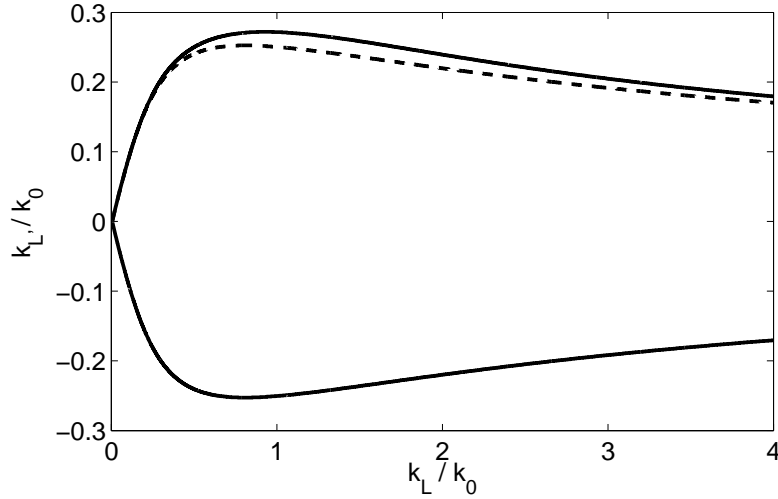
Figure 4.25: $k_{L'}$ (solid lines) as a function of k_L for $\Omega_e/\omega_p = 2$ and wave vectors perpendicular to the magnetic field. Dashed line represents the absolute value of the negative $k_{L'}$ solutions to aid comparison.

Figure 4.26: Frequency ω/ω_p of the Langmuir-whistler mode as a function of $k_{||}/k_0$ and $k_\perp/k_0$ for $\Omega_e/\omega_p = 2$ and $V_e/c = 5 \times 10^{-3}$.

Figure 4.27: Solutions for $k_{L'}/k_0$ for the ω_+ mode with $\theta_B = 0$ and $\Omega_e/\omega_p = 2$, given $k_L/k_0 = 0.25, 0.5, ..., 1.5$.

Figure 4.28: Analog of Fig. 4.27 for the ω_- mode.

Solutions for $k_{L'}$ when $k_L < k_*$ are qualitatively similar to those for the ω_+ mode. However, for $k_L > k_*$, there are only solutions at $k_{L'} = -k_*$ and not $k_{L'} = k_*$.

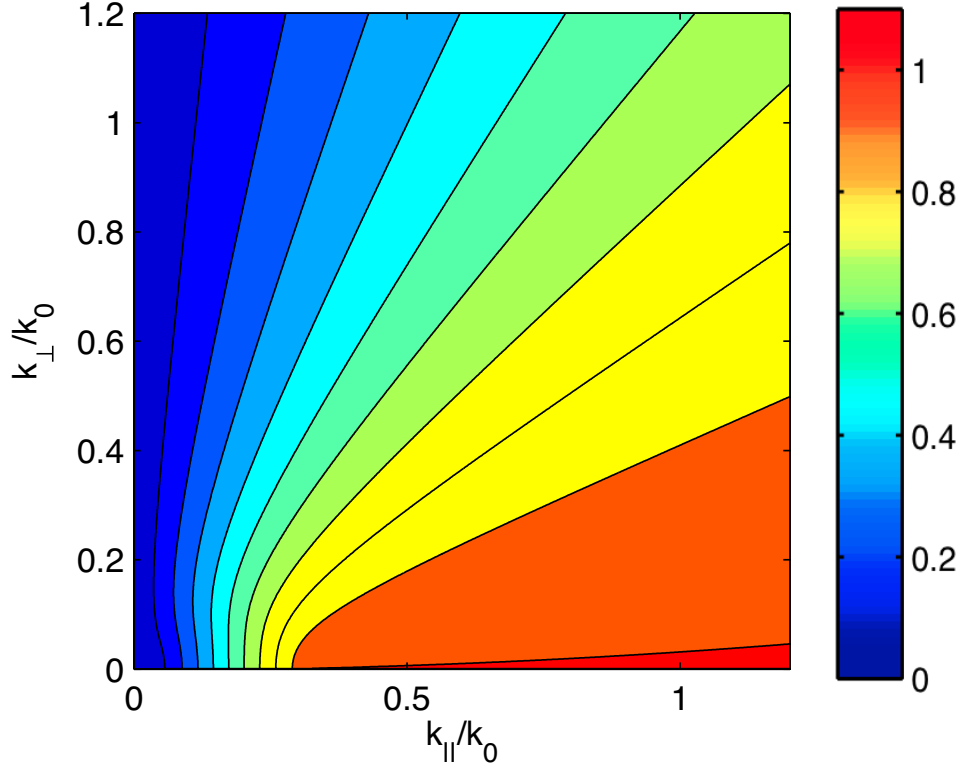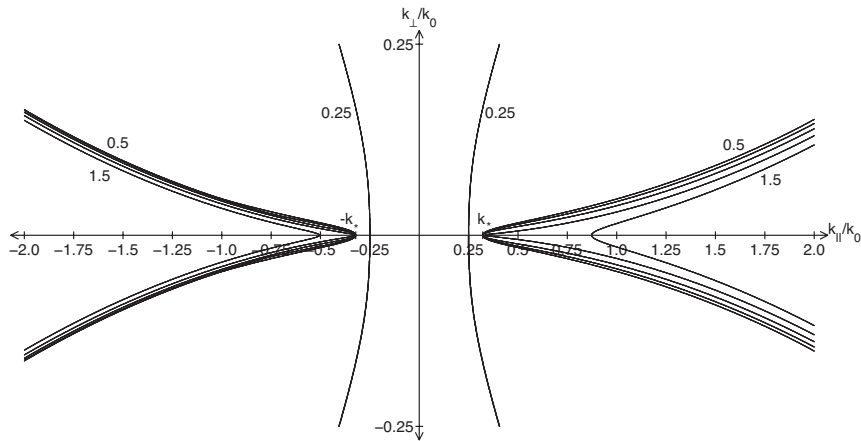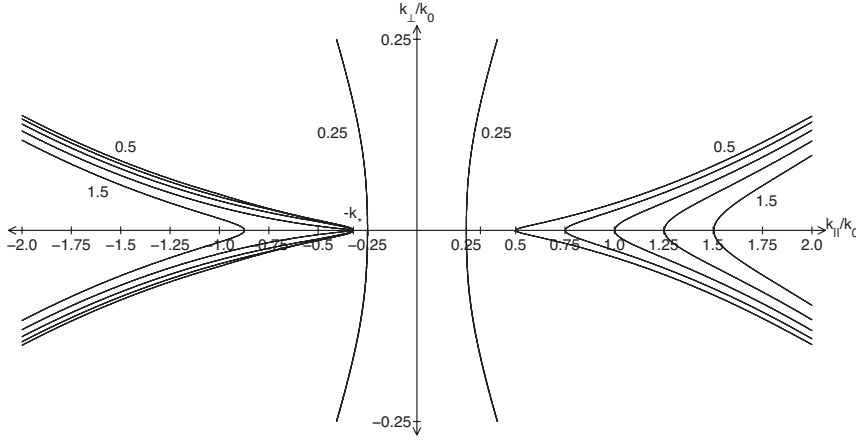One consequence of the above results is that the Langmuir-whistler waves resulting from decay should be confined to a relatively narrow range of $\theta_{LL'}$. We also predict that decay increases, rather than decreases, the wave numbers of Langmuir-whistler waves subject to three-wave decay when $\omega_p/\Omega_e < 1$.

4.8   Discussion

In this chapter we have presented the analysis of decay kinematics for the 2D case; i.e., where the wave vectors participating in the decay and the magnetic field direction are coplanar. Three-dimensional calculations of decay are also possible, in which the three wavevectors can have different azimuthal angles with respect to the magnetic field. However, such calculations are more difficult to perform numerically. Preliminary calculations of decay in 3D not shown here suggest that 2D calculations capture most of the qualitative features of decay in 3D.

Decay of Langmuir-whistler waves parallel to the magnetic field was found to allow solutions where $k_{L'} > k_L$, corresponding to an inverse cascade. By shifting these waves to larger k, we expect them to undergo Landau damping at a faster rate. Also, since this corresponds to a smaller wavelength, we would expect such waves to be more strongly modulated by small-scale density fluctuations.

4.9 Conclusion

We have for the first time calculated in detail the kinematics for the three-wave processes of Langmuir-like and ion-sound-like waves when magnetization is included. We have done this for both weakly and strongly magnetized plasmas and for parallel, perpendicular, and oblique propagation of the primary waves in both 1D and 2D.

For a weakly magnetized plasma, the solutions are well approximated by unmagnetized kinematics when $k_L \gtrsim 2k_0$ but there are important differences for $k_L \lesssim 2k_0$. One such difference is the existence of low-k solutions near k_*, which were previously shown to exist for the 1D parallel case and have now been confirmed to persist for arbitrary propagation angles of primary Langmuir-z waves. Another difference is that decay kinematics at oblique angles are not well approximated by unmagnetized kinematics for $k_L \lesssim k_0$.

For a strongly magnetized plasma, where the relevant wave mode is the Langmuir-whistler mode, the kinematics in 1D are very similar to those of a weakly magnetized plasma. However, in 2D the solutions are seen to be very different, with decay products confined to a narrow range of $\theta_{LL'}$, and $k_{L'}$ increasing as ion sound waves are generated. This is due to the different topology of the Langmuir-whistler mode surface compared with the Langmuir-z mode. Decays involving ion sound waves and ion cyclotron waves are qualitatively very similar for $\theta_{LL'} > \pi/2$, but for $\theta_{LL'} < \pi/2$ are qualitatively different, an example being the absence of k_* solutions for the ω_- mode.

Chapter 5

Quasilinear simulations of type III radio bursts with magnetized electrostatic decay

5.1 Abstract

Quasilinear simulations of electrostatic decay with magnetized kinematics are performed for a range of parameters consistent with type III solar radio burst sources. The dynamics of the decaying Langmuir waves are analyzed as a function of parameters such as beam wave number, beam width, electric field strength, and plasma temperatures. The growth rate of Langmuir waves at low wave numbers, where their polarization is transverse, is appreciable when trapping of Langmuir waves at low wave numbers by higher density regions (e.g., turbulence) is implemented.

5.2 Introduction

Type III radio bursts are caused by flare-accelerated electrons that drive Langmuir waves which are then converted into radio emission at the electron plasma frequency (ω_p) and its harmonic ($2\omega_p$) [*Wild*, 1950; *Ginzburg and Zhelezniakov*, 1958; *Melrose*, 1986a]. Nonlinear wave-wave interactions, such as electrostatic decay, are thought to be the dominant mechanism for converting these beam-driven Langmuir waves into the observed radio emission [*Lin et al.*, 1986; *Cairns and Robinson*, 1995a]. Previous studies have simulated type III bursts using quasilinear equations for the evolution and propagation of the electron beam and for the generation and propagation of Langmuir waves, combined with equations describing the nonlinear electrostatic decay process and nonlinear

wave-wave coupling processes that produce ω_p and $2\omega_p$ radiation [*Li et al.*, 2002, 2003]. These were able to reproduce a number of features of type III bursts, such as the presence of both fundamental and harmonic emission and the evolution of frequency with time.

Recent *in situ* observations of type III radio bursts [*Malaspina et al.*, 2010; *Graham et al.*, 2012a] have demonstrated a previously unseen feature of Langmuir waves in these source regions; namely, under certain conditions there is substantial energy density in the electric field component perpendicular to the magnetic field (and presumably the wave vector). This was interpreted as evidence for some energy being in the transversely-polarized z mode, which is the magnetized counterpart of the Langmuir mode at low wave numbers. This suggests magnetization effects are important in the modeling of type III bursts.

Recently the effects of magnetization on the kinematics of electrostatic decay were derived, shown to be important, and included some preliminary quasilinear simulations of a type III radio burst source region (Chapter 4 and *Layden et al.* [2013]). However, the importance of magnetization effects over a wide range of plasma parameters was not investigated.

In this chapter, we investigate in detail the effects of varying the plasma parameters on electrostatic decay when magnetization is included in the wave kinematics. Although the primary observational interest is the state of the system at large times (such as discussed in Sec. 3.4), due to time constraints our focus in this chapter is on the initial stages of growth of the perpendicular electric field. The outline of the chapter is as follows. Section 5.3 summarizes the one-dimensional quasilinear equations used in our simulations. This is followed by a derivation of the nonlinear rates for the electrostatic decay process which are implemented in the simulations. Section 5.4 presents the results of the simulations, focusing on the levels of waves in the perpendicular wave field component and the timescales of the decay. This is followed by a discussion and the conclusions.

5.3   Theory

In this section we first present the one-dimensional quasilinear equations for wave and particle evolution including nonlinear electrostatic decay that we use in our simulations. Since we are predominantly interested in magnetization effects for the decay process, we use the unmagnetized form of the quasilinear equations; this corresponds to neglecting the cyclotron motion of the particles

and associated resonances. We next derive the nonlinear rate for electrostatic decay of magnetized Langmuir-z waves. Finally we describe the Langmuir wave source that we implement and the method of implementing a density well that traps Langmuir waves.

5.3.1 Quasilinear equations

The quasilinear equations for the occupation number $N_M(k)$ and particle distribution function $f(v)$ are [*Melrose*, 1986a; *Li et al.*, 2003]

$$\frac{\partial N_M(k)}{\partial t} + v_M(k)\frac{\partial N_M(k)}{\partial x} = \alpha(k) - \gamma(k)N_M(k) + \frac{\partial N_M(k)}{\partial t}\bigg|_{NL} + S(t,x,k), \quad (5.1)$$

$$\frac{\partial f(v)}{\partial t} + v\frac{\partial f(v)}{\partial x} = \frac{\partial}{\partial v}\left[A(v)f(v) + D(v)\frac{\partial f(v)}{\partial v}\right], \quad (5.2)$$

where

$$v_M(k) = \frac{\partial \omega_M(k)}{\partial k}, \quad (5.3)$$

$$\alpha(k) = \frac{e^2}{4\epsilon_0\hbar}\frac{v^3}{V_e^2}(1 - k^2\lambda_D^2)f(v)\bigg|_{v=\omega/k}, \quad (5.4)$$

$$\gamma(k) = -\frac{\pi e^2}{m_e\epsilon_0}\frac{v^3}{V_e^2}k\lambda_D^2\frac{\partial f(v)}{\partial v}\bigg|_{v=\omega/k}, \quad (5.5)$$

$$A(v) = \frac{e^2}{8\pi m_e\epsilon_0}\frac{v^2}{V_e^2}k^2(1 - k^2\lambda_D^2)\bigg|_{k=\omega/v}, \quad (5.6)$$

$$D(v) = \frac{e^2\hbar}{2m_e^2\epsilon_0}\frac{v^2}{V_e^2}k^3\lambda_D^2 N(k)\bigg|_{k=\omega/v}. \quad (5.7)$$

In (5.1) and (5.2) the t and x arguments of N_M and f are omitted for brevity. Here $\partial N_M(k)/\partial t|_{NL}$ is the nonlinear electrostatic decay rate for the mode M (= L, L', or S), $S(t,x,k)$ is a source term for Langmuir waves, γ is an absorption coefficient, D is a diffusion coefficient, and α and A are coefficients related to spontaneous emission.

5.3.2 Nonlinear rates

The nonlinear rate equations for the electrostatic decay process $L(k_L) \rightarrow L'(k_{L'}) + S(k_S)$ are [*Melrose*, 1986a; *Li et al.*, 2003]

$$\left.\frac{\partial N_L(k_L)}{\partial t}\right|_{NL} = -\int dk_S \int dk_{L'} \hat{N}(k_L, k_{L'}, k_S)$$
$$\times \delta(k_L - k_{L'} - k_S)\delta[\omega_L(k_L) - \omega_{L'}(k_{L'}) - \omega_S(k_S)], \quad (5.8)$$

$$\left.\frac{\partial N_{L'}(k_{L'})}{\partial t}\right|_{NL} = \int dk_S \int dk_L \hat{N}(k_L, k_{L'}, k_S)$$
$$\times \delta(k_L - k_{L'} - k_S)\delta[\omega_L(k_L) - \omega_{L'}(k_{L'}) - \omega_S(k_S)], \quad (5.9)$$

$$\left.\frac{\partial N_S(k_S)}{\partial t}\right|_{NL} = \int dk_L \int dk_{L'} \hat{N}(k_L, k_{L'}, k_S)$$
$$\times \delta(k_L - k_{L'} - k_S)\delta[\omega_L(k_L) - \omega_{L'}(k_{L'}) - \omega_S(k_S)], \quad (5.10)$$

where

$$\hat{N}(k_L, k_{L'}, k_S) = G\omega_S(k_S)[N_L(k_L)N_{L'}(k_{L'}) - N_{L'}(k_{L'})N_S(k_S) + N_S(k_S)N_L(k_L)],$$
$$(5.11)$$

and

$$G = \frac{\hbar e^2 (1 + 3T_i/T_e)}{8\epsilon_0 m_e^2 V_e^2}. \quad (5.12)$$

The variable $\hat{N}$ includes the nonlinear absorption and emission processes discussed in Sec. 1.3.2.

Equation (5.8) can be simplified by firstly integrating over $k_{L'}$ to give

$$\left.\frac{\partial N_L(k_L)}{\partial t}\right|_{NL} = -\int dk_S \hat{N}(k_L, k_L - k_S, k_S)\delta[\omega_L(k_L) - \omega_{L'}(k_L - k_S) - \omega_S(k_S)],$$
$$(5.13)$$

and then integrating over k_S to give

$$\left.\frac{\partial N_L(k_L)}{\partial t}\right|_{NL} = -\sum_{k_L - k_{L'} - k_S = 0} \frac{\hat{N}(k_L, k_{L'}, k_S)}{\left|\frac{\partial}{\partial k_S}[\omega_L(k_L) - \omega_{L'}(k_L - k_S) - \omega_S(k_S)]\right|}, \quad (5.14)$$

where the sum is performed over the kinematically allowed triples of k_L, $k_{L'}$, and k_S. To derive (5.14) we have used the formula

$$\int dx\, g(x)\, \delta[f(x)] = \sum_i \frac{g(x_i)}{|f'(x_i)|}, \quad (5.15)$$

where the sum is over the roots x_i of $f(x)$. The term $\partial \omega_L / \partial k_S$ in the denominator of (5.14) equals zero, and we evaluate other terms using the chain rule so that

$$\left. \frac{\partial N_L(k_L)}{\partial t} \right|_{NL} = - \sum_{k_L - k_{L'} - k_S = 0} \frac{\hat{N}(k_L, k_{L'}, k_S)}{\left| - \frac{\partial \omega_{L'}(k_L - k_S)}{\partial(k_L - k_S)} \frac{\partial(k_L - k_S)}{k_S} - \frac{\partial \omega_S(k_S)}{k_S} \right|}. \qquad (5.16)$$

Substituting (5.3) into (5.16) then yields

$$\left. \frac{\partial N_L(k_L)}{\partial t} \right|_{NL} = - \sum_{k_L - k_{L'} - k_S = 0} \frac{\hat{N}(k_L, k_{L'}, k_S)}{|v_L(k_{L'}) - v_S|}. \qquad (5.17)$$

Analogous calculations for (5.9) and (5.10) yield

$$\left. \frac{\partial N_{L'}(k_{L'})}{\partial t} \right|_{NL} = \sum_{k_L - k_{L'} - k_S = 0} \frac{\hat{N}(k_L, k_{L'}, k_S)}{|v_L(k_{L'}) - v_S|} \qquad (5.18)$$

and

$$\left. \frac{\partial N_S(k_S)}{\partial t} \right|_{NL} = \sum_{k_L - k_{L'} - k_S = 0} \frac{\hat{N}(k_L, k_{L'}, k_S)}{|v_L(k_L) - v_L(k_{L'})|}. \qquad (5.19)$$

5.3.3 Source and implementation

The source of Langmuir waves (either beam-driven or the products of previous decay) is described by the function $S(t, x, k)$. We choose a Gaussian function in t and k and a steeper variation in x so that the source is contained within the simulation grid, namely,

$$S(t, x, k) = S_0 \exp\left[-\left(\frac{t - t_c}{\Delta t}\right)^2 - \left(\frac{x - x_c}{\Delta x}\right)^{16} - \left(\frac{k - k_c}{\Delta k}\right)^2 \right], \qquad (5.20)$$

where $S_0 = 2E_{\max}^2 / \epsilon_0 \hbar \omega_p \Delta t \Delta k$. As $t \to \infty$ the source has $E = E_{\max}$ at $x = x_c$, in the absence of any other sources of growth or damping. We choose the parameters $t_c = 0.1$ s, $\Delta t = 10^{-2}$ s, $x_c = 3600$ km, $\Delta x = 4000$ km.

We also include the effect of a plasma density well that causes reflection of low-k (i.e., $|k| < k_*$) Langmuir waves, such as may be present in the solar wind. The importance of such density wells on the dynamics of electrostatic decay was demonstrated in Chapter 3 but is analyzed in detail here. For propagation in 1D, reflection of Langmuir-z waves occurs when their frequency equals the z mode cutoff frequency $\omega_z \approx \omega_{p'} - \Omega_e/2 = (e^2 n'_e / m_e \epsilon_0)^{1/2} - \Omega_e/2$, where primed quantities represent their value at the reflective boundaries.
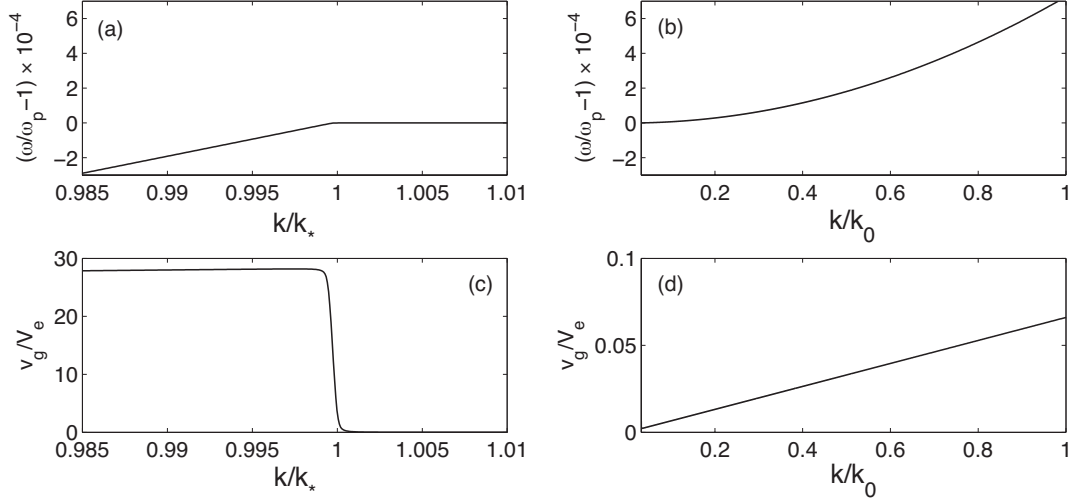
Figure 5.1: (a), (b) Dispersion relation $\omega(k)$ of Langmuir-z waves for $T_e = 1.7 \times 10^5$ K and $\omega_p/\Omega_e = 50$. (c), (d) Group velocity v_g normalized by electron thermal velocity V_e for the same parameters.

Langmuir-z waves near k_* have frequencies $\sim \omega_p$, thus reflection occurs when $\omega_p = \omega_{p'} - \Omega_e/2$. Substituting a typical parameter for the electron cyclotron frequency $\Omega_e = \omega_p/50$ yields $\omega_{p'}/\omega_p = 1.01$, or In terms of plasma density, $n_{e'}/n_e = (\omega_{p'}/\omega_p)^2 \approx 1.02$; i.e., an increase in density of 2%.

Reflection of Langmuir waves is implemented in the simulations by defining the left and right boundaries at given spatial positions in the simulation grid, then at each time step the quanta N_L propagating past the right (left) boundary at positive (negative) k are removed and added to N_L at negative (positive) k.

5.4   Results

In this section, we present the results of quasilinear simulations using a range of Langmuir wave and plasma parameters that are consistent with type III source regions at 1 AU. The electron temperature and magnetization strength are kept constant at $T_e = 1.7 \times 10^5$ K (or $V_e/c = 5.35 \times 10^{-3}$) and $\omega_p/\Omega_e = 50$, respectively. These parameters fully determine the dispersion relation $\omega_L(k)$ and group velocity v_g of the Langmuir waves, which are plotted in Fig. 5.1. The remaining parameters are varied one at a time in order to determine the dependence of Langmuir wave dynamics on the parameters.

We first present the simulation results for the following parameters: $k_c/k_0 = 0.67$, $\Delta k_c/k_c = 0.1$, $T_i/T_e = 0.5$, and $E_{max} = 100$ mV/m. We also include a
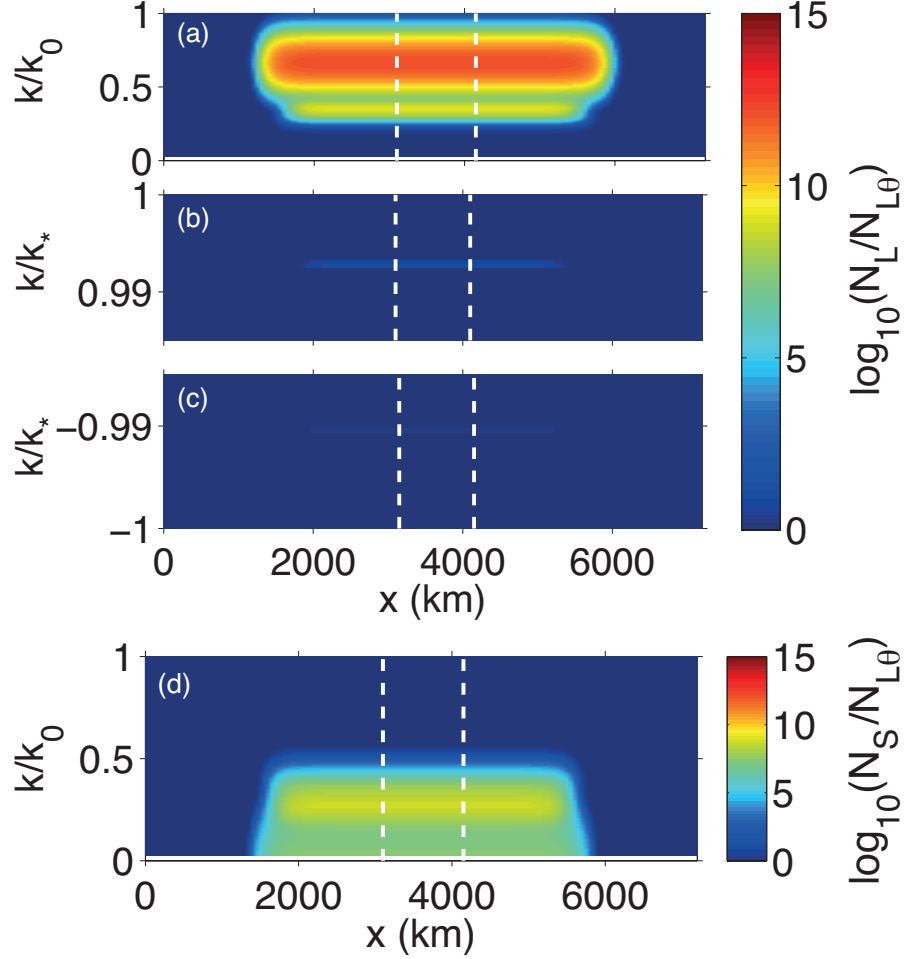
Figure 5.2: (a)-(c) $N_L(x,k)/N_{L\theta}$ and (d) $N_S(x,k)/N_{L\theta}$, at $t = 0.1\,\mathrm{s}$ for the default set of parameters, where $N_{L\theta}$ is the thermal level of Langmuir waves.

density well with left and right boundaries at $x = 3600 \pm 500\,\mathrm{km}$ such that the width of the well is $1000\,\mathrm{km}$.

The Langmuir and ion sound wave spectra at $t = t_0 = 0.1\,\mathrm{s}$ are shown in Fig. 5.2. The Langmuir wave source centered at $k_c = 0.67k_0$ has begun to decay to $k_{L'} = k_0 - k_L = 0.33k_0$, generating ion sound waves centered at $k_S = k_L - k_{L'} = 0.34k_0$. There is also the initial stage of decay from $k_L = 0.33k_0$ to $k_{L'} \approx \pm 0.995k_*$.

Spectra at $t = 0.2\,\mathrm{s}$ are shown in Fig. 5.3. The Langmuir wave source is almost entirely decayed from k_c to $k_{L'} = 0.33k_0$ and $k_{L'} \approx \pm 0.995k_*$. Ion sound waves from the first decay have $k_S = 0.34k_0$; their presence stimulates decay from $0.33k_0$ to $\pm k_*$ via the terms proportional to N_S in (5.9) and (5.11), since
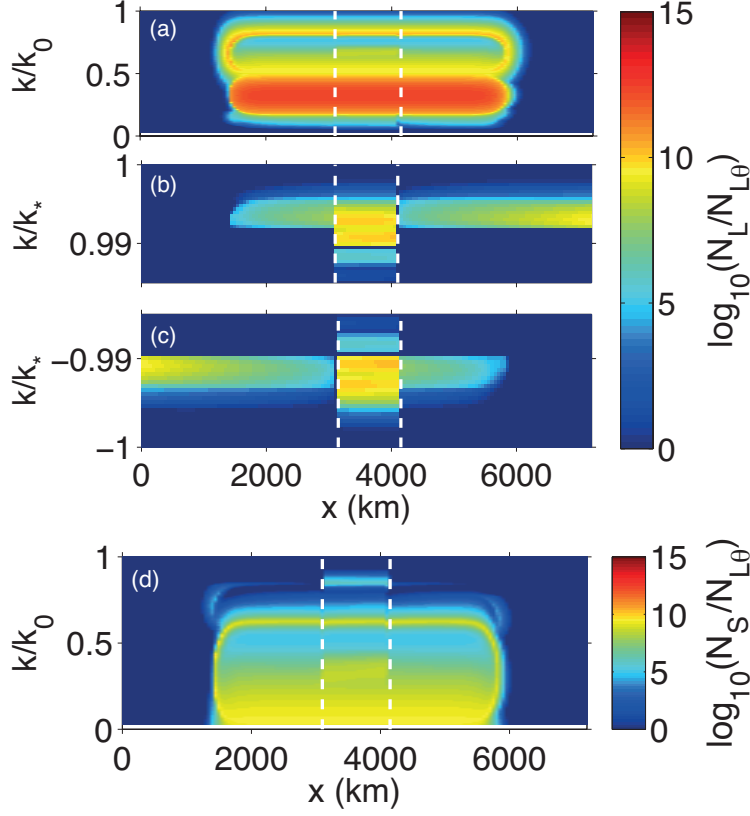
Figure 5.3: (a)-(c) $N_L(x,k)/N_{L\theta}$ and (d) $N_S(x,k)/N_{L\theta}$, at $t = 0.2$ s for the default set of parameters.

k_S is approximately equal to the difference in these wave numbers. Decay from k_c to $\pm k_*$ generates ion sound waves centered at $k_S = 0.67k_0 \mp 0.995k_* \sim 0.67k_0$, which can be seen in as a peak in N_S in Fig. 5.3(d). Low-k Langmuir waves generated outside the density well (and so are not trapped) have propagated to the edges of the simulation box. The lacunas in wave quanta near the boundaries of the reflecting boundaries are not physical but a result of the numerical implementation of reflection.

Figure 5.4 shows the spectra at the later time $t = 0.3$ s. The initial Langmuir wave source is now at approximately the thermal level, except at $\sim 0.67k_0$; this is due to coalescence of some $\pm k_*$ Langmuir waves with ion sound waves back to $k_L \approx 0.67k_0$. Outside the density well the level of Langmuir quanta at low k has decreased further as they propagate away from the source region.
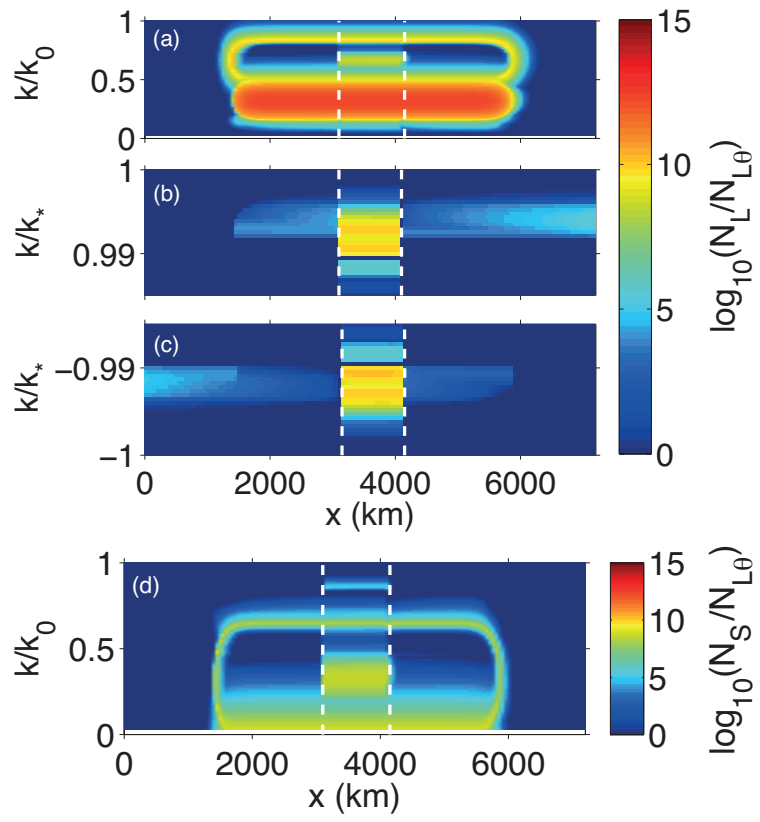
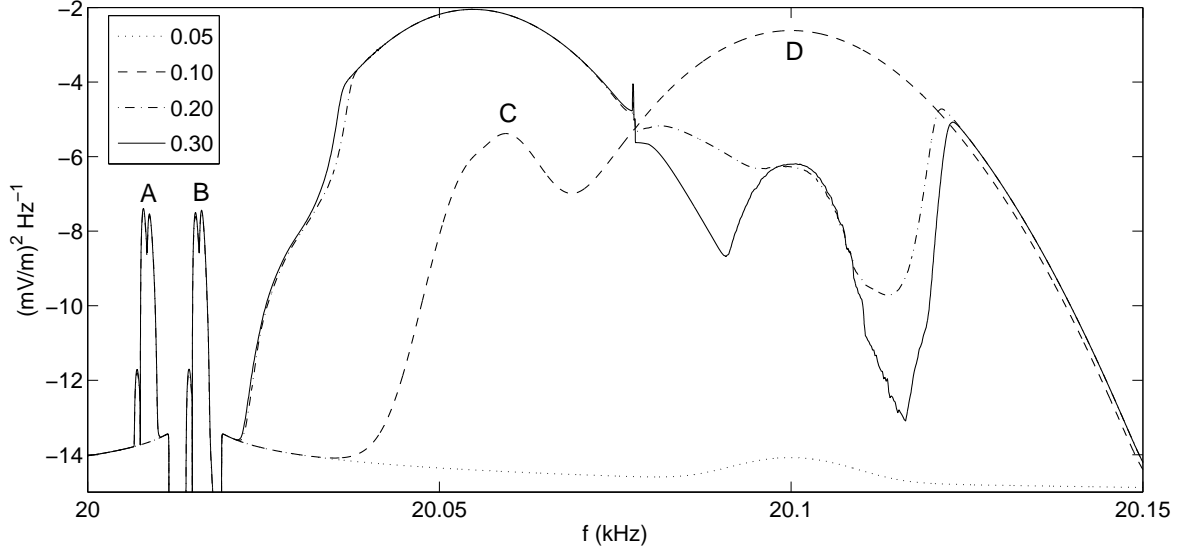Figure 5.4: (a)-(c) $N_L(x,k)/N_{L\theta}$ and (d) $N_S(x,k)/N_{L\theta}$, at $t = 0.3\,\mathrm{s}$ for the default set of parameters.

Figure 5.5: Langmuir wave power spectrum for the default set of parameters, at $x = 3600\,\text{km}$ and times $t = 0.05\,\text{s}$, $0.1\,\text{s}$, $0.2\,\text{s}$, and $0.3\,\text{s}$ as labeled. Points labeled A, B, C, and D correspond to $k_L = -k_*, k_*, 0.33k_0$, and $0.67k_0$ respectively.

A power spectrum for the Langmuir wave fields at $x = 3600\,\text{km}$ is shown in Fig. 5.5 at times $t = 0.05\,\text{s}$, $0.1\,\text{s}$, $0.2\,\text{s}$ and $0.3\,\text{s}$. The frequencies plotted here are for a spacecraft frame, which introduces a Doppler shift when transforming from the solar wind frame in which the simulations are performed. This Doppler shift is given by $\Delta\omega = \mathbf{k} \cdot \mathbf{v}_{sw}$, where $\mathbf{v}_{sw}$ is the relative velocity between the spacecraft frame and the solar wind frame. We take a nominal value of the solar wind at 1 AU of $v_{sw} = 400\,\text{km s}^{-1}$ and assume that Langmuir and ion sound waves have $\mathbf{k}||\mathbf{B}_0$ and thus $\mathbf{k}||\mathbf{v}_{sw}$. At $t = 0.05\,\text{s}$ the Langmuir waves are at approximately their thermal level, except at a small region around $f = 20.1\,\text{kHz}$ due to the Langmuir wave source. From $t = 0.1\,\text{s}$ through to $t = 0.3\,\text{s}$ we observe the further growth of Langmuir waves at k_c and the subsequent decay to $0.33k_0$ and $\pm k_*$ described above. Doppler shifting of the $\pm k_*$ waves (between A and B) is particularly noticeable; their frequencies are equal in the solar wind frame and differ only by virtue of the Doppler effect. The sharp peak at $t = 0.3\,\text{s}$ between C and D corresponds to $k = 0.5k_0$ and is not physical; it is due to the transition in the number of decay solutions from three for $k > 0.5k_0$ to two solutions $k < 0.5k_0$.
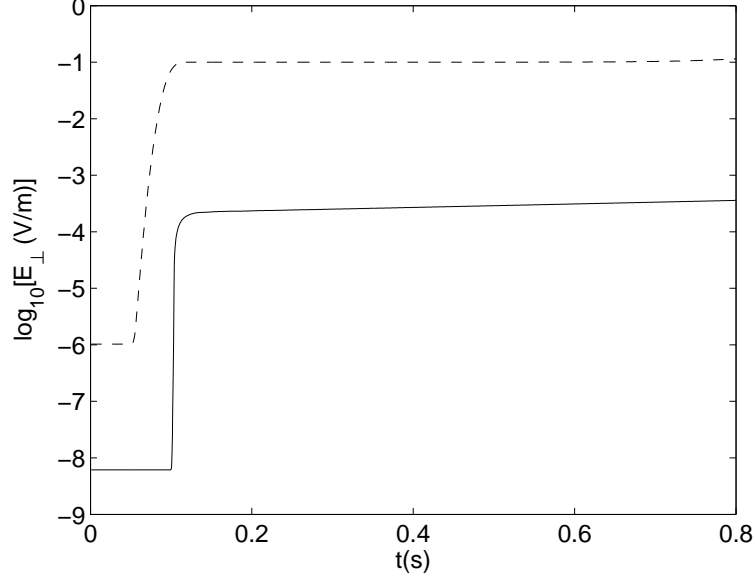
Figure 5.6: Time series of $E_\perp$ (solid line) and $E_{||}$ (dashed line) at $x = 3600\,\mathrm{km}$ for the default set of parameters.

The Langmuir wave electric fields can be calculated by integrating their occupation number over wave number, viz.

$$\frac{1}{2}\epsilon_0 E^2 = \int_{-\infty}^{\infty} \frac{dk}{2\pi} \hbar\omega_L(k) N_L(k). \qquad (5.21)$$

We separate this integral into $|k| \leq k_*$ and $|k| > k_*$ to obtain $E_\perp$ and $E_{||}$ respectively. The resulting time series of $E_\perp$ and $E_{||}$ are shown in Fig. 5.6. As t approaches t_0, $E_{||}$ reaches $E_{\max}$ and thereafter remains approximately constant. For $E_\perp$ there is a sharp increase at $t = t_0$ which is approximately exponential (since $\log_{10} E_\perp$ versus t is approximately linear). Recall that this phase of exponential growth is due to the decay of Langmuir waves at $0.33k_0$ to $\pm k_*$ stimulated by ion sound waves. This is followed by a second phase of exponential growth with a smaller growth rate. The growth rate is smaller because the Langmuir wave source is almost completely decayed; its further decay does not produce the significant levels of ion sound waves that stimulated decay to $\pm k_*$ in the first phase.
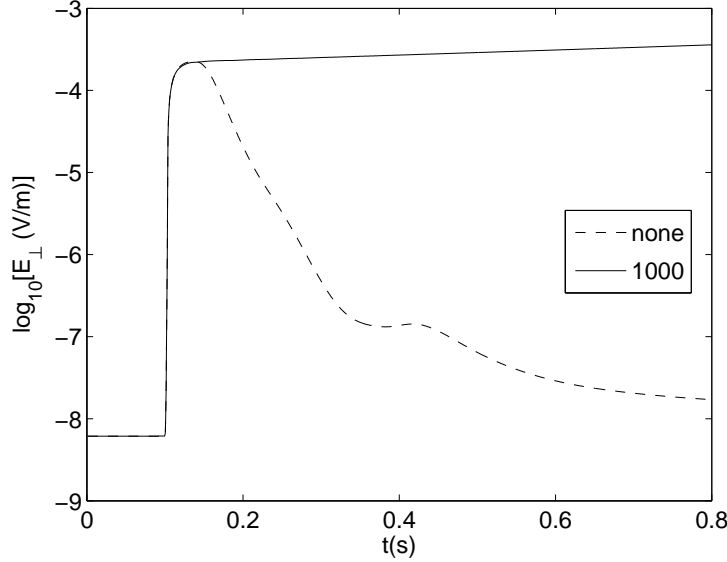
Figure 5.7: Time series of $E_\perp$ at $x = 3600\,\mathrm{km}$ with a density well of width $1000\,\mathrm{km}$ (solid line) and without a density well (dashed line).

5.4.1 Dependence on density well parameters

In this section we present the simulation results with and without trapping of Langmuir-z waves, as well as varying the width of the density well. Until $t = 0.12\,\mathrm{s}$ $E_\perp$ increases in the same manner with and without a density well, as shown in Fig. 5.7. Likewise, the spectra at $t = 0.2\,\mathrm{s}$ shown in Fig. 5.8 are qualitatively similar. However, after $t = 0.12\,\mathrm{s}$ the behavior is different in $E_\perp$; this is due to the low-k Langmuir waves propagating away from the source region, reducing $N_{L'}$ and diminishing the decay rate via the term $N_L N_{L'}$ in (5.9) and (5.11). The propagation of the k_* waves away from the center of the source region is clearly visible in Fig. 5.9.

We can also calculate a power spectrum for the situation in Figs 5.7–5.9. Figure 5.10 shows that Langmuir wave power near $20.02\,\mathrm{kHz}$ decreases, due to the reduction in waves near $\pm k_*$ due to propagation away from the center of the source region.

We now look at effect of increasing the width of the reflecting region. The time series of $E_\perp$ for density well widths of $1000\,\mathrm{km}$ (default), $4000\,\mathrm{km}$, and $6000\,\mathrm{km}$, as well as for no density well, are shown in Fig. 5.11. We observe an approximately exponential growth of $E_\perp$ fields again for $t \gtrsim t_0$ when the width of the well is 4000 or $6000\,\mathrm{km}$ but now with oscillatory behavior. This can be
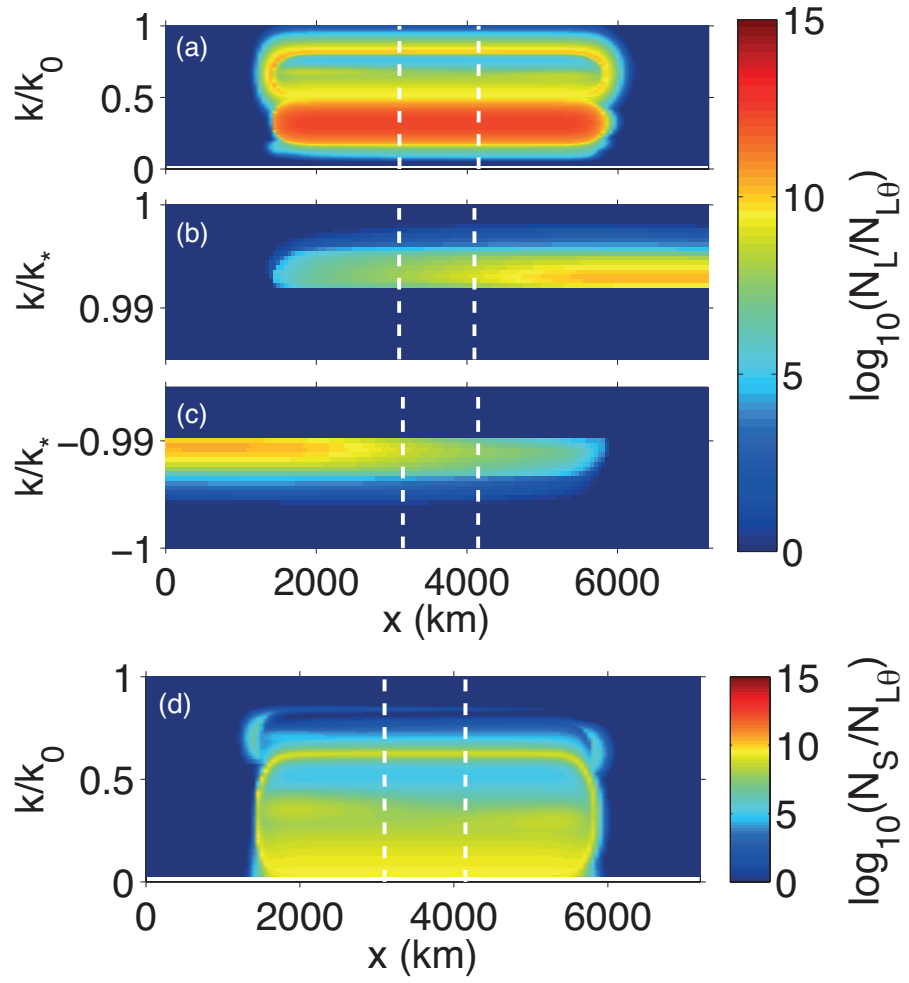
92

Figure 5.8: (a)-(c) $N_L(x,k)/N_{L\theta}$ and (d) $N_S(x,k)/N_{L\theta}$, at $t = 0.2\,\mathrm{s}$, without a density well.
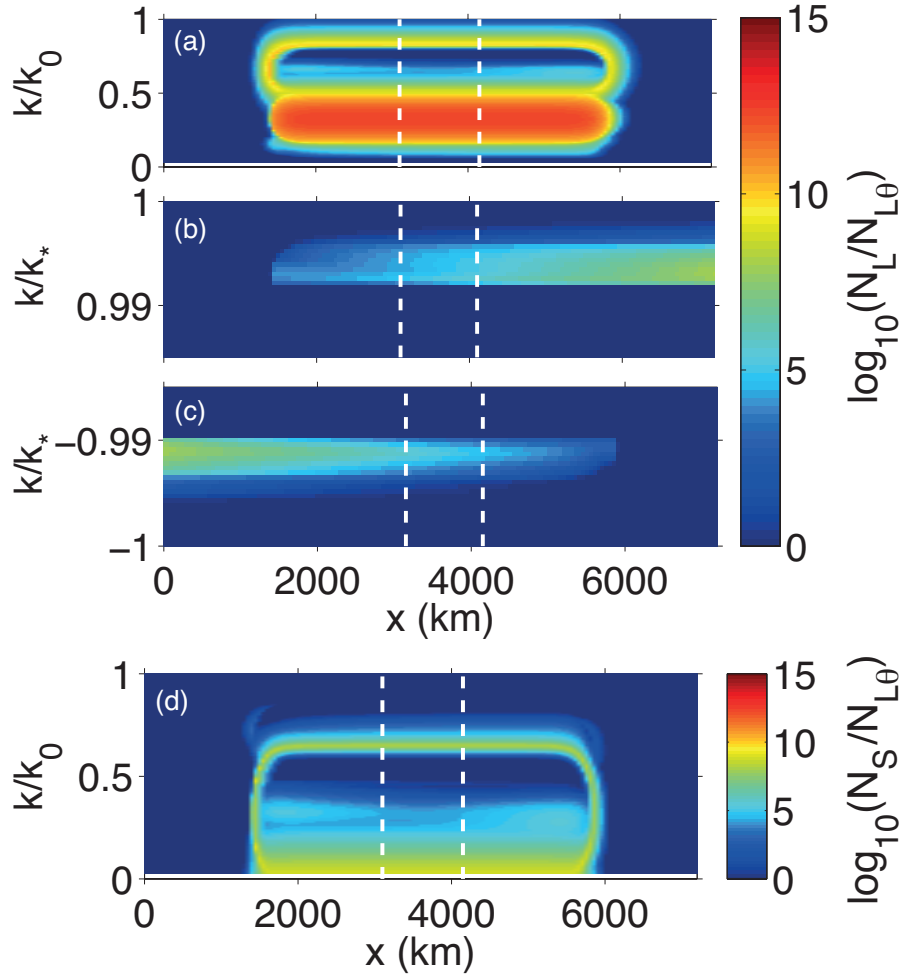
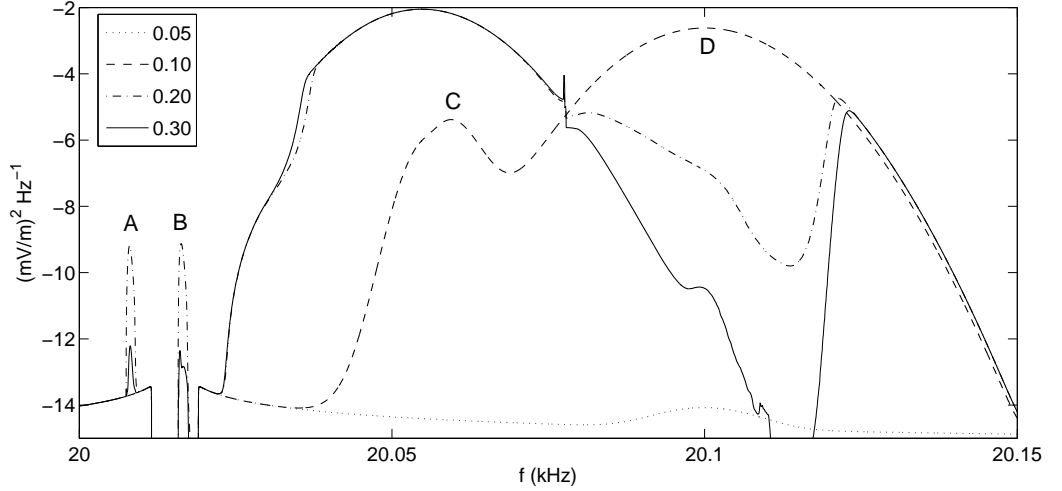Figure 5.9: (a)-(c) $N_L(x,k)/N_{L\theta}$ and (d) $N_S(x,k)/N_{L\theta}$, at $t = 0.3\,$s, without a density well.

Figure 5.10: Langmuir wave power spectrum for the case of no density well, at $x = 3600\,\text{km}$ and times $t = 0.05\,\text{s}$, $0.1\,\text{s}$, $0.2\,\text{s}$, and $0.3\,\text{s}$ as labeled. Points labeled A, B, C, and D correspond to $k_L = -k_*, k_*, 0.33k_0$, and $0.67k_0$ respectively.

understood as follows. In addition to the approximately exponential increase in low-k Langmuir waves, there is also a propagation of these generated waves towards the boundaries. When they reach the boundary they are reflected, changing the sign of k and so propagating in the opposite direction. When the peak of these waves reach $x = 3600\,\text{km}$ this causes an increase in $E_\perp$ (such as at $t \approx 0.25\,\text{s}$). As the peak passes through the center of the density well and reaches the boundaries, there is a local minimum in $E_\perp(t)$.

This oscillatory behavior has a period which is given by

$$t_{\text{bounce}} = L/v_g(k_*). \tag{5.22}$$

We calculate this for $L = 6000\,\text{km}$, using $v_g(k_*) = 28V_e$ (from Fig. 5.1), to give $t_{\text{bounce}} = 0.133\,\text{s}$. This agrees with the difference between times of consecutive local minima, which equals $0.13\,\text{s}$.

The rapid increase in $E_\perp$ near t_0, with a timescale much shorter than that of Langmuir wave propagation, is important in producing this oscillatory behavior; there would be no discernible oscillation if t_{bounce} and the growth rate were comparable.
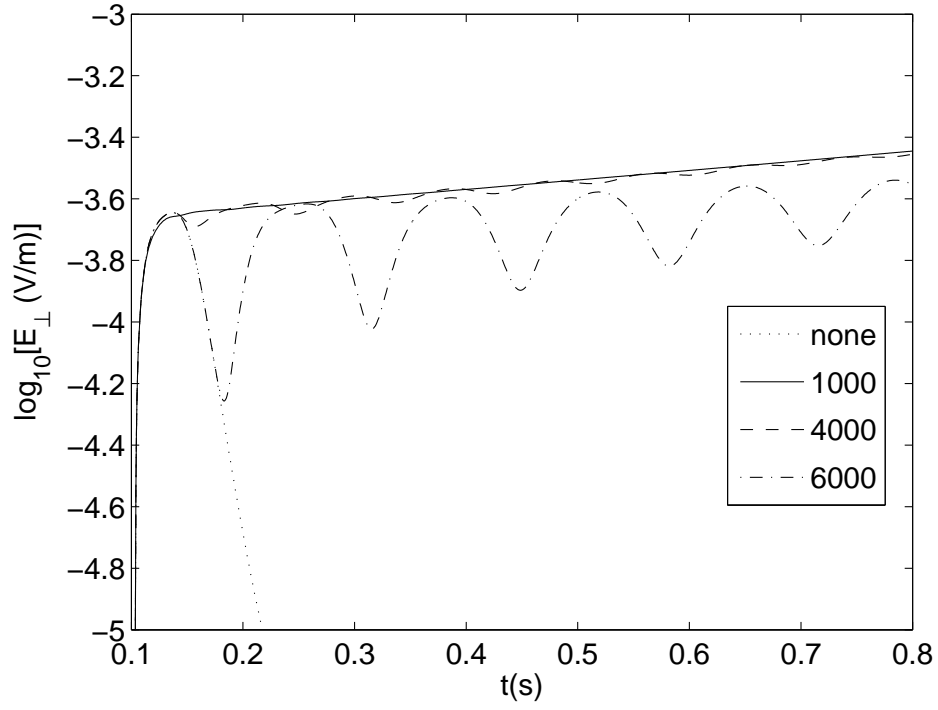
95

Figure 5.11: Time series of $E_\perp$ at $x = 3600\,\text{km}$ with and without a density well of varying width, as labeled in the legend in km.
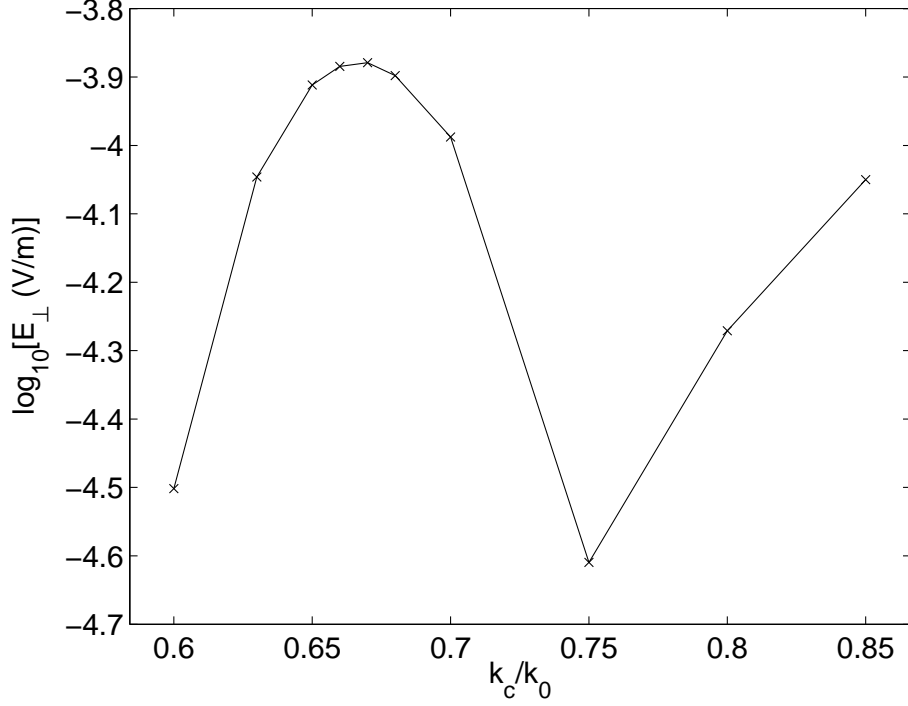
Figure 5.12: $E_\perp$ at $t = 1.1\,\text{s}$ and $x = 3600\,\text{km}$ versus k_c.

5.4.2 Dependence on k_c

To examine the growth rates of $E_\perp$ versus k_c, we examine the $E_\perp$ levels at a time shortly after the source term S reaches its maximum, which we take to be $t = 0.11\,\text{s}$. Figure 5.12 shows that there are two peaks, the first at $k_c/k_0 = 0.67$ and the second where k_c is increasing towards k_0. The first peak can be explained as follows. Decay of Langmuir waves from k_c to $k_0 - k_c$ produces ion sound waves at $2k_c - k_0$. These ion sound waves can stimulate decay of Langmuir waves from $k_0 - k_c$ to $\pm k_*$ if the difference in wave number between $k_0 - k_c$ and $\pm k_*$ equals $2k_c - k_0$, i.e., when $k_L \approx 2k_0/3$. If k_c is smaller or larger than $2k_0/3$ then ion sound waves still stimulate the decay due to the nonzero width of the initial distribution, but will not be as efficient. The second peak is due to the initial distribution becoming closer to k_0. Langmuir waves can then decay from $k_0 - k_*$ to k_*, rather than reaching k_* via two decays as for when $k_c \approx 0.67k_0$.

5.4.3   Dependence on $\Delta k_c/k_c$

The dependence of $E_\perp$ as a function of $\Delta k_c/k_c$ is now explored. Fig. 5.13 shows the time series of $E_\perp$ for $\Delta k_c/k_c = 0.05, 0.10, 0.15, 0.20$. The growth rate of $E_\perp$ is larger for smaller $\Delta k_c/k_c$, with the largest rate found for $\Delta k_c/k_c = 0.05$. There are two effects that can be important. Firstly, the decay rate is proportional to N_L, so larger $\Delta k_c/k_c$ for given $E_{\max}$ gives smaller N_L and thus a smaller rate. Secondly, if the waves have k_c further from where the growth of $E_\perp$ is maximum, a greater $\Delta k_c/k_c$ can give an initial distribution with more waves near $0.670 k_0$, increasing the rate. However, since we have chosen $k_c = 0.67 k_0$ for our default set of parameters, the latter effect is not important here.

5.4.4   Dependence on T_i/T_e

We also look at the dependence of the growth rate on T_i/T_e. First, we define the quantity

$$\Gamma = \frac{d}{dt} \log_{10}[E_\perp(\text{V/m})], \qquad (5.23)$$

which reduces to the exponential growth rate of $E_\perp$ when $\log_{10}[E_\perp(\text{V/m})]$ is a linear function of time. Figure 5.14 displays Γ as a function of T_i/T_e at $t = 0.8\,\text{s}$. It can be seen that Γ increases linearly with T_i/T_e. This is due to the factor G in the nonlinear decay rate, which is proportional to $1 + 3T_i/T_e$ [cf. Eq. (5.12)].

5.4.5   Dependence on $E_{\max}$

Finally, we plot the dependence of the nonlinear rate Γ on $E_{\max}$ at $t = 0.8\,\text{s}$ in Fig. 5.15. We perform a linear fit on $\log_{10}\Gamma$ versus $\log_{10}E_{\max}$ and find a slope of 1.998 ± 0.057, consistent with $\Gamma \sim E_{\max}^2$. This can be explained as follows. After the initial increase in $E_\perp$ stimulated by ion sound waves, the growth of waves near k_* is due to terms of the form $N_L N_{L'}$. Thus,

$$\frac{dN_{L'}}{dt} \propto N_L N_{L'} \propto E_{\max}^2 N_{L'}, \qquad (5.24)$$

where we have used (5.21) in the second proportionality. Equation (5.24) can be solved to give

$$N_{L'}(t) = N_{L'}(0)e^{\Gamma t}, \qquad (5.25)$$

and thus the rate of increase of $E_\perp$ also has the form of an exponential increase with growth rate $\Gamma \propto E_{\max}^2$.
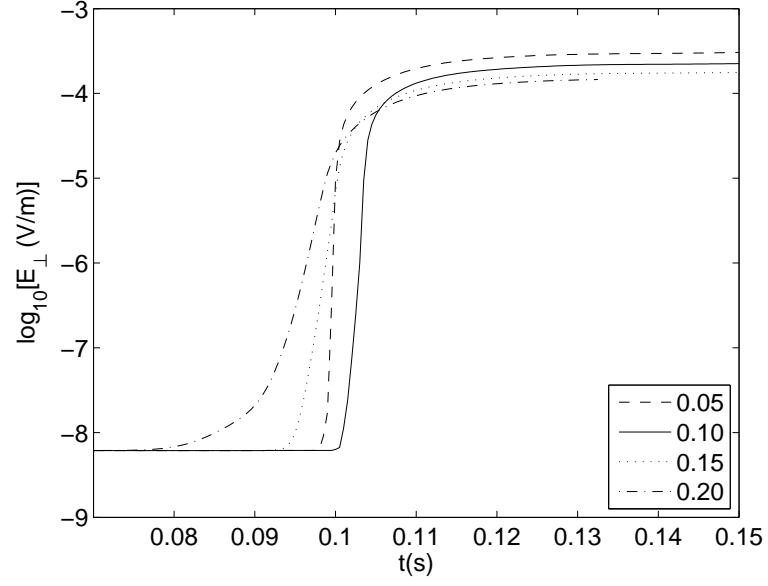
Figure 5.13: $E_\perp$ versus t for different values of $\Delta k_c/k_c$ (labeled in the legend).
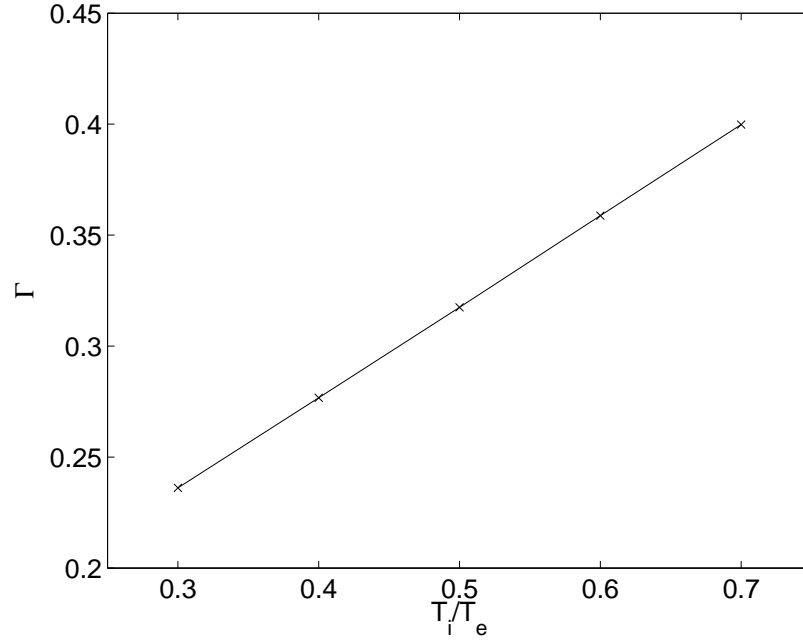

Figure 5.14: Γ as a function of T_i/T_e at $t = 0.8\,\mathrm{s}$.
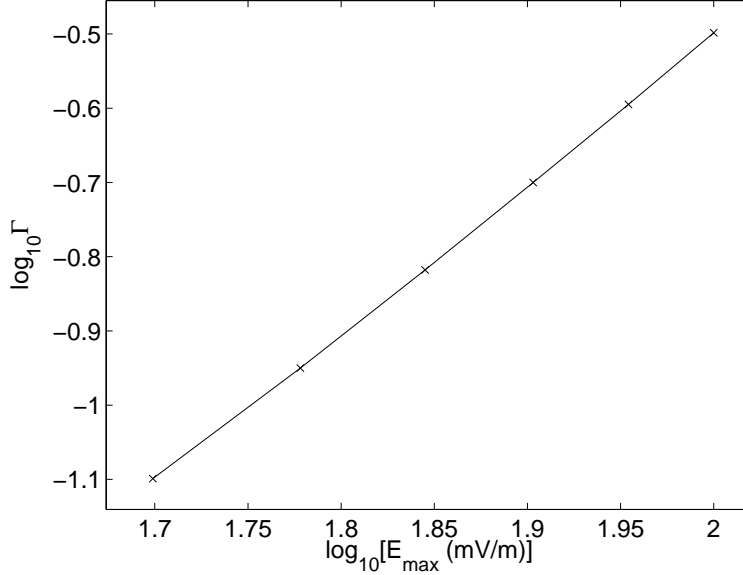
Figure 5.15: $\log_{10} \Gamma$ versus $\log_{10} E_{\max}$ at $x = 3600\,\text{km}$ and $t = 0.8\,\text{s}$.

5.5   Discussion and Conclusion

In this chapter we have performed quasilinear simulations of Langmuir wave growth in magnetized plasmas for typical solar wind parameters. Perpendicular electric fields from low-k Langmuir-z waves undergo two phases of exponential growth. The first phase has a very large growth rate, with $E_\perp$ increasing from $10^{-8}\,\text{V/m}$ to $10^{-4}\,\text{V/m}$ in $\sim 0.01\,\text{s}$. Decay of the initial Langmuir source at k_c to $k_0 - k_c$ produces ion sound waves that stimulate further decays from $k_0 - k_c$ to $\sim \pm k_*$. The second phase has a slower growth rate and is not significantly stimulated by ion sound waves. In both phases the growth rates are dependent on the various plasma parameters. Larger T_i/T_e and $E_{\max}$ and smaller $\Delta k_c/k_c$ are found to increase the growth rate of $E_\perp$. However, the optimal beam wave number for the growth of $E_\perp$ is peaked at $0.67k_0$ or else near k_0. We predict that the parameters which yield a larger growth rate also give rise to a greater observed $E_\perp$ at longer timescales.

Chapter 6

Concluding remarks and future directions

In this thesis the effect of magnetization on various mode conversion processes has been investigated. In Chapter 2 we investigated mode conversion phenomena proposed by previous authors for auroral waves above and below the local plasma frequency, which were interpreted as electromagnetic z-mode and whistler-mode waves, respectively. We argued that these observations must be understood in terms of the wave modes of magnetized kinetic plasmas, namely the combined Langmuir-z and Langmuir-whistler modes, which have the characteristics of the thermal Langmuir mode at high k and either z-mode or whistler-mode characteristics at low k. As these waves propagate in the inhomogeneous ionosphere, they remain on the Langmuir-z or Langmuir-whistler mode but move to lower k where the mode properties are different, so that no mode conversion process is necessary.

In Chapter 3 we investigated the effect of magnetization on the electrostatic decay of Langmuir waves parallel to the background magnetic field in a weakly magnetized plasma. For primary Langmuir wave numbers less than approximately k_0, the kinematics of the decay process are fundamentally different. Namely, there exist solutions with very low $k_{L'}$ which are on the z-mode portion of the Langmuir-z mode and thus are polarized predominantly perpendicular to the background magnetic field. Quasilinear simulations including these magnetization effects showed significant energy transfer to these wave numbers under certain plasma conditions, thus demonstrating the importance of magnetization effects. These results have applications to recent observations by STEREO spacecraft of large transverse electric fields of Langmuir waves in the solar wind at 1 AU, which we suggest are the result of electrostatic decay to low wave numbers.

In Chapter 4 we extended the calculation of kinematics to two dimensions and to weakly and strongly magnetized plasmas. We confirmed that the low wave number solutions for decay discussed in Chapter 3 persist for arbitrary propagation angles of primary Langmuir-z waves with respect to the background magnetic field. This includes perpendicular propagation, where the primary wave is in the upper hybrid mode. We find that decay kinematics at oblique angles in a magnetized plasma are not well approximated by unmagnetized kinematics for $k_L \lesssim k_0$, demonstrating the importance of including magnetization effects in the analysis of decay.

For a strongly magnetized plasma, where the relevant wave mode is the Langmuir-whistler mode, the kinematics in 1D are very similar to those of a weakly magnetized plasma. However, in 2D the solutions are seen to be very different, with decay products confined to a narrow range of angles about the primary wave vector. Also, the wave numbers of the daughter Langmuir waves are found to be larger than those of the primary Langmuir waves, due to the different topology of the Langmuir-whistler mode surface compared with the Langmuir-z mode.

In Chapter 5 we performed further quasilinear simulations of electrostatic decay in a weakly magnetized plasma, focusing on the growth rates of the perpendicular fields of Langmuir waves as a function of the various plasma parameters. It was found that the beam wave number at which the growth of perpendicular wave fields is fastest is $k_b = 0.67k_0$; ion sound waves that are generated by the first decay for this value of k_b possess the optimal wave numbers for stimulation of the decay to $\pm k_*$.

Some possibilities for future work are now discussed. A natural extension to our analysis of the electrostatic decay process $L \rightarrow L' + S$ in magnetized plasmas would be to other three-wave processes that are important in type II and III solar radio bursts, such as electromagnetic decay $L \rightarrow T \pm S$ and the coalescence process $L + L' \rightarrow T$ (where the transverse wave modes T are either the o or x mode). Including these in our quasilinear simulations would allow prediction of the various properties of radio bursts, such their frequency variation with time and the power radiated in the fundamental and harmonic bands, as well as their o/x polarization.

Bibliography

André, M. (1985), Dispersion surfaces, *J. Plasma Phys.*, *33*, 1.

Appleton, E. V. (1932), Wireless studies of the ionosphere, *J. Inst. Elec. Engrs.*, *71*, 642.

Arnoldy, R. L., K. A. Lynch, J. B. Austin, and P. M. Kintner (1999), Energy and pitch angle-dispersed auroral electrons suggesting a time-variable, inverted-V potential structure, *J. Geophys. Res.*, *104*, 22,613.

Åström, E. (1950), Magneto-hydrodynamic waves in a plasma, *Nature*, *165*, 1019.

Bale, S. D., P. J. Kellogg, K. Goetz, and S. J. Monson (1998), Transverse zmode waves in the terrestrial electron foreshock, *Geophys. Res. Lett.*, *25*, 9.

Beghin, C., J. L. Rauch, and J. M. Bosqued (1989), Electrostatic plasma waves and HF auroral hiss generated at low altitude, *J. Geophys. Res.*, *94*, 1359.

Bell, T. F., and H. D. Ngo (1988), Electrostatic waves stimulated by coherent vlf signals propagating in and near the inner radiation belt, *J. Geophys. Res.*, *93*, 2599.

Bell, T. F., and H. D. Ngo (1990), Electrostatic lower hybrid waves excited by electromagnetic whistler mode waves scattering from planar magnetic-field-aligned plasma density irregularities, *J. Geophys. Res.*, *95*, 149.

Benford, G., D. Tzach, K. Kato, and D. F. Smith (1980), Collective microwave emission from intense elecron-beam interactions: Theory and experiment, *Phys. Rev. Lett.*, *45*, 1182.

Bernstein, I. B. (1958), Waves in a plasma in a magnetic field, *Phys. Rev*, *109*, 10.

Bohm, D., and E. P. Gross (1949), Theory of plasma oscillations. A. Origin of medium-like behavior, *Phys. Rev.*, *75*, 1851.

Bougeret, J., K. Goetz, M. Kaiser, S. Bale, P. Kellogg, M. Maksimovic, N. Monge, S. Monson, P. Astier, S. Davy, M. Dekkali, J. Hinze, R. Manning, E. Aguilar-Rodriguez, X. Bonnin, C. Briand, I. Cairns, C. Cattell, B. Cecconi, J. Eastwood, R. Ergun, J. Fainberg, S. Hoang, K. Huttunen, S. Krucker, A. Lecacheux, R. MacDowall, W. Macher, A. Mangeney, C. Meetre, X. Moussas, Q. Nguyen, T. Oswald, M. Pulupa, M. Reiner, P. Robinson, H. Rucker, C. Salem, O. Santolik, J. Silvis, R. Ullrich, P. Zarka, and I. Zouganelis (2008), S/WAVES: The radio and plasma wave investigation on the STEREO mission, *Space Sci. Rev.*, *136*, 487.

Budden, K. G. (1961), *Radio Waves in the Ionosphere*, Cambridge Univ. Press, Cambridge.

Budden, K. G. (1985), *The Propagation of Radio Waves*, Cambridge Univ. Press, Cambridge.

Budden, K. G., and D. Jones (1986), Full wave calculations of radio windows and their relevance to the theory of production of planetary nonthermal continuum radiation, in *Comparative study of magnetospheric systems*, vol. 1, p. 563.

Cairns, I. H. (1987a), Second harmonic plasma emission involving ion sound waves, *J. Plasma Phys.*, *38*, 179.

Cairns, I. H. (1987b), Fundamental plasma emission involving ion sound waves, *J. Plasma Phys.*, *38*, 169.

Cairns, I. H. (1995), Detectability of electrostatic decay products in Ulysses and Galileo observations of type III solar radio sources, *Astrophys. J. Lett.*, *449*, L95.

Cairns, I. H. (2000), Role of collective effects in dominance of scattering off thermal ions over Langmuir wave decay: Analysis, simulations, and space applications, *Phys. Plasmas*, *7*, 4901.

Cairns, I. H., and P. A. Robinson (1992), Theory for low-frequency modulated Langmuir wave packets, *Geophys. Res. Lett.*, *19*, 2187.

Cairns, I. H., and P. A. Robinson (1995a), Ion acoustic wave frequencies and onset times during type III solar radio bursts, *Astrophys. J.*, *453*, 959.

Cairns, I. H., and P. A. Robinson (1995b), Inconsistency of Ulysses millisecond Langmuir spikes with wave collapse in type III radio sources, *Geophys. Res. Lett.*, *22*, 3437.

Cairns, I. H., and P. A. Robinson (1997), First test of stochastic growth theory for Langmuir waves in Earth's foreshock, *Geophys. Res. Lett.*, *24*, 369.

Cairns, I. H., and P. A. Robinson (1998), Constraints on nonlinear and stochastic growth theories for type III solar radio bursts from the corona to 1 AU, *Astrophys. J.*, *509*, 471.

Cairns, I. H., and P. A. Robinson (1999), Strong evidence for stochastic growth of Langmuir-like waves in Earth's foreshock, *Phys. Rev. Lett.*, *82*, 3066.

Cairns, I. H., P. A. Robinson, and N. I. Smith (1998), Arguments against modulational instabilities of Langmuir waves in Earth's foreshock, *J. Geophys. Res.*, *103*, 287.

Cairns, I. H., P. A. Robinson, and G. P. Zank (2000a), Progress on coronal, interplanetary, foreshock, and outer heliospheric radio emissions, *Publ. Astron. Soc. Aust.*, *17*, 22.

Cairns, I. H., P. A. Robinson, and R. R. Anderson (2000b), Thermal and driven stochastic growth of Langmuir waves in the solar wind and Earth's foreshock, *Geophys. Res. Lett.*, *27*, 61.

Chaston, C. C., C. W. Carlson, W. J. Peria, R. E. Ergun, and J. P. McFadden (1999), FAST observations of inertial Alfven waves in the dayside aurora, *Geophys. Res. Lett.*, *26*, 647.

Chen, F. F. (1974), *Introduction to Plasma Physics*, Plenum Press, New York.

Cheung, P. Y., A. Y. Wong, C. B. Darrow, and S. J. Qian (1982), Simultaneous observation of caviton formation, spiky turbulence, and electromagnetic radiation, *Phys. Rev. Lett.*, *48*, 1348.

Davidson, R. C. (1972), *Methods in nonlinear plasma theory*, Academic Press, New York.

Drummond, W. E., and D. Pines (1962), Non-linear stability of plasma oscillations, *Nucl. Fusion Suppl. Part 3*, p. 1049.

Ellis, G. R. A. (1956), The Z propagation hole in the ionosphere, *J. Atmos. Terr. Phys.*, *8*, 243.

Ergun, R. E., D. Larson, R. P. Lin, J. P. McFadden, C. W. C. K. A. Anderson, L. Muschietti, M. McCarthy, G. K. Parks, H. Reme, J. M. Bosqued, C. D'Uston, T. R. Sanderson, K. P. Wenzel, M. Kaiser, R. P. Lepping, S. D. Bale, P. J. Kellogg, and J.-L. Bougeret (1998), Wind spacecraft observations of solar impulsive electron events associated with solar type III radio bursts, *Astrophys. J.*, *503*, 435.

Ergun, R. E., D. M. Malaspina, I. H. Cairns, M. V. Goldman, D. L. Newman, P. A. Robinson, S. Eriksson, J.-L. Bougeret, C. Briand, S. D. Bale, C. A. Cattell, P. J. Kellogg, and M. L. Kaiser (2008), Eigenmode structure in solar-wind Langmuir waves, *Phys. Rev. Lett.*, *101*, 051,101.

Field, G. B. (1956), Radiation by plasma oscillations, *Astrophys. J.*, *124*, 555.

Gary, S. P. (1985), Electromagnetic electron beam instabilities: Hot, isotropic beams, *J. Geophys. Res.*, *90*, 10,815.

Ginzburg, V. L., and V. V. Zhelezniakov (1958), On the possible mechanisms of sporadic solar radio emission (radiation in an isotropic plasma), *Astron. Zh.*, *2*, 694.

Graham, D. B., and I. H. Cairns (2013a), Constraints on the formation and structure of Langmuir eigenmodes in the solar wind, *Phys. Rev. Lett.*, *111*, 121,101.

Graham, D. B., and I. H. Cairns (2013b), Electrostatic decay of Langmuir/z-mode waves in type III solar radio bursts, *J. Geophys. Res.*, *118*, 3968.

Graham, D. B., O. Skjaeraasen, P. A. Robinson, and I. H. Cairns (2011), Three-dimensional electromagnetic strong turbulence. I. Scalings, spectra, and field statistics, *Phys. Plasmas*, *18*, 62,301.

Graham, D. B., I. H. Cairns, D. R. Prabhakar, R. E. Ergun, D. M. Malaspina, S. D. Bale, K. Goetz, and P. J. Kellogg (2012a), Do Langmuir wave packets in the solar wind collapse?, *J. Geophys. Res.*, *117*, A09,107.

Graham, D. B., I. H. Cairns, D. M. Malaspina, and R. E. Ergun (2012b), Evidence against the oscillating two-stream instability and spatial collapse of Langmuir waves in solar type III radio bursts, *Astrophys. J. Lett.*, *753*, L18.

Grognard, R. J.-M. (1975), Deficiencies of the asymptotic solutions commonly found in the quasilinear relaxation theory, *Aust. J. Phys.*, *28*, 731.

Gurnett, D. A. (1966), A satellite study of VLF hiss, *J. Geophys. Res.*, *71*, 5599.

Gurnett, D. A. (1974), The Earth as a radio source: Terrestrial kilometric radiation, *J. Geophys. Res.*, *79*, 4227.

Gurnett, D. A., and R. R. Anderson (1976), Electron plasma oscillations associated with type III radio bursts, *Science*, *194*, 1159.

Gurnett, D. A., S. D. Shawhan, and R. R. Shaw (1983), Auroral hiss, Z mode radiation, and auroral kilometric radiation in the polar magnetosphere: DE 1 observations, *J. Geophys. Res.*, *88*, 329.

Hartree, D. R. (1931), The propagation of electromagnetic waves in a refracting medium in a magnetic field, *Proc. Camb. Phil. Soc.*, *27*, 143.

Hellberg, M. A., and R. L. Mace (2002), Generalized plasma dispersion function for a plasma with a kappa-Maxwellian velocity distribution, *Phys. Plasmas*, *9*, 1495.

Henri, P., C. Briand, A. Mangeney, S. D. Bale, F. Califano, K. Goetz, and M. Kaiser (2009), Evidence for wave coupling in type III emissions, *J. Geophys. Res.*, *114*, A03,103.

Henri, P., F. Califano, C. Briand, and A. Mangeney (2010), Vlasov simulations of Langmuir electrostatic decay and consequences for type III observations, *AIP Conference Proceedings*, *1216*(1), 288.

Henri, P., F. Califano, C. Briand, and A. Mangeney (2011), Low-energy Langmuir cavitons: Asymptotic limit of weak turbulence, *Europhys. Lett.*, *96*, 55,004.

Hess, S. L. G., D. M. Malaspina, and R. E. Ergun (2010), Growth of the Langmuir cavity eigenmodes in the solar wind, *J. Geophys. Res.*, *115*, A10,103.

Hinkel-Lipsker, D. E., B. D. Fried, and G. J. Morales (1992), Analytic expressions for mode conversion in a plasma with a linear density profile, *Phys. Fluids B*, *4*, 559.

James, H. G. (1976), VLF saucers, *J. Geophys. Res.*, *81*, 501.

Jones, D. (1976a), Source of terrestrial non-thermal radiation, *Nature*, *260*, 686.

Jones, D. (1976b), The second Z-propagation window, *Nature*, *262*, 674.

Kim, E. H., I. H. Cairns, and P. A. Robinson (2007), Extraordinary-mode radiation produced by linear-mode conversion of Langmuir waves, *Phys. Rev. Lett.*, *99*, 15,003.

Kim, E. H., I. H. Cairns, and P. A. Robinson (2008), Mode conversion of Langmuir to electromagnetic waves at magnetic field-aligned density inhomogeneities: Simulations, theory, and applications to the solar wind and the corona, *Phys. Plasmas*, *15*, 102,110.

Kintner, P. M., J. Vago, S. Chesney, R. L. Arnoldy, K. A. Lynch, C. J. Pollock, and T. E. Moore (1992), Localized lower hybrid acceleration of ionospheric plasma, *Phys. Rev. Lett.*, *68*, 2448.

Knock, S. A., I. H. Cairns, P. A. Robinson, and Z. Kuncic (2001), Theory of type II radio emission from the foreshock of an interplanetary shock, *J. Geophys. Res.*, *106*, 25,041.

Kurth, W. S., D. A. Gurnett, F. L. Scarf, and R. L. Poynter (1984), Detection of a radio emission at 3 kHz in the outer heliosphere, *Nature*, *312*, 27.

LaBelle, J., and A. T. Weatherwax (2002), Statistical study of auroral roar emissions at South Pole Station, *J. Geophys. Res.*, *107*, A000,167.

LaBelle, J., M. L. Trimpi, R. Brittain, and A. T. Weatherwax (1995), Fine structure of auroral roar emissions, *J. Geophys. Res.*, *100*, 21,953.

LaBelle, J., I. H. Cairns, and C. A. Kletzing (2010), Electric field statistics and modulation characteristics of bursty Langmuir waves observed in the cusp, *J. Geophys. Res.*, *115*, A10,317.

Landau, L. D. (1946), On the vibrations of the electronic plasma, *J. Phys. USSR*, *10*, 25.

Layden, A., I. H. Cairns, P. A. Robinson, and J. LaBelle (2011), Changes in mode properties versus mode conversion for waves in Earth's auroral ionosphere, *J. Geophys. Res.*, *116*, 12,328.

Layden, A., I. H. Cairns, B. Li, and P. A. Robinson (2013), Electrostatic decay in a weakly magnetized plasma, *Phys. Rev. Lett.*, *110*, 185,001.

Leblanc, Y., D. Jones, and H. O. Rucker (1986), Jovian 1.2-kHz nonthermal continuum radiation, *J. Geophys. Res.*, *91*, 9995.

Li, B., P. A. Robinson, and I. H. Cairns (2002), Multiple electron beam propagation and Langmuir wave generation in plasmas, *Phys. Plasmas*, *9*, 2976.

Li, B., A. J. Willes, P. A. Robinson, and I. H. Cairns (2003), Dynamics of beam-driven Langmuir and ion-acoustic waves including electrostatic decay, *Phys. Plasmas*, *10*, 2748.

Li, B., I. H. Cairns, and P. A. Robinson (2008), Simulations of coronal type III solar radio bursts: 1. Simulation model, *J. Geophys. Res.*, *113*, 6104.

Lin, R. P., W. K. Levedahl, W. Lotko, D. A. Gurnett, and F. L. Scarf (1986), Evidence for nonlinear wave-wave interactions in solar type III radio bursts, *Astrophys. J.*, *308*, 954.

Malaspina, D. M., and R. E. Ergun (2008), Observations of three-dimensional Langmuir wave structure, *J. Geophys. Res.*, *113*, A12,108.

Malaspina, D. M., I. H. Cairns, and R. E. Ergun (2010), The 2fp radiation from localized Langmuir waves, *J. Geophys. Res.*, *115*, 1101.

Malaspina, D. M., I. H. Cairns, and R. E. Ergun (2011), Dependence of Langmuir wave polarization on electron beam speed in type III solar radio bursts, *Geophys. Res. Lett.*, *38*, 13,101.

Malaspina, D. M., I. H. Cairns, and R. E. Ergun (2012), Antenna radiation near the local plasma frequency by Langmuir wave eigenmodes, *Astrophys. J.*, *755*, 45.

McAdams, K. L., and J. LaBelle (1999), Narrowband structure in HF waves above the electron plasma frequency in the auroral ionosphere, *Geophys. Res. Lett.*, *26*, 1825.

McAdams, K. L., J. LaBelle, P. W. Schuck, and P. M. Kintner (1998), PHAZE II observations of lower hybrid burst structures occurring on density gradients, *Geophys. Res. Lett.*, *25*, 3091.

McAdams, K. L., J. LaBelle, M. Trimpi, P. Kintner, and R. Arnoldy (1999), Rocket observations of banded structure in waves near the Langmuir frequency in the auroral ionosphere, *J. Geophys. Res.*, *104*, 28,109.

McAdams, K. L., R. E. Ergun, and J. LaBelle (2000), HF chirps: Eigenmode trapping in density depletions, *Geophys. Res. Lett.*, *27*, 321.

Melrose, D. B. (1976), Effects of an ambient magnetic field on the properties of Langmuir waves, *Sol. Phys.*, *46*, 511.

Melrose, D. B. (1980a), *Plasma Astrophysics volume II*, Gordon & Breach, New York.

Melrose, D. B. (1980b), The emission mechanisms for solar radio bursts, *Space Sci. Rev.*, *26*, 3.

Melrose, D. B. (1982), Fundamental emission for type III bursts in the interplanetary medium - The role of ion-sound turbulence, *Sol. Phys.*, *79*, 173.

Melrose, D. B. (1986a), *Instabilities in Space and Laboratory Plasmas*, Cambridge University Press, Cambridge.

Melrose, D. B. (1986b), *Reactive and resistive nonlinear instabilities*, vol. 36, 269 pp.

Muschietti, L., and C. T. Dum (1991), Nonlinear wave scattering and electron beam relaxation, *Phys. Fluids B*, *3*, 1968.

Nulsen, A. L., I. H. Cairns, and P. A. Robinson (2007), Field distributions and shapes of Langmuir wave packets observed by Ulysses in an interplanetary type III burst source region, *J. Geophys. Res.*, *112*, A05,107.

Oya, H. (1971), Conversion of electrostatic plasma waves into electromagnetic waves: Numerical calculation of the dispersion relation for all wavelengths, *Radio Sci.*, *6*, 1131.

Papadopoulos, K., M. L. Goldstein, and R. A. Smith (1974), Stabilization of electron streams in type III solar radio bursts, *Astrophys. J.*, *190*, 175.

Poeverlein, H. (1950), Strahlege von radiowellen in der ionosphare, *Z. Angew. Phys.*, *2*, 152.

Robinson, P. A. (1986), Electron cyclotron waves: Dispersion and accessibility conditions in isotropic and anisotropic plasmas, *J. Plasma Phys.*, *35*, 187.

Robinson, P. A. (1992), Clumpy Langmuir waves in type III radio sources, *Sol. Phys.*, *139*, 147.

Robinson, P. A. (1997), Nonlinear wave collapse and strong turbulence, *Rev. Mod. Phys.*, *69*, 507.

Robinson, P. A., D. L. Newman, and M. V. Goldman (1988), Three-dimensional strong Langmuir turbulence and wave collapse, *Phys. Rev. Lett.*, *61*, 702.

Robinson, P. A., A. J. Willes, and I. H. Cairns (1993a), Dynamics of Langmuir and ion-sound waves in type III solar radio sources, *Astrophys. J.*, *408*, 720.

Robinson, P. A., I. H. Cairns, and G. D. A. (1993b), Clumpy Langmuir waves in type III radio sources: Comparison of stochastic-growth theory with observations, *Astrophys. J.*, *407*, 790.

Rönnmark, K. (1982), Waves in homogeneous, anisotropic multicomponent plasmas (WHAMP), *KGI report*, Kiruna Geophysical Institute, Kiruna, Sweden.

Sagdeev, R. Z., and A. A. Galeev (1969), *Nonlinear Plasma Theory*, Benjamin, New York.

Samara, M., J. LaBelle, and I. H. Cairns (2008), Statistics of auroral Langmuir waves, *Ann. Geophys.*, *26*, 3885.

Santolík, O., F. Lefeuvre, M. Parrot, and J. L. Rauch (2001), Propagation of Z-mode and whistler-mode emissions observed by Interball 2 in the nightside auroral region, *J. Geophys. Res.*, *106*, 21,137.

Scarf, F. L., R. W. Fredricks, L. A. Frank, and M. Neugebauer (1971), Non-thermal electrons and highfrequency waves in the upstream solar wind, 1. Observations.

Sitenko, A. G. (1982), *Fluctuations and Non-linear Wave Interactions in Plasmas*, Pergamon, Oxford.

Stix, T. H. (1962), *The Theory of Plasma Waves*, McGraw-Hill, New York.

Stix, T. H. (1992), *Waves in plasmas*, American Institute of Physics, New York.

Sturrock, P. A. (1964), Type III solar radio bursts, *NASA Special Publication*, *50*, 357.

Swift, D. W., and J. R. Kan (1975), A theory of auroral hiss and implications on the origin of auroral electrons, *J, Geophys. Res*, *80*, 985.

Thejappa, G., R. J. MacDowall, and M. Bergamo (2012a), In situ detection of strong Langmuir turbulence processes in solar type III radio bursts, *J. Geophys. Res.*, *117*, A08,111.

Thejappa, G., R. J. MacDowall, and M. Bergamo (2012b), Phase coupling in Langmuir wave packets: Evidence of four wave interactions in solar type III radio bursts, *Geophys. Res. Lett.*, *39*, L05,103.

Tonks, L., and I. Langmuir (1929), Oscillations in ionized gases, *Phys. Rev.*, *33*, 195.

Tsurutani, B. T., G. S. Lakhina, C. M. Ho, J. K. Arballo, C. Galvan, A. Boonsiriseth, J. S. Pickett, D. A. Gurnett, W. K. Peterson, and R. M. Thorne (1998), Broadband plasma waves observed in the polar cap boundary layer: Polar, *J. Geophys. Res.*, *103*, 17,351.

Tsytovich, V. N. (1966), Statistical acceleration of particles in a turbulent plasma, *Sov. Phys. Usp.*, *9*, 370.

Tsytovich, V. N. (1970), *Nonlinear effects in a plasma*, Plenum, New York.

Vago, J. L., P. M. Kintner, S. W. Chesney, R. L. Arnoldy, K. A. Lynch, T. E. Moore, and C. J. Pollock (1992), Transverse ion acceleration by localized lower hybrid waves in the topside auroral ionosphere, *J. Geophys. Res.*, *97*, 16,935.

Vedenov, A. A., and L. I. Rudakov (1964), Wave interaction in continuous media, *Dokl. Akad. Nauk. SSSR*, *159*.

Vedenov, A. A., E. P. Velikhov, and R. Z. Sagdeev (1962), Quasi-linear theory of plasma oscillations, *Nucl. Fusion Suppl. Part 2*, p. 465.

Vladimirov, S. V., V. N. Tsytovich, S. I. Popel, and F. K. Khakimov (Eds.) (1995), *Modulational Interactions in Plasmas*, *Astrophysics and Space Science Library*, vol. 201.

Vlasov, A. A. (1968), The vibrational properties of an electron gas, *Sov. Phys. Usp.*, *10*, 721.

Weatherwax, A. T., J. LaBelle, M. L. Trimpi, R. A. Treumann, J. Minow, and C. Deehr (1995), Statistical and case studies of radio emissions observed near 2fce and 3fce in the auroral zone, *J. Geophys. Res.*, *100*, 7745.

Wild, J. P. (1950), Observations of the spectrum of high-intensity solar radiation at metre wavelengths. III. Isolated bursts, *Aust. J. Sci. Res.*, *A3*, 541.

Willes, A. J., and I. H. Cairns (2000), Generalized Langmuir waves in magnetized kinetic plasmas, *Phys. Plasmas*, *7*, 3167.

Willes, A. J., and I. H. Cairns (2001), Mode conversion and reflection of Langmuir waves in an inhomogeneous solar wind, *Publ. Astron. Soc. Aust.*, *18*, 355.

Willes, A. J., and I. H. Cairns (2003), Banded frequency structure from linear mode conversion in inhomogeneous plasmas, *Phys. Plasmas*, *10*, 4072.

Wu, C. S., and L. C. Lee (1979), A theory of the terrestrial kilometric radiation, *Astrophys. J.*, *230*, 621.

Wu, C. S., C. B. Wang, P. H. Yoon, H. N. Zheng, and S. Wang (2002), Generation of type III solar radio bursts in the low corona by direct amplification, *Astrophys. J.*, *575*, 1094.

Yin, L., M. Ashour-Abdalla, M. El-Alaoui, J. M. Bosqued, and J.-L. Bougeret (1998), Generation of electromagnetic fpe and 2fpe waves in the Earth's electron foreshock via linear mode conversion, *Geophys. Res. Lett.*, *25*, 2609.

Yoon, P. H. (1995), Plasma emission by a nonlinear beam instability, *Phys. Plasmas*, *2*, 537.

Yoon, P. H., and J. LaBelle (2005), Discrete Langmuir waves in density structure, *J. Geophys. Res.*, *110*, A11,308.

Yoon, P. H., A. T. Weatherwax, T. J. Rosenberg, J. LaBelle, and S. G. Shepherd (1998), Propagation of medium frequency (14 MHz) auroral radio waves to the ground via the Z-mode radio window, *J. Geophys. Res.*, *103*, 29,267.

Zakharov, V. E. (1972), Collapse of Langmuir waves, *Sov. Phys. JETP*, *35*, 908.